

**NUMERICAL INVESTIGATIONS OF  
FLASH-BOILING GASOLINE DIRECT INJECTION  
SPRAYS**

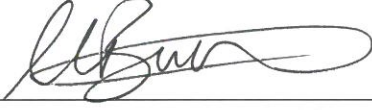
**A Thesis Submitted to  
the Graduate School of Engineering and Sciences of  
İzmir Institute of Technology  
in Partial Fulfillment of the Requirements for the Degree of  
MASTER OF SCIENCE  
in Mechanical Engineering**

**by  
Orhan ORAL**

**July 2019  
İZMİR**

We approve the thesis of **Orhan ORAL**

Examining Committee Members:



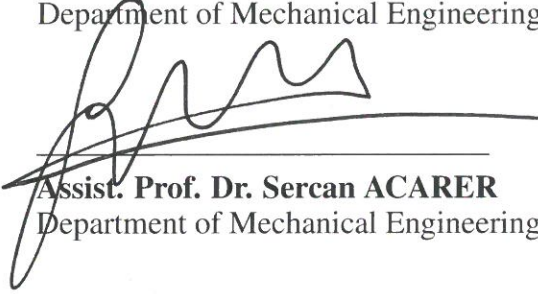
**Assoc. Prof. Dr. Murat BARIŞIK**

Department of Mechanical Engineering, İzmir Institute of Technology



**Assoc. Prof. Dr. Erdal ÇETKİN**

Department of Mechanical Engineering, İzmir Institute of Technology



**Assist. Prof. Dr. Sercan ACARER**

Department of Mechanical Engineering, İzmir Katip Çelebi University

19 July 2019



**Assoc. Prof. Dr. Murat BARIŞIK**

Supervisor

Department of Mechanical Engineering  
İzmir Institute of Technology

**Assist. Prof. Dr. Hasan ÇELİK**

Co-Supervisor

Department of Mechanical Engineering  
İzmir University of Economics



**Prof. Dr. Sedat AKKURT**

Head of the Department of  
Mechanical Engineering

**Prof. Dr. Aysun SOFUOĞLU**

Dean of the Graduate School of  
Engineering and Sciences

## **ACKNOWLEDGMENTS**

I would like to thank my supervisor Assoc. Prof. Dr. Murat Barışık for his support and guidance. I also would like to thank my co-supervisor Assist. Prof. Dr. Hasan Çelik for his endless support and contributions to my thesis. His guidance and expertise helped me a lot to finish this thesis. I would like to state my thankfulness to Assist. Prof. Dr. Alvaro Diez for everything he taught me and his contributions to my thesis.

I want to thank my friends Anılcan Ulu, Seven Burçin Çellek, Yağmur Güleç, Semih Berk Seven, Farid Musa, Tugay Tatlıdil, Doğan Can Aksöz and Emre Akkuzugil for their support and friendship.

Moreover, I wish to express my gratitude to my dear mother Nurten Oral and my dear father Mehmet Ragıp Oral whose emotional and endless support helped me to deal with this tough study.

# ABSTRACT

## NUMERICAL INVESTIGATIONS OF FLASH-BOILING GASOLINE DIRECT INJECTION SPRAYS

Gasoline Direct Injection (GDI) system is a new technology that is the combination of injection in diesel engines and ignition in gasoline engines. Comparing with the conventional methods of injection, it has many advantages including, fuel economy, higher engine power, lower engine knock tendency,  $NO_x$  and cold-start  $HC$  emission rates. The operation of the GDI engine is affected by the processes of fuel injection, spray atomization and vaporization, charge cooling, air/fuel mixture preparation, and in-cylinder charge motion. Therefore, numerical modeling has an important role to improve all these factors affecting the engine.

This thesis focuses on numerical analyses of the fuel sprays injected into a constant volume chamber by a single hole GDI injector under flash-boiling and non-flash-boiling conditions. The aim of this thesis is to develop a numerical model that can be used in flash-boiling spray simulations and to validate the results of the numerical model against experimental data in terms of spray angle and spray penetration. Initially the GDI sprays were simulated by the standard spray simulation model of OpenFOAM solver package that was tuned for gasoline injections. Then the model was modified for both non-flashing and flashing spray simulations and the results were compared with experimental ones. It is concluded that; discharge coefficient and spray initial angle have critical impacts on the numerical results.

## ÖZET

### KAYNAYAN BENZİNLİ DOĞRUDAN ENJEKSİYONLU SPREYLERİN SAYISAL OLARAK İNCELENMESİ

Benzinli doğrudan enjeksiyon (GDI) sistemi, dizel motorlardaki enjeksiyon ve benzinli motorlarda ki ateşlemenin birleşimidir. Konvansiyonel enjeksiyon yöntemleri ile karşılaştırıldığında, yakıt ekonomisi, daha yüksek motor gücü, daha düşük motor vuru-  
runtu eğilimi,  $NO_x$  ve soğuk başlatma  $HC$  emisyon oranları gibi birçok avantajı vardır. GDI motorunun çalışması yakıt enjeksiyonu, püskürtme atomizasyonu ve buharlaştırma, soğutma, hava/yakıt karışımı hazırlığı ve silindir içi hareketlerden etkilenir. Bu nedenle, sayısal modelleme, motoru etkileyen tüm bu faktörleri iyileştirmek için önemli bir role sahiptir.

Bu tez, kaynama ve normal koşullar altında tek delikli bir GDI enjektörü ile sabit bir hacim haznesine enjekte edilen yakıt sprelerinin sayısal analizini içermektedir. Bu tezin amacı, kaynayan spre simülasyonlarında kullanılabilecek sayısal bir model geliştirmek ve deneysel verilere karşı nümerik modelin sonuçlarını spre açısı ve spre penetrasyonu açısından doğrulamaktır. Başlangıçta GDI spreleri, OpenFOAM'ın benzin enjeksiyonları için ayarlanmış standart spre simülasyon modeli ile simüle edilmiştir. Daha sonra model, hem kaynayan hem de normal püskürtme simülasyonları için modifiye edilmiş ve sayısal analiz sonuçları, deneysel veri ile karşılaştırılmıştır. Sonuç olarak; deşarj katsayısı ve spre başlangıç açısı, sayısal sonuçlar üzerinde kritik etkilere sahiptir.

# TABLE OF CONTENTS

LIST OF FIGURES .....	viii
LIST OF TABLES .....	x
LIST OF SYMBOLS .....	xi
LIST OF ABBREVIATIONS .....	xiv
CHAPTER 1. INTRODUCTION .....	1
1.1. Introduction to SI Engines .....	1
1.2. Methods to Develop The Fuel Economy in SI Engines .....	2
1.2.1. Port Fuel Injection and GDI .....	4
1.3. Gasoline Direct Injection Technology .....	6
1.3.1. Working Principle of DISI Engines .....	7
1.4. GDI Sprays .....	9
1.4.1. Breakup Regimes of Liquid Jets.....	11
1.4.2. Breakup Regimes of Liquid Drops .....	13
1.5. Flash-boiling.....	14
1.6. Background and Motivation .....	16
1.7. Organization of Thesis .....	17
CHAPTER 2. LITERATURE SURVEY .....	18
2.1. Previous Studies of Diesel Sprays .....	18
2.2. Previous Studies of GDI Sprays .....	23
CHAPTER 3. METHODOLOGY .....	30
3.1. Spray Equation .....	30
3.2. Phase Modeling .....	31
3.2.1. Gaseous Phase.....	31
3.2.2. Liquid Phase.....	32
3.3. Spray Modeling .....	33

3.3.1. Rosin-Rammler Droplet Size Distribution Model .....	33
3.3.2. Reitz-Diwakar Breakup Model .....	34
3.3.3. Pilch-Erdman Breakup Model .....	35
3.3.4. TAB Breakup Model .....	36
3.3.5. Pilch-Erdman/TAB Hybrid Breakup Model .....	37
3.3.6. Trajectory Model .....	38
3.3.7. Evaporation and Heat Transfer Model .....	38
3.3.8. $k-\varepsilon$ Turbulence Model.....	40
3.3.9. Realizable $k-\varepsilon$ Turbulence Model .....	41
3.4. Spray Angle Calculation .....	42
3.5. Numerical Setup.....	44
3.6. Model Validation .....	50
CHAPTER 4. RESULTS AND DISCUSSIONS .....	54
CHAPTER 5. CONCLUSIONS .....	72
REFERENCES .....	74

# LIST OF FIGURES

<u>Figure</u>	<u>Page</u>
1.1 Actual four-stroke spark ignition .....	2
1.2 Single-point and multi-point injection systems .....	5
1.3 GDI operating modes .....	6
1.4 Combustion systems of GDI .....	6
1.5 GDI nozzle types .....	7
1.6 Gasoline direct injection .....	8
1.7 Detailed representation of a full-cone spray .....	9
1.8 Three-dimensional Ohnesorge diagram .....	12
1.9 Relation of jet breakup length and jet velocity $u$ .....	13
1.10 Drop breakup regimes .....	14
1.11 Conventional and flash-boiling injection .....	15
2.1 Definition of VSB2 spray model .....	18
2.2 Mie-scattering experimental setup .....	19
2.3 Cross section and the slice of the domain .....	21
2.4 Experimental and numerical spray structures .....	22
2.5 Numerical study of spray evolution .....	24
2.6 Experimental and numerical setup .....	26
2.7 Representation of flashing drops .....	27
2.8 The single-hole research injector .....	28
3.1 TAB model .....	37
3.2 Collusion in Trajectory Model .....	38
3.3 Spray angle for a single-hole GDI injector .....	43
3.4 Experimental and numerical spray angle measurement .....	44
3.5 Computational domain and mesh configuration .....	45
3.6 Experimental measurement of the injection profile after SOI .....	46
3.7 Modified injection profiles for different $T_{\text{fuel}}$ .....	47
3.8 Comparison of secondary breakup models at $T_{\text{fuel}}=293\text{K}$ , $P_v=1\text{bar}$ .....	51
3.9 Comparison of turbulence models at $T_{\text{fuel}}=293\text{K}$ , $P_v=1\text{bar}$ .....	52
3.10 Mesh dependency test at $T_{\text{fuel}}=293\text{K}$ , $P_v=1\text{bar}$ .....	53
3.11 Time convergence test at $T_{\text{fuel}}=293\text{K}$ , $P_v=1\text{bar}$ .....	53



4.1	Spray penetration and cone angle at $T_{\text{fuel}}=293\text{K}$ $P_v=3\text{bar}$ .....	55
4.2	Spray penetration and cone angle at $T_{\text{fuel}}=293\text{K}$ $P_v=1\text{bar}$ .....	56
4.3	Spray penetration and cone angle at $T_{\text{fuel}}=293\text{K}$ $P_v=0.4\text{bar}$ .....	57
4.4	Spray penetration and cone angle at $T_{\text{fuel}}=363\text{K}$ $P_v=1\text{bar}$ .....	58
4.5	Spray penetration and cone angle at $T_{\text{fuel}}=363\text{K}$ $P_v=3\text{bar}$ .....	59
4.6	Spray penetration and cone angle at $T_{\text{fuel}}=393\text{K}$ $P_v=3\text{bar}$ .....	60
4.7	Spray penetration and cone angle at $T_{\text{fuel}}=363\text{K}$ $P_v=0.4\text{bar}$ .....	61
4.8	Spray penetration and cone angle at $T_{\text{fuel}}=393\text{K}$ $P_v=1\text{bar}$ .....	62
4.9	Spray penetration and cone angle at $T_{\text{fuel}}=393\text{K}$ $P_v=0.4\text{bar}$ .....	63
4.10	Comparison of two numerical models at $T_{\text{fuel}}=393\text{K}$ , $P_v=3\text{bar}$ .....	64
4.11	Comparison of two numerical models at $T_{\text{fuel}}=363\text{K}$ , $P_v=0.4\text{bar}$ .....	65
4.12	Comparison of two numerical models at $T_{\text{fuel}}=393\text{K}$ , $P_v=1\text{bar}$ .....	66
4.13	Comparison of two numerical models at $T_{\text{fuel}}=393\text{K}$ , $P_v=0.4\text{bar}$ .....	66
4.14	Comparison of numerical data for constant $P_v$ and variable $T_f$ .....	68
4.15	Comparison of numerical data for constant $T_f$ and variable $P_v$ .....	69
4.16	Experimental particle distribution .....	70
4.17	Numerical particle distribution .....	70

# LIST OF TABLES

<b><u>Table</u></b>	<b><u>Page</u></b>
1.1 AtSPR ranges .....	16
3.1 Hybrid breakup model .....	37
3.2 Mesh configuration .....	45
3.3 Density of n-heptane .....	47
3.4 Simulation cases .....	48
3.5 Theoretically calculated discharge coefficient and spray initial angle values ...	49
3.6 AtSPR values under different conditions .....	49
3.7 Summary of sub-models .....	50
4.1 Average standard deviation of spray angle analyses .....	71

## LIST OF SYMBOLS

$\eta_{th,Otto}$	.....	Thermal efficiency of Otto cycle
$r_c$	.....	Compression Ratio
$k$	.....	Specific Heat Ratio
$c_p$	.....	Specific Heat at Constant Pressure
$c_v$	.....	Specific Heat at Constant Volume
$CO_2$	.....	Carbon di Oxide
$HC$	.....	Hydrocarbons
$NO_x$	.....	Nitrogen oxides
$S$	.....	Spray Penetration Length
$t$	.....	Time
$t_{break}$	.....	Breakup Time
$\rho_l$	.....	Liquid Density
$\rho_g$	.....	Gas Density
$D$	.....	Diameter of the Nozzle
$\Delta P$	.....	Pressure Difference
$P_{inj}$	.....	Injection Pressure
$P_{chamber}$	.....	Chamber Pressure
$d$	.....	Diameter
$\mu_l$	.....	Dynamic Viscosity of the Liquid
$\mu_g$	.....	Dynamic Viscosity of the Gas
$C$	.....	Empirical Constant
$r$	.....	Radius
$u$	.....	Velocity
$We$	.....	Weber Number
$Re$	.....	Reynolds Number
$Z$	.....	Ohnesorge Number
$\sigma$	.....	Surface Tension
$d$	.....	The Droplet Diameter Before Breakup
$u_{rel}$	.....	Relative Velocity Between Droplet and Gas
$\varepsilon$	.....	Void Fraction
$V_{bub}$	.....	Bubble Volume
$V_{liq}$	.....	Liquid Volume

$P_a$	Ambient Pressure at a Given Temperature
$P_s$	Saturation Pressure of the Liquid at a Given Temperature
$T$	Temperature
$\mathbf{g}$	Gravity
$\sigma_{ij}$	Reynold Stress Tensor
$\tau_{ij}$	Viscous Stress Tensor
$\tau_p$	Relaxation Time of Droplet
$K$	Mass or Volume Fraction
$\delta$	Location Parameter
$n$	Spread Parameter
$Oh$	Ohnesorge Number
$T_b$	Total Breakup Time
$\tau_b$	Characteristic Breakup Time
$x, y, z$	Positions
$Q$	Heat Flux
$\alpha$	Heat Transfer Coefficient
$H_v$	Latent Heat
$\Delta T$	Superheat Degree
$M_{sc}$	Sub-cooled Evaporation Rate
$M_{sh}$	Superheated Evaporation Rate
$M_t$	Total Evaporation Rate
$Sh$	Sherwood Number
$Sc$	Schmidt Number
$Nu$	Nusselt Number
$Pr$	Prandtl Number
$D$	Diffusivity Coefficient
$Y_f$	Fuel Vapor Mass Fraction
$H_v$	Latent Heat of the Fluid
$k$	Turbulence Kinetic Energy
$\varepsilon$	Turbulence Dissipation Rate
$m$	Mass
$V$	Volume
$n_{particles}$	Number of Particles
$\dot{m}$	Mass Flow Rate

*A* ..... Area

## LIST OF ABBREVIATIONS

DISI .....	Direct Injection Spark Ignition
GDI .....	Gasoline Direct Injection
CI .....	Compression Ignition
DI .....	Direct Injection
VVT .....	Variable Valve Timing
AtSPR .....	Ambient to Saturation Pressure Ratio
SMD .....	Sauter Mean Diameter
RANS .....	Reynolds Averaged Navier Stokes Equations
LISA .....	Linearized Instability Sheet Atomization
CFD .....	Computational Fluid Dynamics
TAB .....	Taylor Analogy Breakup
KHRT .....	Kelvin-Helmholtz, Rayleigh-Taylor
PDA .....	Phase Doppler Anemometry
ETAB .....	Enhanced Taylor Analogy Breakup
PDF .....	Probability Density Function
SOI .....	Start of Injection
SIA .....	Spray Initial Angle

# CHAPTER 1

## INTRODUCTION

In recent years, the design and development of new generation engines is a trending topic in the automotive industry due to the strict legislation of emission rates and efficiency regulations. To gain a better combustion process and limit the pollutants, researchers have concentrated on Direct Injection Spark Ignition Engines (DISI). This technology has several advantages, such as fuel economy, lower emission rates, higher engine power, less knocking tendency at full load operations, and better thermodynamic efficiency in part load and cold start operating conditions. Particularly the injector has a significant role in spray-guided combustion systems for the accomplishment of correct air/fuel mixture formation. Thus, it is compulsory to have detailed information about spray evolution and interactions with the ambient in several engine operating conditions for the improvement of Gasoline Direct Injection (GDI) technology<sup>[1]</sup>. Instead of repeating costly experiments, numerical models have been developed for the validation of experimental works besides the experimental studies of spray structure and evolution.

### 1.1. Introduction to SI Engines

Internal combustion engines produce mechanical power from the thermal energy released by burning or oxidizing the fuel inside the engine. Based on the type of ignition, there are two engines called as spark-ignition engine (SI) and compression ignition engine (CI). The two main differences between these engines are different fuel types that are used to gain mechanical power and dissimilar thermodynamic cycles, which show the working principle of these engines. While Otto cycle represents how a spark-ignition engine runs, Diesel cycle indicates the way of working for compression ignition engine.

Otto cycle has four processes. In these processes of ideal Otto cycle, the working fluid is the air because it is easy to complete thermodynamic calculations for that fluid. Firstly the air is compressed in isentropic conditions. Then heat is added at constant volume, and isentropic expansion starts. After the expansion process, heat is lastly rejected at constant volume. The actual cycle shown in Figure (1.1) contains air-fuel mixture instead

of only air and spark plug ignites the air-fuel mixture after the mixture is compressed in the compression stroke. Then the products of chemical reaction at high pressure push down the piston for creating useful work output in power stroke. In the next process, the piston moves upwards to eject the combustion products through the exhaust valve in expansion stroke and finally moves downwards to fill the chamber with fresh air-fuel mixture through the intake valve in the intake stroke<sup>[2]</sup>.

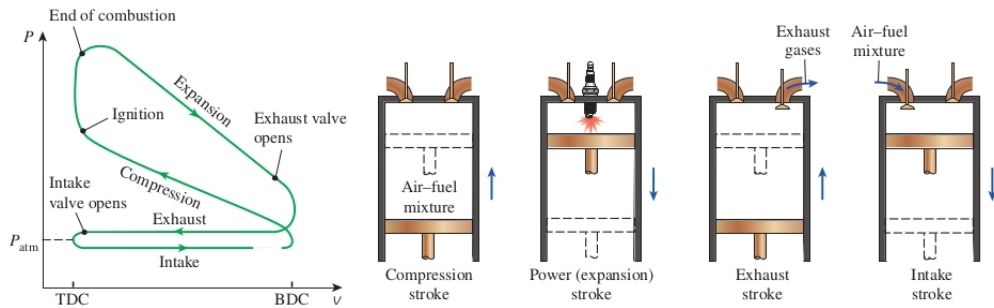


Figure 1.1.: Actual four-stroke spark ignition engine (Source: Cengel et al.<sup>[2]</sup>)

Otto cycle is executed in a closed system where the changes in kinetic and potential energies are neglected; therefore, the thermal efficiency of the Otto cycle can be formulated as in Equation (1.1),

$$\eta_{th,Otto} = 1 - \frac{1}{r_c^{k-1}} \quad (1.1)$$

where  $r_c$  is the compression ratio that is the division of maximum cylinder volume to minimum cylinder volume and  $k$  is the specific heat ratio  $c_p/c_v$ . Equation (1.1) demonstrates that the thermal efficiency of the engine is directly proportional to the compression ratio and specific heat ratio. On the contrary, the compression ratio is limited by engine knock, which is the autoignition of air, fuel, and residual gas mixture before the advancing flame. Engine knock is easily affected by the temperature of air-fuel mixture during the compression stroke. Therefore, injection systems have been turned into direct injection for controlling the air-fuel mixture generation. Direct injection system allows the fuel to vaporize efficiently. It absorbs heat from the ambient air during the evaporation, which causes a drop in air temperature. High pressure rates can be reached without a risk of engine knock owing to that charge cooling effect<sup>[3]</sup>.



## 1.2. Methods to Develop The Fuel Economy in SI Engines

Gasoline Engines have been used in the automobiles since the second half of the 1800s; however, the usage of gasoline engines regressed after the invention of diesel engines, as diesel engines have higher efficiency and their fuel consumption rate is less than gasoline engines. Although diesel engines have these excellent features, the emission rates of diesel engines are considerably more than gasoline engines, and they are now thought to be removed from the market due to the legislations that are related to the effects of emissions. Therefore, gasoline engines once again come up with different technologies which are utilized to reduce the emission and the fuel consumption rates.

While improving modern gasoline engines, vehicle manufacturers commonly use downsizing and downspeeding, which are decreasing the total displacement volume and lowering the engine speed by adjusting the transmission. A significant fuel economy can be provided by these methods since the engine starts operating at more efficient high load conditions instead of less efficient partial load conditions. The fuel consumption and  $CO_2$  emission rates can also be reduced by combining different technologies, including direct injection (DI) of fuel, that is known as GDI, boosting, variable valve timing (VVT), lessening engine friction, and cylinder deactivation<sup>[4]</sup>.

GDI technology can be thought of the combination of ignition in gasoline engines and injection in diesel engines. It helps the engine to develop the accuracy of air-fuel ratio, decrease throttling losses, have higher thermal efficiency and higher compression ratio, rise performance and volumetric efficiency in consequence of charge cooling effect, reduce  $CO_2$  emissions and the fuel consumption, lessen the heat losses, and have better cold-start performance and drive comfort<sup>[5]</sup>.

Boosting is enhancing the specific power of the engine by increasing the inducted air. Turbocharging and supercharging systems are used to boost an engine. A turbocharger is a turbine, that is driven by the exhaust gases, for compressing and forcing more air to the engine. Besides a supercharger is a system, that is almost exactly the same as a turbocharger; however, it is driven by the engine's crankshaft<sup>[6]</sup>.

VVT is merely changing the timing of valve lift event. This process is utilized in internal combustion engines to advance performance and fuel economy. It reduces the tendency of knocking and trapped residuals. If it is compared with the fixed valve engines, the  $CO_2$  emissions in an engine with VVT system are 2-4% less than fixed valve ones.

Friction reduction is essential to enhance the fuel economy of an engine and a

small development in any components, such as piston surfaces, piston rings and crankshaft can end up with a positive effect on fuel economy.

Consequently, the cylinder deactivation, which is also known as variable engine displacement, is used to have an improved fuel economy. Half of the cylinders in the engine stops working while others are operating at roughly twice the load. Both intake and exhaust valves of non-operating cylinders are closed. Therefore, there is not an injection into these cylinders. It means that pumping losses are lower than normal conditions and this brings about reduced fuel consumption<sup>[4]</sup>.

### **1.2.1. Port Fuel Injection and GDI**

Port fuel injection and gasoline direct injection are the fuel injection types after the carburetor. There are two dissimilar port fuel injection systems, namely single point injection and multi-point injection.

In single-point injection system, intake manifold delivers the mixture of air, fuel droplets, and fuel vapor to the cylinders. Some of this mixture causes the formation of liquid wall film, as it is stored on the walls. The liquid wall film moves much slower than the remaining mixture stream to each cylinder. In addition to this, the wall film thickness alters with a change in the load. Manifold has to spread the centrally prepared mixture into the cylinders; however, it is tough to distribute the mixture uniformly owing to the manifold's complicated geometry.

The number of injectors in multi-point injection system is equal to the number of cylinders. These injectors are located near the intake valve, as shown in Figure (1.2). The desired amount of fuel is injected into the part of the manifold that belongs to the separate cylinders. The multi-point injection system prevents the problems that occur due to the non-uniform fuel distribution. Since the wettable area is small and the temperature is high near the intake valve, the percentage of fuel deposited in the liquid wall film is less than the amount of stored fuel in the other injection system. This results in a correct fuel quantity during the injection, and some advantages related to fuel consumption and emissions. In order to improve the vaporization and mixture generation outside of the cylinders and block the large droplets before they get into the combustion chamber, the injection is done when the intake valve is not open. Furthermore, preventing these large droplets from entering the cylinders helps the engine to avoid *HC* emissions because they

can be deposited on the cylinder walls if they achieve to go into the cylinders.

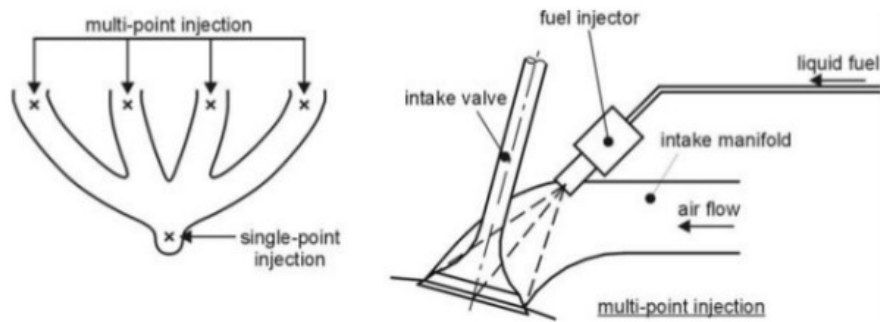


Figure 1.2.: Single-point and multi-point injection systems (Source: Baumgarten<sup>[3]</sup>)

The direct injection system has important advantages like reducing  $CO_2$  emissions and enhancing fuel economy. Common-rail injection system is utilized to raise the injection pressures considerably because highly dispersed sprays in a short time are needed for spray distribution and mixture formation in the cylinders. In diesel engines, the direct injection occurs near top dead center. However, in GDI engines, the direct injection can be done during intake stroke for the full load (homogeneous stoichiometric mode) or during the compression stroke for the part load (stratified mode).<sup>[3]</sup> The strategy of late injection enables burning the lean mixture by holding rich combustible mixture close to spark plug during the discharge time. In addition to that, the stratified mode has a better fuel economy and it is able to burn lean mixture. On the other hand, early injection method enables to form homogeneous mixture due to the sufficient time for mixture preparation. The advantage of early injection strategy is the charge cooling which takes the heat energy from the ambient for vaporization of the fuel and it advances the volumetric efficiency. Charge cooling decreases the knocking tendency; therefore, it helps GDI engine to run with a high compression ratio.

The combustion system of GDI is divided into three different categories, which are air-guided, wall-guided, and spray-guided system. The location of the injector in the wall-guided and air-guided system is away from the spark plug. The location is determined by well-defined motion in the cylinder or by the interaction between spray and the piston cavity. On the contrary, the distance between the injector and the spark plug is close in spray-guided systems and this provides better combustion. Wall-guided and air-guided systems are the first generation of GDI and spray-guided system is the second

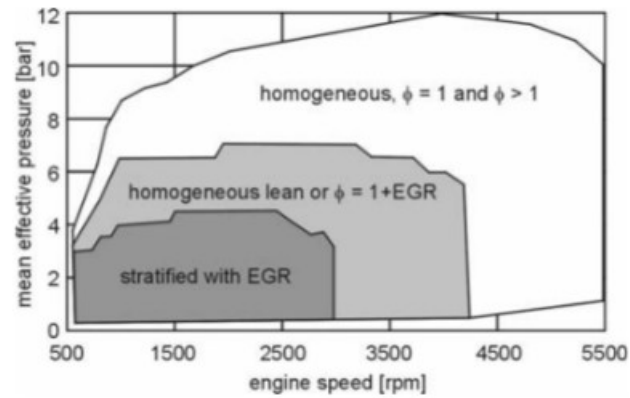


Figure 1.3.: GDI operating modes (Source: Baumgarten<sup>[3]</sup>)

generation of GDI. When these two generations are compared, the spray-guided system has greater combustion efficiency and combustion phases losses that brings about important development of the fuel economy<sup>[7]</sup>.

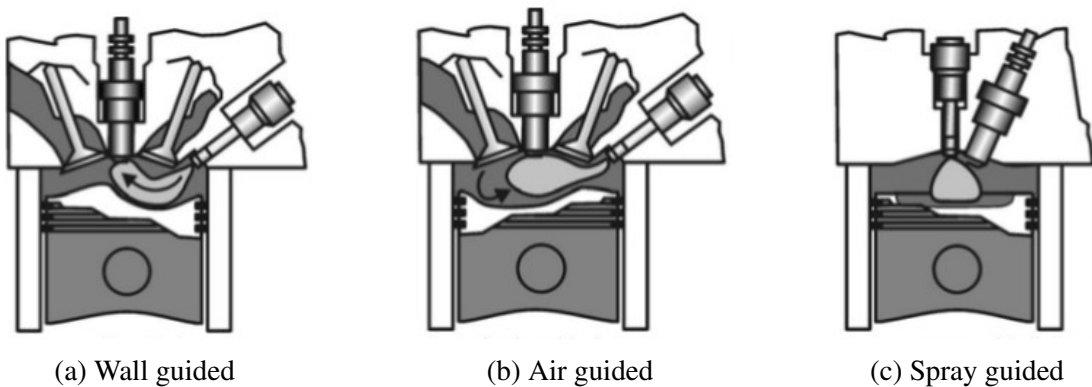


Figure 1.4.: Combustion systems of GDI (Source: Baumgarten<sup>[3]</sup>)

### 1.3. Gasoline Direct Injection Technology

Combustion process of a GDI engine is directly related to the fuel injection and fuel-air mixture formation; therefore, improvement of a proper injector is a significant task. There are three types of injectors used in GDI engines. These are multihole nozzle,

outward-opening nozzle, and swirl nozzle injector.

Older versions of stratified charge wall-guided engines and homogeneous GDI engines, where the injection pressure is slightly low (50-100 bar), have swirl nozzle injectors. The fuel obtains an angular velocity due to the inner structure of these injectors before it is injected into the cylinders. The spray has a hollow cone shape after its generation and it exhibits good atomization characteristics. They are not sensitive to thermal and mechanical disturbances as well as the contamination; however, they are not suitable to be used in spray-guided systems, as the spray cone angles can be affected by back pressure in the combustion chamber.

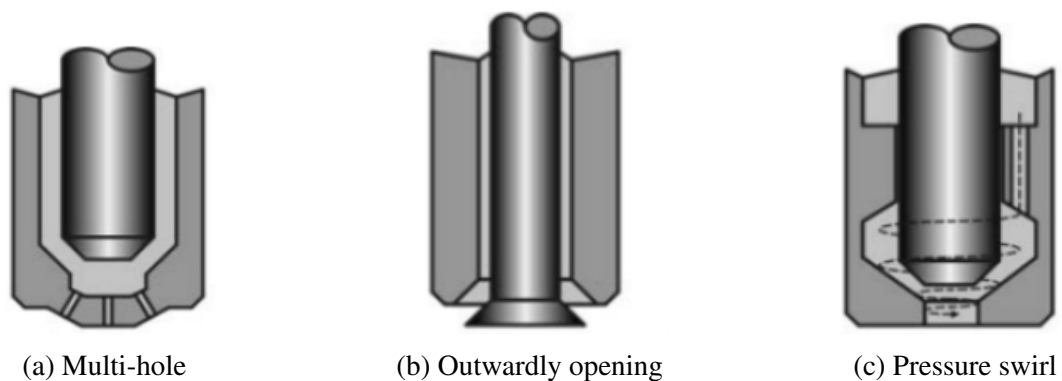


Figure 1.5.: GDI nozzle types (Source: Baumgarten<sup>[3]</sup>)

The multi-hole injectors produce flexible spray patterns by changing the orientation of the nozzle holes, but they need high pressures (more than 150 bar) to accomplish good atomization. When these high pressure injection values are associated to the small nozzle diameters, the tendency of nozzle hole blockage by soot deposits rises, so this type of injectors need good cooling to prevent soot formation near the injector. The other disadvantage of this sort of injectors is wall-wetting due to the retarded fuel injection that causes *HC* and soot emissions<sup>[4]</sup>.

The outward-opening injectors have also a hollow cone spray that does not collapse at higher back pressures and does not have any pre-spray. It is a significant positive effect on the formation of the mixture in GDI engines, yet there may be critical deposit formation because of the elevated temperatures at the seat and at the needle tip<sup>[3]</sup>.

### 1.3.1. Working Principle of DISI Engines

A direct injection spark ignition engine has two combustion modes that are homogeneous stoichiometric mode and stratified mode. The fuel is injected during the intake stroke to form a homogeneous mixture at high loads, but at low loads the fuel is generally injected into the cylinder during the compression stroke when the piston is almost at the top dead center.

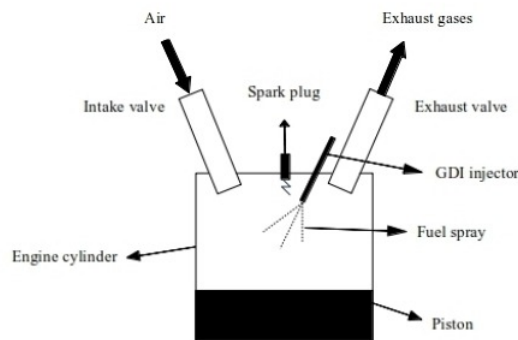


Figure 1.6.: Gasoline direct injection

Smaller droplets start breaking away from the liquid core after the fuel injection and then they evaporate. The fuel vapor is mixed with air and the mixture is moved towards the spark plug. The fuel's liquid to gas phase transformation time is very limited. It takes normally few hundred microseconds for a late injection. Therefore, formation of a highly stratified fuel-air mixture occurs in the middle of the chamber. The spark plug starts ignition of newly prepared mixture after the injection or during the injection. Ignition process may happen in a few crank angles and it is followed by the propagation of turbulent flame. Due to the highly stratified mixture, the flame propagation is the quickest in the relatively rich fuel-air mixture in collaboration with a large amount of  $CO_2$  formation. In lean and rich mixtures, the propagation is slower and this results in substantial amount of unburned  $HC$ . Moreover,  $NO_x$  can be originated in the comparatively lean products because of the high combustion temperature (2200 K or more). The lean and rich products burn in mixing controlled mode after the premixed flame propagated. The com-

bustion process happens at the end of the compression and most of the expansion stroke. Thereafter, exhaust process takes place and burned gases are ejected from the chamber<sup>[4]</sup>.

## 1.4. GDI Sprays

Although hollow cone sprays are mostly used in DISI engines, the full cone sprays, that are composed by single hole injectors, are going to be investigated in this work. A full-cone spray is described schematically in Figure (1.7).

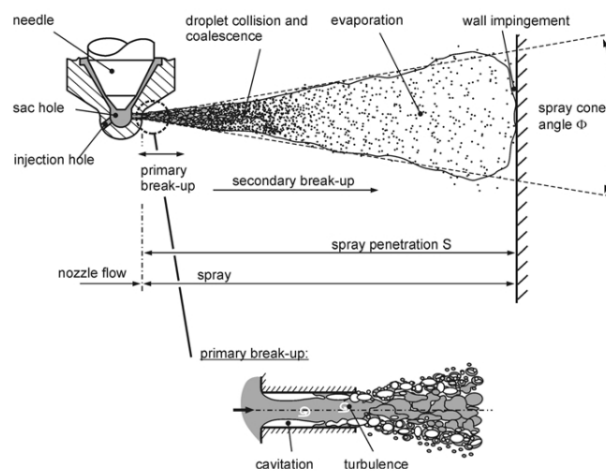


Figure 1.7.: Detailed representation of a full-cone spray (Source: Baumgarten<sup>[31]</sup>)

The needle, sac hole and injection hole located at the bottom side of the injector are indicated in Figure (1.7). The fuel jet begins breaking-up into a conical spray immediately, after it leaves the nozzle hole. The first breakup is known as the primary breakup and in this stage, a dense spray in the vicinity of the nozzle is originated by large ligaments and droplets. The high injection pressures cause the formation of cavitation and turbulence that are the main breakup mechanisms and they are usually generated inside the injection holes. The following breakup regime, that consists of smaller droplets originated from the already existing ones, is known as secondary breakup and it is caused by the aerodynamic forces due to the relative velocity between liquid droplets and ambient gas.

As the droplets are decelerated by the aerodynamic forces, the drops at the spray tip face with the most powerful drag force and their velocity becomes much slower than

the ones tracing them. Thus, new droplets are perpetually replaced with the drops at the spray tip and they are pushed by the new ones with low kinetic energy to the outer part of the spray. The outer region of the spray consists of less liquid mass and more fuel vapor, while the liquid mass seizes the regions near the spray axis.

There are few parameters, such as spray penetration, spray cone angle, average droplet diameter, and breakup length, which can be used to describe the behavior of a spray. Spray penetration and spray cone angle formulations are developed by Hiroyasu and Arai<sup>[8]</sup>. They claimed that spray penetration length can be analyzed by dividing it into two phases. The beginning point of the first phase is the start of injection ( $t=0$ , needle starts opening) and it is over when the liquid jet starts to breakup ( $t = t_{break}$ ). Equation (1.2) represents the first phase of the spray penetration length and linear growth of it can be observed from that equation. In the second phase ( $t > t_{break}$ ), there are droplets at the spray tip and the tip velocity is slower than the one in the first phase. Equation (1.3) is used for the spray penetration length during the second phase. In order to compose these phases, the breakup time is calculated via Equation (1.4).

$$t < t_{break} : S = 0.39 \times \left( \frac{2\Delta P}{\rho_l} \right)^{0.5} t \quad (1.2)$$

$$t > t_{break} : S = 2.95 \times \left( \frac{2\Delta P}{\rho_g} \right)^{0.25} (Dt)^{0.5} \quad (1.3)$$

$$t_{break} = \frac{28.65 \rho_l D}{(\rho_g \Delta P)^{0.5}} \quad (1.4)$$

where  $D$  is the diameter of the nozzle and  $\Delta P = P_{inj} - P_{chamber}$  is the pressure difference.

Sauter Mean Diameter (SMD) is a significant parameter that characterizes the success of the spray breakup. It is known as the surface-volume mean diameter that is equal to the proportion of the volume of all drops in the spray to the surface areas of all droplets.

$$SMD = \frac{\sum_{n=1}^n d_i^3}{\sum_{n=1}^n d_i^2} \quad (1.5)$$

In order to have much efficient evaporation and mixture formation, SMD value needs to be very small. When the SMD value is low, surface per unit volume is high



and that rises the efficiency of the evaporation and mixture formation. Even if SMD is used as an important quantity for spray formation processes, it does not help to figure out anything related to the droplet size distribution.

Depending on their experimental work, Hiroyasu and Arai<sup>[8]</sup> associated SMD to Reynolds and Weber numbers and prepared the Equation (1.6).

$$\frac{SMD}{D} = 0.38Re^{0.25}We^{-0.32}\left(\frac{\mu_l}{\mu_g}\right)^{0.37}\left(\frac{\rho_l}{\rho_g}\right)^{-0.47} \quad (1.6)$$

Here, increased nozzle diameter and rising gas density due to the bigger amount collisions make the SMD value higher. Additionally a higher injection pressure value leads to better atomization; therefore, it reduces the SMD.

Another important quantity, which needs to be covered, is the liquid core length. However, it is difficult to measure it due to high density ligaments and drops in the liquid core. Chehroudi et al.<sup>[9]</sup> derived Equation (1.7) based the electrical resistance measurements in the core region.

$$L_c = CD\sqrt{\frac{\rho_l}{\rho_g}} \quad (1.7)$$

Equation (1.7) demonstrates how the ratio of liquid and gas density, nozzle diameter, and empirical constant C, which changes between 3.3 and 11, influences the liquid core length. This expression was updated by Hiroyasu and Arai<sup>[8]</sup> and Equation (1.8) was composed.

$$L_b = 7D\left(1 + 0.4\frac{r}{D}\right)\left(\frac{p_g}{\rho_l u^2}\right)^{0.05}\left(\frac{L}{D}\right)^{0.13}\left(\frac{\rho_l}{\rho_g}\right)^{0.5} \quad (1.8)$$

#### 1.4.1. Breakup Regimes of Liquid Jets

The breakup of liquid jets is triggered by dissimilar breakup mechanisms that are dependent on the relative velocity of the liquid and the properties of ambient air and liquid. Those different breakup mechanisms are symbolized by the margin between the nozzle hole and the place of the first droplet generation, the breakup length, and the size of the produced droplets.

The measurements of intact liquid jet length were completed by Ohnesorge<sup>[10]</sup> for describing the jet breakup process quantitatively. According to Ohnesorge, the liquid Weber and Reynold numbers can be used to define disintegration process.

$$We = \frac{u^2 D \rho_l}{\sigma} \quad (1.9)$$

$$Re = \frac{u D \rho_l}{\mu_l} \quad (1.10)$$

The dimensionless Ohnesorge number ( $Z$ ) was finally derived after eliminating the jet velocity  $u$ .

$$Z = \frac{\sqrt{We}}{Re} = \frac{\mu_l}{\sqrt{\sigma \rho_l D}} \quad (1.11)$$

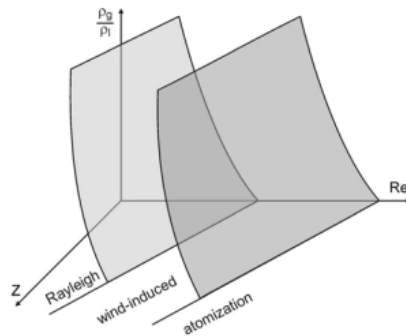


Figure 1.8.: Three-dimensional Ohnesorge diagram (Source: Baumgarten<sup>[3]</sup>)

The formula of Ohnesorge number contains all relevant fluid properties. However, considering only the liquid properties is not an adequate way to describe liquid jet breakup regimes, since increasing gas density can enhance the atomization. Thus, a three-dimensional Ohnesorge diagram including the gas-to-liquid density ratio was proposed<sup>[3]</sup>.

Even if the liquid velocity  $u$  was eliminated in Equation (1.11), it is the only variable when the nozzle diameter is fixed and the liquid properties are stable. Figure (1.9) illustrates the jet breakup curve that identifies the length of unbroken jet with respect

to the jet velocity  $u$ . Considering Figure (1.9), the curves between each letter represent a liquid breakup regime described in Figure (1.8). The atomization regime is the suitable one for engine sprays, as the resultant droplets are tinier than the nozzle diameter. On the other hand, the theory behind the jet breakup in atomization regime is too complicated due to the disintegration process, which is dependent on unknown and chaotic flow conditions in the nozzle hole. The validation of models is also very complex because of the high injection velocities, small dimensions, and intense spray<sup>[3]</sup>.

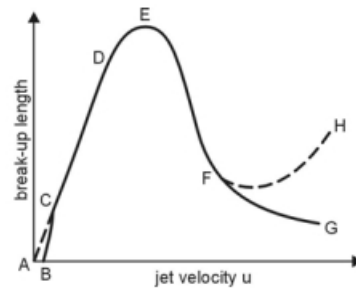


Figure 1.9.: Relation of jet breakup length and jet velocity  $u$  (Source: Baumgarten<sup>[3]</sup>)

## 1.4.2. Breakup Regimes of Liquid Drops

The aerodynamic forces initiated by the relative velocity  $u_{rel}$  between liquid droplet and the ambient lead to the breakup of drops in a spray. Those forces bring about either an unstable growing of waves on the liquid-gas interface or of the all droplets itself that eventually causes disintegration and the origination of smaller drops. Nevertheless the droplets are tried to keep spherical by surface tension force, which counteracts the deformation force. The surface tension force is dependent on the curvature of the droplet's surface. When the diameter of the droplet is smaller, the surface tension force and the critical relative velocity get bigger. This results in and unstable droplet deformation and disintegration. The gas phase Weber number in Equation (1.12) is used to express this behavior.

$$We_g = \frac{\rho_g u_{rel}^2 d}{\sigma} \quad (1.12)$$

In Equation (1.12),  $d$  represents the droplet diameter before breakup,  $\sigma$  is the surface tension between gas and liquid,  $u_{rel}$  is the relative velocity between droplet and gas, and  $\rho_g$  presents the gas density. The ratio of aerodynamic forces and surface and surface tension forces are stood for Weber number<sup>[3]</sup>.

The experimental investigations indicate the existence of different droplet breakup modes that depend on the Weber number. A detailed explanation of those modes were composed by Wierzba<sup>[11]</sup> and they are shown in Figure (1.10).

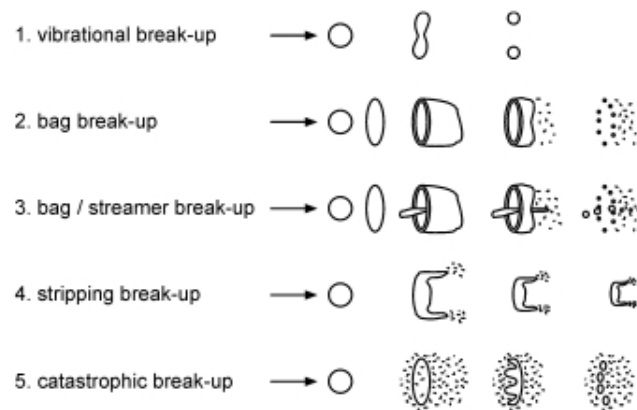


Figure 1.10.: Drop breakup regimes (Source: Wierzba<sup>[11]</sup>)

## 1.5. Flash-boiling

Flash-boiling is a metastable state that happens often in nozzles running at either large pressure drops or high temperatures. Saturation of a subcooled liquid may occur when the pressure drop is adequately high to decrease the substance pressure below the saturation pressure corresponding to its temperature. That leads to the generation of great numbers of bubbles, which can expand quickly in both number and size<sup>[12]</sup>.

For the internal combustion engines, this process takes place when highly pressurized liquid fuel is injected into the engine cylinders where the pressure is much smaller than the saturation pressure of the fuel at its first temperature. Since smaller droplets are acquired due to flash-boiling, it affects the atomization and breakup of the spray positively by inducing the fuel vaporization<sup>[13]</sup>. Therefore, flash-boiling can be desired to

have much efficient combustion in the internal combustion engines.

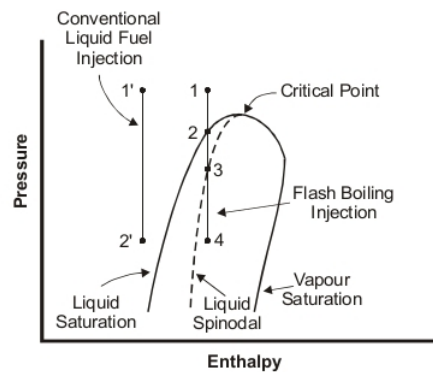


Figure 1.11.: Conventional and flash-boiling injection (Source: Schmitz et al.<sup>[14]</sup>)

Based on the previous experimental and numerical works, it is generally accepted that flash-boiling includes three parts, namely, bubble nucleation, bubble growth, and boiling explosion. The most important trigger of the bubble nucleation is the superheated degree of the droplet. As the liquid fuel is in a metastable state, vapor nucleation is activated when the fuel temperature is much bigger than the saturation temperature at given ambient temperature. There are two different bubble nucleation mechanisms that are known as homogeneous and heterogeneous nucleation. In heterogeneous nucleation, vapor bubble originates at specific zones, such as at fine solid particles, at crevices on the solid surfaces, mixed gas or dissolved gas inside the liquid fuel. On the contrary, homogeneous nucleation is the primary mechanism in the absence of solid surfaces and impurities<sup>[13-15]</sup>.

If the bubble diameter goes beyond a critical value after the nucleation process, bubble growth starts. Dissimilar mechanisms including the liquid inertia, the surface tension of the liquid, the pressure difference between the two phases, and the temperature gradient at the liquid/gas interface specify the growth rate of the bubble. In addition to that, the growth was divided into the stages based on those mechanisms mentioned above. Boiling of small droplets of emulsions was investigated by Roesle and Kulacki<sup>[16]</sup> and the bubble growth was split into two parts.

In the first part of the growth process, it was assumed that the radius of bubble has a constant value that is almost at critical radius. In the second stage, physical characteristics

of the liquid surrounding the bubble influenced the bubble growth rate. Moreover it was separated into three parts for a single component fuel. Those stages are the surface tension controlled stage, the pressure difference controlled stage, and the heat transfer controlled stage<sup>[17-18-19]</sup>.

Under flash-boiling conditions, bubble boiling explosion is a significant mechanism for fuel atomization. Unlike major features of flash-boiling, namely, spray cone angle and spray penetration, investigations of boiling explosion is still missing, particularly for the boiling explosion time. Suma et al.<sup>[20]</sup> searched the effect of void fraction ( $\varepsilon = V_{bub}/V_{bub} + V_{liq}$ ) on flash-boiling explosion and found that liquid jet breakup begins when it is between 0.51-0.53. Thereafter the occurrence of droplet breakup at the void fraction of 0.55 was assumed by Kawano et al.<sup>[21]</sup>. Suma's study pioneered to the flash-boiling explosion sub-model of Senda<sup>[15]</sup>, which assumes that the amount of broken droplets is two times more than the number of bubbles.

Postrioti<sup>[1]</sup> explored the effects of Ambient to Saturation Pressure Ratio (AtSPR), which is a dimensionless number that represents the superheated degree to define flash-boiling spray evolution, for a single hole GDI injector. It evaluates the spray tendency to flash-boiling by describing three regions shown in Table (1.1). When dimensionless number ( $P_a/P_s$ ) = 1, flash-boiling explosion happens for both single hole and multi-hole injectors<sup>[1-22]</sup>.

Table 1.1.: AtSPR ranges<sup>[1]</sup>

$1 > \text{AtSPR}$	Non Flash-Boiling
$1 > \text{AtSPR} > 0.3$	Transition Region
$0.3 > \text{AtSPR}$	Full Flash-Boiling

The flash-boiling process of the fuel sprays is very complicated from bubble nucleation to boiling explosion. As the temperature variation of the liquid droplet is considerably high during whole process, it directly influences the nucleation rate and the bubble growth rate. Flash-boiling explosion process in internal combustion engines is also very different from other flash-boiling applications. Consequently, flash-boiling phenomena is still unclear and new flash-boiling investigations and validations are required for better estimations of fuel atomization and vaporization.

## 1.6. Background and Motivation

Achieving the correct air/fuel mixture under different engine operating conditions is not an easy task; therefore, high injection pressures are utilized for promoting atomization and vaporization of the liquid fuel, since the better atomization and vaporization, the better air/fuel mixture. However, over penetration and piston wall wetting, which end up with a high level of *HC* and soot emissions, can occur because of high injection pressures. Here, flash-boiling phenomena steps in because under flashing conditions, fuel sprays penetrate shorter distance and have a wider angle. Hence, flash-boiling phenomena have been investigated both experimentally and numerically for a few decades. The main parameters that are needed for the analysis of flashing sprays are spray penetration length and spray cone angle. However, momentum flux and Sauter Mean Diameter (SMD) values were also taken into account in the previous studies.

In this study, the main goal is to develop a numerical model for the investigations of non-flashing and flashing fuel sprays injected by a single hole GDI injector IHP-293, which is a product of Magneti Marelli<sup>[23]</sup>. This thesis examines how the spray penetration length and the spray cone angle are influenced by fuel temperature, vessel pressure, discharge coefficient, spray initial angle and mesh dependency. In addition to that, the effects of fuel temperature and vessel pressure on discharge coefficient and injected mass profile will be analyzed. Moreover, all impacts will be scrutinized in the comparison of the numerical and experimental results for a better understanding of spray structures under non-flash-boiling and flash-boiling conditions.

## 1.7. Organization of Thesis

After general information about DISI engines is mentioned in this chapter, the previous numerical and experimental studies related to the fuel sprays are comprehensively investigated in Chapter 2. Then, the theoretical information behind the spray simulations is explained, numerical models are described, and numerical setup is depicted in Chapter 3. Furthermore, the model is validated in terms of spray penetration. The comparison of numerical and experimental results are clearly shown and discussed in Chapter 4. Finally, the general inferences and recommendations for future studies are indicated in Chapter 5.

## CHAPTER 2

### LITERATURE SURVEY

Direct injection technology was firstly used for the applications of CI engines. Therefore, the studies for the investigations of diesel sprays played a significant role to develop GDI technology. In this chapter, detailed information related to the numerical and experimental examinations of both diesel and gasoline sprays is mentioned.

#### 2.1. Previous Studies of Diesel Sprays

Direct injection of liquid fuel under dissimilar circumstances has different spray structures that affect the performance and pollution rates severely. Considering the strict laws related to the exhaust gases produced by diesel engines, there has been many experimental and numerical studies completed for diesel injection.

A new spray model namely VSB2 was composed by Kösters and Karlsson<sup>[24]</sup> and it was tested under different conditions. In that model, a stochastic blob including differently sized droplets was used instead of a conventional Lagrangian parcel. RANS equations were used for the simulations of the turbulence due to the acceptable time costs and mostly applicable results of this method.

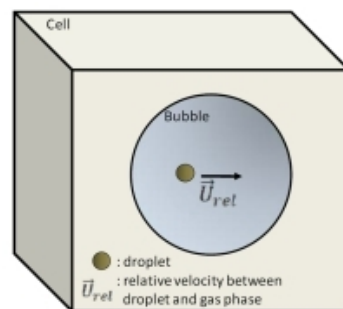


Figure 2.1.: Definition of VSB2 spray model (Source: Kösters et al.<sup>[24]</sup>)

A cylindrical geometry with 60 mm diameter and 110 mm length was used for



the numerical simulations. 232,320 cells with the measure of 0.5 mm x0.5 mm x1 mm were placed in the middle of the geometry where injector tip is. Additionally, a coarser mesh configuration with 44,880 cells was also implemented for the sensitivity studies. The results of two turbulence models known as  $k-\varepsilon$  and RNG  $k-\varepsilon$  were compared with the experimental values, which were obtained by Siebers and Naber<sup>[25-26]</sup>, in terms of spray penetration length. These models were purposely tuned and at the end, it was seen that the combination of new spray model and calibrated turbulence models had better results than the standard ones.

Spray structures of diesel and gasoline sprays in a CI engine were compared by Kim and Kim<sup>[27]</sup>. Gasoline and diesel were substituted by iso-octane and n-heptane respectively. In this study, the evaporation model, which is a significant one for the simulations of liquid-vapor phase change under evaporating conditions, was tuned based on the fuel distillation curves and the numerical results were eventually compared with the experimental ones. The experimental setup shown in Figure (2.2) was used for the Mie-scattering images of the spray. The fuels were firstly filtered and then, they were pumped to the common rail for the fuel injection inside a pressurized chamber. A high-speed camera working synchronically with a light source took the images of the spray during the injection and the images were finally processed via MATLAB.

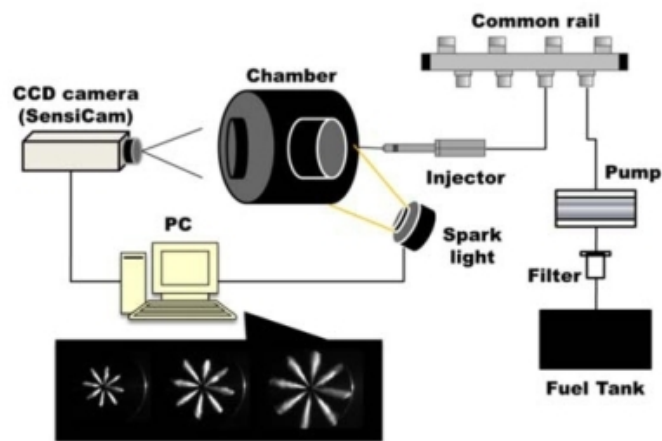


Figure 2.2.: Mie-scattering experimental setup (Source: Kim et al.<sup>[27]</sup>)

The numerical simulations were completed by OpenFOAM. Several spray sub-models including KHRT secondary breakup model and a purposely modified evaporation model were used for the numerical calculations. The simulations were done in a rectangular

domain with the dimensions of 10 mm x10 mm x100 mm. 324,000 number of cells were composed for the simulations and fine mesh configuration was used in the middle of the geometry due to the location of the injector. In conclusion, the experimental and numerical results were compared in terms of spray penetration length. Gasoline spray simulations showed considerable results in contrast with the results of diesel spray simulations because of the high distillation curve of diesel spray, which led to the experimental condition to be a fully non-evaporating one.

The effects of several parameters known as injection pressure, vessel pressure, and vessel temperature on spray penetration length were investigated both numerically and experimentally by Abdelghaffar et al.<sup>[28]</sup>. Additionally, the number of nozzle holes was also examined in this study. Three types of the nozzle with 1-hole, 3-hole, and 5-hole were used under dissimilar conditions. Those circumstances were different vessel temperatures that were 576 K for cold air intake and 721 K hot air intake, varying vessel pressures from 2 MPa to 6 MPa, and changing injection pressure between 60 and 160 MPa. The experiments were done in a single cylinder test engine with a rapid compression and high-speed imaging technique was utilized for obtaining the results. Apart from that, the numerical simulations were completed by KIVA-3V code. Several sub-models including TAB secondary breakup model and O'Rourke collision model were applied for spray structure simulations. A typical cylindrical geometry with 50 mm diameter and 80 mm height was decided as the computational domain. Fine mesh configuration was implemented in the middle of the geometry and the height and width of the smallest in the geometry were respectively 1 mm and 2.5 mm. Consequently, it was understood that spray penetration length and vessel pressure were inversely proportional while spray penetration length and injection pressure were directly proportional to each other. Moreover, the high ambient temperature rose the vaporization rate, which resulted in a shorter spray penetration length. Except for those, the increased number of nozzle holes also influenced the spray penetration length reversely.

A hybrid model for the investigations of diesel sprays was developed by Bianchi and Pelloni<sup>[29]</sup>. The hybrid model included Huh-Gosman<sup>[30]</sup> atomization model and tuned version of the TAB secondary breakup model. In this work, the validation of the hybrid model, the sensitivity tests of grid resolution and the effects of turbulence dispersion on sprays were carried out. KIVA spray analysis codes were used for the numerical modeling. The numerical setup had three dimensional geometry with coarse mesh configuration where the cell size was 1 mm x1 mm x1 mm. Additionally, medium and fine mesh config-

urations were applied for the grid resolutions analysis. Standard  $k-\varepsilon$  model was utilized for the turbulence effects. The numerical results were validated against the experiments of Allocca et al.<sup>[31]</sup>. The extended comparisons showed that the hybrid model had acceptable results for estimations of spray structures. Except for that, better predictions were obtained when smaller cells were composed in the geometry.

The simulations of non-evaporating diesel sprays injected by a single-hole injector and comparisons of them with experimental measurements were done by Chaudhry et al.<sup>[32]</sup>. A cylindrical geometry was generated for the spray simulations. Rosin-Rammler particle distribution model, O'Rourke collision model, and WAVE breakup model were used as the sub-models for creating the numerical model of spray.

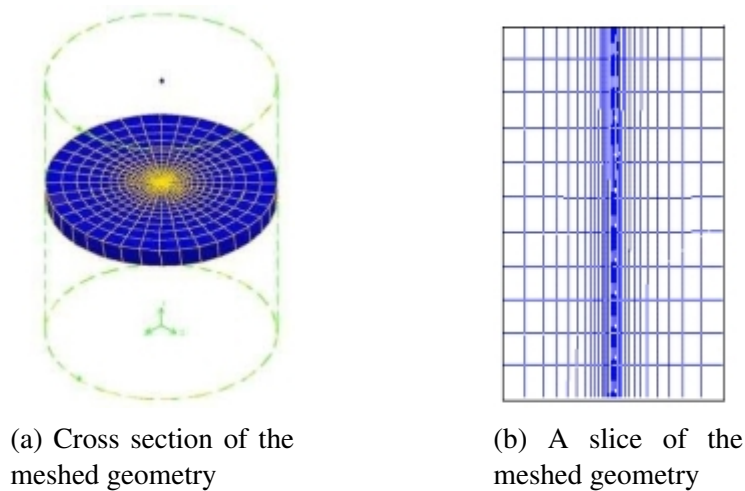


Figure 2.3.: Cross section and the slice of the domain (Source: Chaudhry et al.<sup>[32]</sup>)

The numerical results were compared with the experimental measurements of Mirza<sup>[33]</sup>. It was seen that the numerical and experimental values showed a perfect match in terms of spray penetration length. Another conclusion was that the chamber pressure and particle distribution influenced the spray shape significantly. Furthermore, the penetration value decreased due to rising chamber pressure and increased because of advancing nozzle diameter.

Another investigation of non-evaporating diesel sprays was presented by Kaario et al.<sup>[34]</sup>. Spray simulations were completed by STAR-CD and numerical results were validated against the experimental ones. The experiments were done in a constant volume chamber filled with nitrogen at the room temperature. The chamber was pressurized in the range of 1.06 MPa-3.5 MPa and marine fuel oil was used as the working fluid. A

high-speed camera took pictures of the spray structures for obtaining the experimental results. In order to compose numerical spray structures, WAVE and ETAB breakup models were implemented in a cylindrical domain divided into 16800 cells and the results of those numerical simulations were compared with the experimental ones in terms of spray penetration length, SMD, and spray width. The models showed a good match with the experimental penetration length but they could not accomplish to predict the SMD and spray width properly.

Similar to the previously explained studies, simulations of non-evaporating diesel sprays by using WAVE and KHRT breakup models were performed by Larimi et al.<sup>[35]</sup>. The results of the spray simulations were compared with the data of non-evaporating spray experiments done by Larimi<sup>[36]</sup>. Different from other investigations, this work presented the effect of fuel viscosity on droplet size and the results were compared in terms of spray penetration length and SMD. Two types of fuel namely marine fuel oil and light fuel oil were determined as test fluids. Those were injected into a chamber filled with nitrogen. In addition to the chamber, the test rig had other instruments including a camshaft, a fuel injection pump, an injection valve, and a fuel injector. Since different fuels were used in the experiments, the speed of the camshaft were calibrated based on the fuel properties.

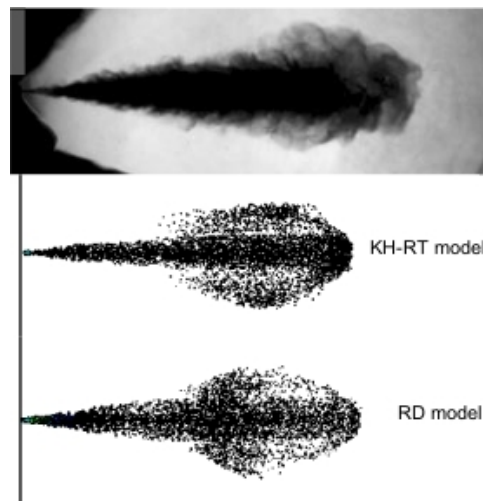


Figure 2.4.: Experimental and numerical spray structures. (Source: Larimi et al.<sup>[35]</sup>)

A typical cylindrical geometry with 100 mm diameter and 100 mm length was used as the computational domain. The standard  $k-\varepsilon$  turbulence model was applied with WAVE and KHRT breakup models for creating a numerical a spray structure. The final

results indicated that both models predicted the spray penetration length adequately, yet KHRT model estimated the droplet size for different fuels better than WAVE model. On the other hand, WAVE breakup model had a better spray structure than KHRT breakup.

In addition to spray penetration length, droplet size, and spray structure analysis, momentum flux is also an important parameter. The momentum flux of diesel sprays was both experimentally and numerically examined by Postrioti et al.<sup>[37]</sup>. The experimental measurements were done by a test rig that had a common rail, high-speed camera, and instantaneous injection rate meter. Moreover, the numerical model of spray was composed via Reitz-Diwakar breakup model, the  $k-\varepsilon$  high Reynolds turbulence model. In this work, the results of the simulated diesel spray that was an impacting jet on a target were compared with the time-dependent global momentum flux measurements. In order for the comparisons, the same global momentum flux data was also used in a similar numerical work done by Postrioti and Battistoni<sup>[38]</sup>. In this work, a free jet was configured and the momentum balance equation was derived for the resultant total force calculation at a fixed distance. Apart from global momentum flux measurements, Postrioti et al.<sup>[39]</sup> measured the spatial momentum flux distribution of a local spray and investigated it numerically. Both numerical and experimental measurements demonstrated satisfactory results in comparison with the global momentum flux measurements of them.

## **2.2. Previous Studies of GDI Sprays**

Numerical simulation of GDI sprays is good way to understand the gasoline spray behavior under different circumstances and they have been implemented for few decades. Actually the first simulations were done for diesel sprays, as the starting point of direct injection technologies came from there. However, the same methods and modified versions of those methods have been started to be used for the investigations of GDI sprays. Moreover, they lead the creation of new models.

In order to have a better estimation and understanding of fuel sprays, researchers validated their simulations based on different parameters that are spray angle, spray penetration, SMD and momentum flux. De Vita and Allocca<sup>[40]</sup> performed numerical and experimental analyses of hollow-cone sprays formed by pressure swirl injectors for DISI engines. The experimental measurements were completed in an optically accessible chamber that was filled with nitrogen. Sprays were injected into that vessel by an electroni-

cally controlled injection system and the images of spray structures were captured by a CCD camera. KIVA-3V code with simplified liquid sheet atomization model and Rosin-Rammler distribution model was used to simulate different sprays generated by two injectors with dissimilar initial angles. The results indicated that the ambient pressure influenced the spray structure, unlike injection pressure. On the other hand, rising injection pressure increased the spray penetration length. Apart from those, numerical results were compared with the empirical results in terms of spray penetration length and spray cone angle. The model seemed to predict fairly but it was needed to be improved by adding new sub-models.

Rotondi and Bella<sup>[41]</sup> studied the problems related to the mixture formation in GDI engines. A numerical technique was used for the investigation of a hollow cone fuel spray's atomization originated by a high pressure swirl injector. The model was created based on a previous Diesel atomization model in which the effects of Weber number changes on atomization were examined and it was validated by comparing spray penetration data and spray morphology with experimental results.

Another numerical study related to atomization and air/fuel mixture preparation under GDI conditions was done by Banerjee and Kumar<sup>[42]</sup>. Performance of a single hole GDI injector was firstly analyzed and the effects of ambient pressure, temperature, temperature of the injected fuel on liquid and vapor penetration lengths were examined. Blob injection model and WAVE breakup model were used for performing the numerical simulation in a cylindrical domain with 60 mm diameter and 90 mm length.

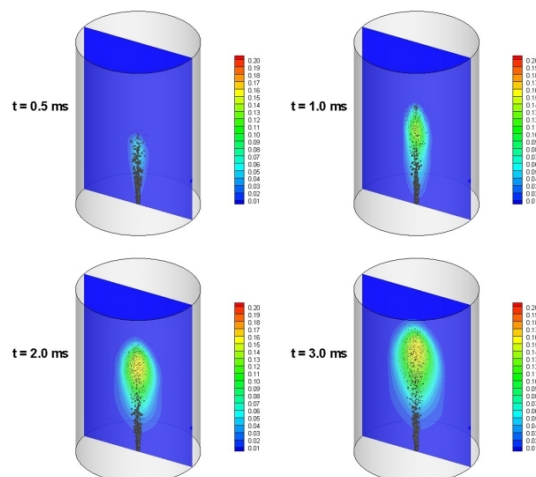


Figure 2.5.: Numerical study of spray evolution (Source: Banerjee et al.<sup>[42]</sup>)

The results of the numerical simulations illustrated that ambient temperature and pressure had non-negligible effects on spray penetration length, yet the spray penetration length was not highly influenced by the fuel temperature. Faster spray penetration was also observed at the beginning of the injection due to the larger size of droplets that broke up into smaller ones in the following stages. As the small droplets had a tendency to evaporate, there was always a vapor plume seen around the spray. Additionally, the air/fuel mixture preparation for a multi-hole GDI injector under simplified engine conditions was also studied.

Suh and Rutland<sup>[43]</sup> also focused on air/fuel mixture preparation under a wide range of GDI engine conditions. Development of hollow cone sprays generated by a high pressure swirl injector was investigated by implementing simulations via KIVA-3V code with Linearized Instability Sheet Atomization (LISA), spray collision, coalescence, breakup and drop drag models.

Cavicchi et al.<sup>[44]</sup> analyzed the spray momentum flux of a single hole GDI research injector with a diameter  $d = 0.2\text{mm}$  and length to diameter ratio  $L/D = 3$ . The experimental work contained the analysis of injection rate, Phase Doppler Anemometry, and spray visual image. A 3-D CFD model of the injector was developed and the results of the numerical model were compared with the experimental data in terms of spray penetration curve, overall shape, droplet sizing, and velocity. The validated numerical model was again utilized for the spray momentum simulations and the numerical results were compared with the experimental data for dissimilar values of the main measurement parameters that are target size, nozzle/target distance, discharge ambient pressure. Unlike other works, a purposely calibrated Rosin-Rammler distribution model was used as a primary breakup model and Reitz-Diwakar model was applied as a secondary breakup model in the numerical simulations. The simulations were completed in an environment where the mesh configuration is fine near-nozzle region and medium in the spray region. Comparisons of the numerical and experimental data indicated that the estimations of the developed CFD model were correct and it described the phenomena of experiments truly.

Apart from the works related to air/fuel mixture preparation and spray momentum measurements, Huang<sup>[4]</sup> investigated the hollow cone sprays formed by a pintle-type GDI injector via OpenFOAM. The liquid properties of gasoline were added to OpenFOAM code and several sub-models including LISA, TAB, Reitz-Diwakar, KHRT, Rosin-Rammler and O'Rourke were modified, validated, and applied in the numerical simulations. A cylindrical geometry with 170 mm diameter and 205 mm length was used as the numer-

ical domain. Three different mesh configurations namely coarse, medium, and fine was applied to divide geometry into cells. The coarse mesh configuration had 131,250 cells in the vicinity of the nozzle whilst medium and fine ones had 1,108,230 and 1,754,400 cells respectively. Besides numerical setup, the experimental setup was equipped with an optically accessible chamber, lighting system, a high-speed camera, and a phase Doppler anemometry (PDA) system. At the end, SMD and spray penetration evaluated by the simulations were compared with the experimental data.

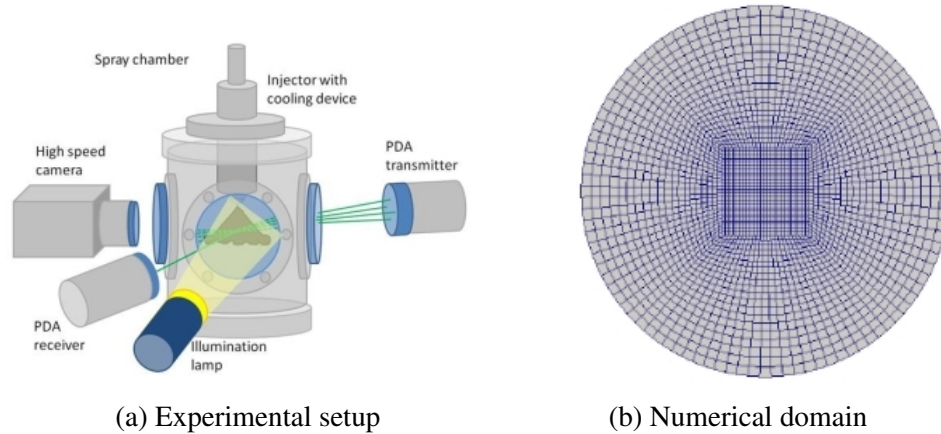


Figure 2.6.: Experimental and numerical setup. (Source: Huang<sup>[4]</sup>)

Furthermore, flash-boiling is also a significant issue for engine sprays that has been examined under different conditions. Price et al.<sup>[45]</sup> studied flash-boiling of n-Pentane and iso-Octane sprays generated by six-hole GDI injector. Lagrangian particle tracking method was used in this numerical model and evaporation model for superheated drops was applied via STAR-CD code. Thereafter the computational tool was utilized to simulate flashing sprays. The simulations were completed in an 80 mm<sup>3</sup> cubic numerical domain that had cells with size changing between 0.5 mm and 3mm. RNG k- $\epsilon$  turbulence model, flash evaporation model, Reitz-Diwakar drop breakup model and O'Rourke droplet collision model were implemented to simulate the fuel spray. The effects of ambient pressure, fuel temperature, initial drop size, heat transfer coefficient and breakup models on flashing and non-flashing sprays were investigated and the computational results were validated against experimental spray penetration length and SMD data measured previously. The results indicated that adjusting the parameters of the model affected the parameters used for the comparisons but it was not valid for the flashing sprays. Nevertheless, the flash boiling sprays were significantly influenced by varying initial droplet



diameter, heat transfer coefficient, and droplet collisions.

Numerical and experimental examinations of the multi-hole GDI sprays under flash-boiling conditions were done by Khan et al.<sup>[46]</sup>. A new flash-boiling model was developed due to the incapability of the spray formation model in flashing spray simulations. Additionally, Rosin-Rammler distribution model was implemented for drop size distribution. ETAB (Enhanced Taylor Analogy Breakup) was applied as a secondary breakup model and a modified O'Rourke collision model was added for estimating droplet collisions. Except for those sub-models, the standard  $k-\varepsilon$  turbulence model was used for the effects of turbulence on the spray. The numerical domain was decided as a rectangular prism with 180 mm length. Adaptive mesh refinement was utilized in the spray zone and coarse mesh refinement was applied near boundaries of the geometry. The parameters of the distribution model and secondary breakup model were estimated based on the experimental data measured by Khan et al.<sup>[47]</sup>. The experiments were done in a constant volume chamber. High-speed images of the sprays were taken for identifying liquid penetration, vapor penetration, and spray cone angle under different engine conditions. The effects of various chamber conditions on spray structures were also investigated besides other parameters. At the end, the experimental and numerical results were compared based on spray structure and spray penetration length and it was determined that the prediction capability of the numerical model for flash-boiling sprays was acceptedly well.

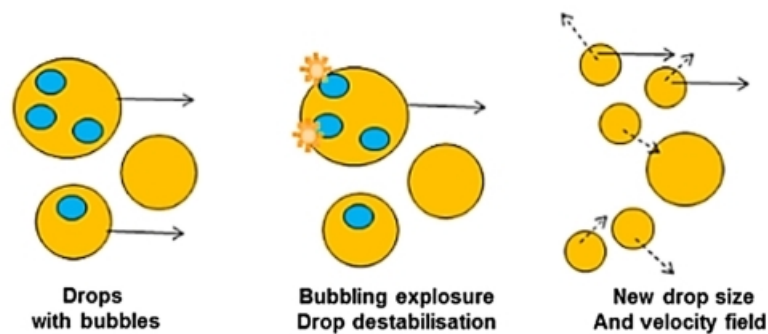


Figure 2.7.: Representation of flashing drops. (Source : Khan et al.<sup>[46]</sup>)

Another flash-boiling model that contains the bubble nucleation, growth, and disruption in the nozzle orifice and injected fuel droplets was constructed by Kawano et al.<sup>[48]</sup>. The model was applied to study spray characteristics of a multi-component fuel under flashing and non-flashing conditions numerically. The simulations were performed

in a constant cylindrical domain with 60 mm diameter and 100 mm length by KIVA-3V code. The chamber was pressurized to 1 bar with nitrogen at 440 K. Fuel injection was completed with 103.164 m/s injection velocity at three dissimilar injection temperatures. A fuel injector with a diameter  $d = 0.2\text{mm}$  was used for the injection process. The results of the model were validated against experimental ones measured in a constant volume chamber under the same conditions mentioned for the numerical simulations except for 15 MPa injection pressure instead of the injection velocity used for numerical simulations. Eventually, it was seen that the developed model was good at estimating the flash-boiling sprays and the results showed that the evaporation was promoted by flash-boiling that led to shorter penetration length.

The flash-boiling spray study of Gulec et al.<sup>[49]</sup> was divided into two parts. Firstly, they investigated the sprays at low temperatures and high ambient pressure conditions where the liquid spray absorbs heat from surroundings and undergo flashing condition. Then, superheated and compressed liquid fuel at 100 bar was injected into an environment at vacuum pressure that can be faced in DISI engines running at low load warm conditions. A newly developed hybrid breakup model and Pilch-Erdman breakup model were applied for numerical simulations besides Rosin-Rammler distribution model and flash-evaporation model. Fuel sprays were simulated in an cylindrical geometry that was separated into cells by three different mesh configurations. Coarse mesh configuration had 60,000 cells while medium and fine mesh configurations had 180,000 and 400,000 cells respectively. The simulation plan was composed based on the experimental study of Postrioti et al.<sup>[23]</sup> and numerical results were compared with those experimental measurements.



Figure 2.8.: The single-hole research injector. (Source: Cavicchi et al.<sup>[44]</sup>)

The experimental tests were done by a single-hole research injector IHP-293 manufactured by Magneti Marelli. The injector had a 0.2 mm diameter and 3 length to diameter(L/D) ratio. In order for symbolizing the spray structure, the images of the spray were captured by a high-speed camera. N-heptane was used as the test liquid in both experimental and numerical examinations. As a result of this study, the numerical model seemed good for the predictions of flashing sprays at 0.4 bar and 1 bar vessel pressure; however, the numerical data of spray at 3 bar vessel pressure did not match the experimental data.

Different from the explained studies, Price et al.<sup>[50]</sup> developed a new model, which can be implemented as a zero-dimensional boundary condition for flash-boiling sprays formed by multi-hole injectors. Additionally mesh type sensitivity was also underlined by using uniform Cartesian and a non-uniform polyhedral mesh in that study. Another different approach was described by Bianchi et al.<sup>[51]</sup>. A 1-D flash-evaporation model was developed for providing Lagrangian spray simulation model with the right droplet size to properly estimate the influence of superheating degree on mixture formation.

# CHAPTER 3

## METHODOLOGY

In order for the simulations of single-hole GDI sprays under non flash-boiling and flash-boiling conditions, sprayFoam solver in OpenFOAM software is a powerful tool. The solver is basically working with the principles of Lagrangian-Eulerian multi-phase flow where Lagrangian approach represents the liquid phase (fuel) and Eulerian one represents the gaseous phase (air). The software also provides a large Lagrangian library where different sub-models are located and those can be used for the representation of sprays under dissimilar conditions. For the validation of numerical simulations, two important parameters namely spray penetration and spray angle are mostly taken into account.

In this section, the sub-models implemented for the simulations, modified significant variables that are affecting the behavior of the spray, spray angle calculations and lastly geometry and the meshing type are explicitly described.

### 3.1. Spray Equation

Simulation of a spray is a complex process that consists in calculations of droplet radius  $r$ , droplet velocity  $\vec{u}$ , and droplet temperature  $T$  for each time and each  $\vec{x} = (x, y, z)$  position. As sprays contain millions of droplets, droplet probability density function (PDF) can be used to express the sprays statistically.

$$f(\vec{x}, \vec{u}, r, T, t) d\vec{u} dr dT \quad (3.1)$$

The possible number of droplets at a certain time and a point is represented by Equation (3.1). Here,  $f$  function is a nine-dimensional one (three spatial coordinates, three velocity coordinates, one-dimensional radius, one dimension for temperature, and time) where the velocities are in the interval  $d\vec{u}$  around  $\vec{u}$ , when the radius is in the range of  $dr$  around  $r$ , and the temperature is between the range of  $dT$  around  $T$ . Additionally, more

dimensions should be taken into consideration, if other properties, including droplet deformation and deformation velocity, are desired to be found. The so-called spray equation describes the time evolution of Equation (3.1) in a differential form.

$$\frac{\delta f}{\delta t} + \nabla_{\vec{x}}(f\vec{x}) + \nabla_{\vec{u}}(f\vec{u}) + \frac{\delta}{\delta T}(f\frac{dT}{dt}) + \frac{\delta}{\delta r}(f\frac{dr}{dt}) = \dot{f}_{source} \quad (3.2)$$

In Equation (3.2), the changing rates of droplet size and temperature are indicated by  $dr/dt$  and  $dT/dt$ . Besides,  $\vec{a} = (d\vec{u}/dt)$  shows the acceleration of droplets and the impact of further processes, which can shift the amount of drops, such as breakup mechanisms, collusion, etc., is symbolized by source term  $\dot{f}_{source}$  in Equation (3.2)<sup>[3]</sup>.

## 3.2. Phase Modeling

Fuel injection process is considered as a two-phase flow because it is a combination of liquid phase (fuel droplets) and gas phase (air in the combustion chamber). Hence, each phase is tackled distinctly and whilst the fuel drops are modeled by Lagrangian method, the gas phase is modeled by Eulerian approach.

### 3.2.1. Gaseous Phase

Reynolds Averaged Navier Stokes Equations (RANS) are utilized as an approach to model the transport equations of the gaseous phase. The model contains turbulent scales and the representation of compressible RANS equations is demonstrated below.

$$\frac{\delta \rho}{\delta t} + \frac{\delta \rho \bar{u}_i}{\delta x_i} = S_{mass} \quad (3.3)$$

$$\frac{\delta \rho \bar{u}_i}{\delta t} + \frac{\delta \rho \bar{u}_i \bar{u}_j}{\delta x_j} = \rho g - \frac{\delta \bar{p}}{\delta x_i} + \frac{\delta \bar{\sigma}_{ij}}{\delta x_j} + \frac{\delta \bar{\tau}_{ij}}{\delta x_j} + \bar{S}_{mom} \quad (3.4)$$

$$\frac{\delta \rho \bar{e}}{\delta t} + \frac{\delta \rho \bar{u}_j \bar{e}}{\delta x_j} = -\frac{\delta \bar{u}_j \bar{p}}{\delta x_i} + \frac{\delta \bar{u}_j \bar{\sigma}_{ij}}{\delta x_j} + \frac{\delta \bar{u}_j \bar{\tau}_{ij}}{\delta x_j} + \bar{S}_{energy} \quad (3.5)$$

The symbols above with overhead bars demonstrate the average of those quantities. The terms  $S_{mass}$ ,  $S_{mom}$ , and  $S_{energy}$  are alternately the source terms from the dispersed phase or liquid phase. While  $\rho$  is the density of the gaseous phase,  $p$  stands for the pressure and  $g$  denotes the gravity. The indices  $i$  and  $j$  are used for specifying the directions x,y,and z. Furthermore,  $\sigma_{ij}$  symbolizes the Reynold stress tensor that includes the turbulent eddy viscosity term modeled by k- $\epsilon$  turbulence model. Lastly viscous stress tensor is indicated by  $\tau_{ij}$ .<sup>[46]</sup>

### 3.2.2. Liquid Phase

The liquid phase of the spray is composed by Lagrangian model and Newton's law of motion shown in Equation (3.6) mostly conducts the motion of the drops inside the fuel spray.

$$\frac{1}{6}\rho_p\pi d_p^3\frac{du_p}{dt} = \frac{1}{2}(u_g - u_p)|u_g - u_p|\rho_g C_d \frac{\pi d_p^2}{4} \quad (3.6)$$

In Equation (3.6), the body forces are neglected and  $\rho_p$  represents droplet density,  $d_p$  is the diameter of the droplet,  $u_p$  and  $u_g$  indicate the droplet velocity and gas velocity at the droplet location,  $C_d$  symbolizes the coefficient of drag. After Equation (3.6) is reduced, Stokes drag indicated in Equation (3.7) is derived.

$$\frac{du_p}{dt} = \frac{C_d}{\tau_p}(u_g - u_p) \quad (3.7)$$

$\tau_p$  variable in Equation (3.7) demonstrates the relaxation time of the droplet which is, for instance, the time taken by the droplet to halt totally. Moreover,  $Re_p$  Reynolds number of the droplet is another parameter that has to be considered for the determination of  $C_d$ .<sup>[46]</sup>

$$Re_p = \frac{|u_g - u_p|d_p}{\nu_p} \quad (3.8)$$

$$\tau_p = \frac{\rho_p d_p}{\rho_g C_d |u_g - u_p|} \quad (3.9)$$

$$C_d = \begin{cases} \frac{24}{Re_p}, & Re_p < 0.1 \\ \frac{24(1+\frac{1}{6}Re_p^{2/3})}{Re_p}, & 0.1 < Re_p < 1000 \\ 0.424, & Re_p > 1000 \end{cases} \quad (3.10)$$

### 3.3. Spray Modeling

Considering different conditions of the liquid fuel and combustion chamber, two phase flow of spray occurs when the fuel is injected into the combustion chamber. A sudden phase change happens after highly pressurized liquid fuel enters in a volume at low temperature. Throughout the phase change, bubbles start to form in the liquid droplets and they burst when they reach to their critical size. The explosion of bubbles leads to the atomization of liquid and expansion in the vicinity of the nozzle. The droplets face with physical phenomena namely, drag force, collusion, dispersion, heat transfer and evaporation; therefore, various sub-models, which remark the physical features of the spray, are required for the investigation of fuel sprays.

#### 3.3.1. Rosin-Rammler Droplet Size Distribution Model

Rosin-Rammler expression<sup>[52]</sup> is a suitable representation of droplet size distribution for fuel sprays. It was firstly derived for expressing the particle size distribution of sieved coal dust, but it has a wide range of usage area and spray analysis is just one of them. For droplet size distribution in spray analysis, the cumulative volume form of Rosin-Rammler distribution function is embedded into OpenFOAM libraries.

$$K = 1 - e^{-((\frac{d_{max}-d_{min}}{\delta})^n)} \quad (3.11)$$

In Equation (3.11),  $K$  is the mass or volume fraction of the particles with sizes larger than the subtraction of  $d_{max}$  and  $d_{min}$ . The subtraction expresses the particle size and  $\delta$  is the location parameter of the distribution. Lastly,  $n$  is known as the spread parameter and a change in that has a significant effect on the particle distribution. Spread

parameter ( $n$ ) alters from 1 to 4 and when it is close to 4, the uniformity of the spray shape becomes clear. Moreover, the changes in location parameter ( $\delta$ ) influence the size of the droplets proportionally<sup>[53]</sup>.

### 3.3.2. Reitz-Diwakar Breakup Model

Reitz-Diwakar<sup>[54]</sup> breakup model is the secondary breakup model in default Lagrangian library of sprayFoam solver. In that model, breakup happens, when a critical droplet Weber number  $We$  has been exceeded<sup>[55]</sup>. Weber number is a vital dimensionless number for the breakup of the liquid drops. There are several breakup mechanisms, which have been explained in Section (1.4.2), depending on the the relative velocity between the liquid drop and surrounding gas, and therefore dependent on Weber number. This breakup model distinguishes between two breakup mechanisms that are bag and stripping breakup.

$$We = \frac{\rho_g \cdot u_{rel}^2 \cdot D}{\sigma} \quad (3.12)$$

$$Re = \frac{2 \cdot u_{rel} \cdot D}{\nu} \quad (3.13)$$

$$\text{Bag Breakup, } We > 6 \quad \text{Stripping Breakup, } \frac{We}{\sqrt{Re}} > 0.5 \quad (3.14)$$

Regardless of those breakup regimes, the reduction of the droplet diameters is assumed to be found by Equation (3.15),

$$d_p = \left( \frac{dt}{\tau} d_{st} + d_p \right) / \left( 1 + \frac{dt}{\tau} \right) \quad (3.15)$$

where  $d_p$  is the droplet diameter prior to breakup,  $d_{st}$  is the new diameter for the stable droplet and  $\tau$  is the corresponding lifetime of the unstable droplets. Regarding the breakup regimes, the values of  $\tau$  and  $d_{st}$  are calculated by using Equations (3.16, 3.17) for bag breakup and Equations (3.18, 3.19) for stripping breakup regime.

$$\tau_{bag} = C_b \cdot \sqrt{\frac{\rho_g d D^3}{\sigma}} \quad (3.16)$$



$$d_{st,bag} = \frac{2C_{bag}\sigma}{\rho_l u_{rel}^2} \quad (3.17)$$

$$\tau_{strip} = \frac{C_s D}{u_{rel}} \sqrt{\frac{\rho_g}{\rho_l}} \quad (3.18)$$

$$d_{st,strip} = \frac{(2C_{strip}\sigma)^2}{\rho_l^2 u_{rel}^3 \nu} \quad (3.19)$$

The original droplet is broken up into a bunch of smaller droplets when one of the breakup criteria is fulfilled longer than the corresponding breakup time for a drop class. The child droplets have the same size and it is decided from equalizing the respective breakup criterion (Equation (3.16) or Equation (3.18)) to its vital value and by resolving it for the droplet diameter. Therefore, it is supposed that the new child droplets are preliminarily in a stable state. Moreover, the amount of child droplets  $N_{d,child}$  originated from disintegration of parent drops is determined by mass conservation rules<sup>[56]</sup>.

$$N_{d,child} \cdot d_{child}^3 = N_{d,parent} \cdot d_{parent}^3 \quad (3.20)$$

### 3.3.3. Pilch-Erdman Breakup Model

Considering the liquid droplets at high velocity flow field, which are less dense than the other droplets, Pilch and Erdman derived this model<sup>[57]</sup>. The breakup of droplets is mostly induced by aerodynamic and surface tension forces. The ratio of those forces is represented by Weber number  $We$ . Additionally, the breakup model also presents the triangular relationship of critical Weber number, breakup time and velocity history data. The so-called Ohnesorge number indicated in Equation (1.11) was used to compute the critical Weber number shown in Equation (3.21).

$$We_{cr} = 12 \cdot (1 + 1.077 \cdot Oh^{1.6}) \quad (3.21)$$

The value of Weber number has a significant role in the breakup tendency of the droplets and the probability of droplet breakup increases when it becomes higher. Thus, the Weber number is a key factor for the determination of breakup modes and after it exceeds the critical Weber number, the following relations are utilized to find out total breakup time.

$$T_b = \begin{cases} 6(We - 12)^{-0.25}, & 12 < We < 18 \\ 2.45(We - 12)^{-0.25}, & 18 < We < 45 \\ 14.1(We - 12)^{-0.25}, & 45 < We < 351 \\ 0.766(We - 12)^{-0.25}, & 351 < We < 2670 \\ 5.5, & We > 2670 \end{cases} \quad (3.22)$$

Thereafter the dimensionless breakup time  $T_b$  is used for calculating the characteristic breakup time  $\tau_b$  by Equation (3.23)<sup>[49-58]</sup>.

$$\tau_b = T_b \left( \frac{\rho_l}{\rho_g} \right)^{0.5} \left( \frac{u_{rel}}{D} \right) \quad (3.23)$$

### 3.3.4. TAB Breakup Model

TAB mathematical model, that was introduced by O'Rourke and Amsden<sup>[59]</sup>, is represented by basic mass, spring and damper system. It represents the resemblance of an oscillation drop, which goes into a gaseous environment with a relative velocity  $u_{rel}$ , to a forced oscillating mass-spring system. In that model, aerodynamic forces corresponds to the forcing term, liquid viscosity stands for the damping force, and surface tension symbolizes restoring force.

In Fig (3.1), maximum radial distortion from the spherical surface is represented by  $x$  and deformation parameter is  $y = 2x/r$ . The drop distortion formula is expressed in Equation (3.24),

$$\ddot{y} + \frac{5\mu}{\rho_d r^2} \dot{y} + \frac{8\sigma}{\rho_d r} y = 2\rho_g ||u_{rel}^2|| 3\rho_d^2 \quad (3.24)$$

where  $\mu$  is drop viscosity,  $\sigma$  is surface tension, and  $u_{rel}$  is the relative drop-gas velocity.

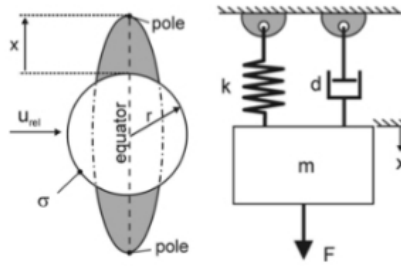


Figure 3.1.: TAB model (Source: Baumgarten<sup>[31]</sup>)

### 3.3.5. Pilch-Erdman/TAB Hybrid Breakup Model

The combination of Pilch-Erdman and TAB secondary breakup models was applied to create hybrid breakup model by Gulec et al.<sup>[49]</sup>. This breakup model was composed with the aim of decreasing the average droplet diameter under the condition of the higher level of the breakup. The model was tested under dissimilar circumstances and it estimated the results reasonably.

$We$  number described in Equation (1.12) is a key factor in this model to determine the breakup regimes of the droplets. This breakup model uses the working principle of Pilch-Erdman and TAB breakup models with some modifications. Unlike Pilch-Erdman correlation, this breakup model promotes a further breakup of droplets when  $We < 12$  where TAB breakup model starts working. This leads to smaller droplets and enhanced evaporation. The working principle of the hybrid model is clearly explained in the following table.

Table 3.1.: Hybrid breakup model<sup>[60]</sup>

TAB	$We < 12$
Vibrational mode	$12 < We < 18$
Bag regime	$18 < We < 45$
Chaotic regime	$45 < We < 100$
Stripping regime	$100 < We < 1000$
Catastrophic regime	$1000 < We$

### 3.3.6. Trajectory Model

Trajectory Model is one of the methods to simulate the collision of the droplets. Unlike O'Rourke collision model<sup>[61]</sup>, directions of the parcels are taken into account in this model. The intersection points of the parcels are firstly calculated by Trajectory Model before the collision. It also computes the alignment velocity vector, which ensures the locomotion of droplets towards each other.

$$u_{align} = (u_{p2} - u_{p1}) \frac{x_{p2} - x_{p1}}{|x_{p2} - x_{p1}|} \quad (3.25)$$

In Equation (3.25),  $u_{p1}$  and  $u_{p2}$  represent the respective velocities of the droplets while  $x_{p1}$  and  $x_{p2}$  stand for the respective positions of the droplets.

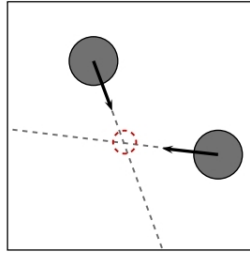


Figure 3.2.: Collision in Trajectory Model<sup>[62]</sup>

The collision distance between two droplets is found by alignment velocity and simulation time step  $\Delta t$ , if the droplets are in the position of the collision. The collision takes place when the parcel comes to the intersection point that is calculated in the present simulation time step. Otherwise, the computations are completed again for the next time step<sup>[46]</sup>.

$$u_{align} \Delta t > (x_{p2} - x_{p1}) - 0.5(d_{p2} - d_{p1}) \quad (3.26)$$

### 3.3.7. Evaporation and Heat Transfer Model

The evaporation model presented by Zuo et. al<sup>[63]</sup> is a powerful model to simulate the evaporation of the droplets under flashing and non-flashing conditions because that model contains not only the heat transfer from superheated droplets itself, but also the heat transfer from the ambient. The internal heat flux  $Q_1$  and heat transfer coefficient  $\alpha$  are based upon the experimental correlations.  $H_v$  is the latent heat of the fluid and the superheat degree  $\Delta T$  is described as  $T_d - T_b$ .

$$Q_1 = \pi \cdot r_d^2 \cdot \alpha \cdot (T_d - T_b) \quad (3.27)$$

The summation of sub-cooled ( $M_{sc}$ ) and superheated evaporation ( $M_{sh}$ ) rates gives us the total evaporation ( $M_t$ ) rate at superheated conditions.

$$\frac{dM_t}{dt} = \frac{dM_{sc}}{dt} + \frac{dM_{sh}}{dt} \quad (3.28)$$

The calculation of sub-cooled evaporation rate is demonstrated in Equation (3.29),

$$\frac{dM_{sc}}{dt} = r_d \cdot \pi \cdot \rho \cdot D \cdot \ln\left(\frac{1 - Y_{f,\infty}}{1 - Y_{f,r}}\right) \cdot Sh \quad (3.29)$$

where  $D$  is the diffusivity coefficient of the fuel vapor in air,  $Y_{f,r}$  represents the fuel vapor mass fraction at the droplet surface,  $Y_{f,\infty}$  symbolizes fuel vapor mass fraction outside of the boundary layer, and  $Sh$  is the Sherwood number that stands for risen mass transport due to relative velocity between the gas surrounding the droplet and the droplet's itself. It is basically calculated via Froessling correlation<sup>[46]</sup>.

$$Sh = 2 + 0.6Re_p^{1/2}Sc^{1/3} \quad (3.30)$$

$$Sc = \frac{\mu}{\rho D} \quad (3.31)$$

In order to obtain the heat transfer correlation of Ranz-Marshall<sup>[64]</sup>, which is used for finding the Nusselt number  $Nu$ , the dimensionless Schmidt number  $Sc$  in Equation (3.30) is replaced with Prandtl number  $Pr$ .

$$Nu = 2 + 0.6Re_p^{1/2}Pr^{1/3} \quad (3.32)$$

$$Pr = \frac{\mu C_p}{k} \quad (3.33)$$

Those correlations were acquired from the experiments of vaporizing single-component droplets at atmospheric pressure and temperate surrounding temperatures with low transfer rates<sup>[64]</sup>. In addition to them, the heat transfer coefficient  $\alpha$  is defined as a function of superheat degree  $\Delta T$ ,

$$\alpha = \begin{cases} 760 \cdot \Delta T^{(x_1)}, & 0 \leq \Delta T \leq 5 \\ 27 \cdot \Delta T^{(x_2)}, & 5 \leq \Delta T \leq 25 \\ 13800 \cdot \Delta T^{(x_3)}, & \Delta T \geq 25 \end{cases} \quad (3.34)$$

where the exponents  $x_1$ ,  $x_2$ , and  $x_3$  are respectively 0.26, 2.33, and 0.39 based on the study of Zuo et. al<sup>[63]</sup>.

In order for finding the total evaporation rate at the end, the superheated evaporation rate is needed to be calculated based on Equation (3.35).

$$\frac{dM_{sh}}{dt} = \frac{Q_1}{H_v} \quad (3.35)$$

### 3.3.8. $k-\varepsilon$ Turbulence Model

The standard  $k-\varepsilon$  model is a two equation model where  $k$  is the turbulence kinetic energy and  $\varepsilon$  is the turbulence dissipation rate.

In turbulent flows, the kinetic energy of the main flow can only be converted into turbulent kinetic energy by the large eddies; however, turbulent kinetic energy is only dispersed in the smallest eddies. In accordance with the energy cascade model, the large-scale eddies transmit the turbulent energy to smaller ones until it is eventually dispersed in the smallest eddies<sup>[3]</sup>.

The  $k - \varepsilon$  model in OpenFOAM is defined by Equation (3.36) and Equation (3.37) that are respectively known as turbulent kinetic energy equation and dissipation equation<sup>[65]</sup>.

$$\frac{D}{dt}(\rho k) = \nabla \cdot (\rho D_k \nabla k) + G_k - \frac{2}{3}\rho(\nabla u)k - \rho\varepsilon + S_k \quad (3.36)$$

$$\frac{D}{dt}(\rho\varepsilon) = \nabla \cdot (\rho D_\varepsilon \nabla \varepsilon) + \frac{C_1 G_k \varepsilon}{k} - \frac{2}{3}(C_1 + C_{3,RDT})\rho(\nabla u)k - C_2 \rho \frac{\varepsilon^2}{k} + S_\varepsilon \quad (3.37)$$

### 3.3.9. Realizable k- $\varepsilon$ Turbulence Model

Realizable  $k - \varepsilon$  turbulence model was derived based on the standard  $k - \varepsilon$  model by Shih et al.<sup>[66]</sup>. Therefore, it consists of two main equations namely dissipation equation and kinetic energy equation like the standard model. The realizability restrictions, which are the inequality of Schwarz for turbulent shear stress and the positivity of normal Reynolds stress, underlie the kinetic energy equation (Equation (3.38)). On the other hand, at large Reynolds number, the dynamic equation of the mean-square vorticity fluctuation is the underlying factor of turbulence dissipation equation (Equation (3.39))<sup>[67]</sup>.

$$\frac{D}{dt}(\rho k) = \nabla \cdot (\rho D_k \nabla k) + \rho G - \frac{2}{3}\rho(\nabla u)k - \rho\varepsilon + S_k \quad (3.38)$$

$$\frac{D}{dt}(\rho\varepsilon) = \nabla \cdot (\rho D_\varepsilon \nabla \varepsilon) + C_1 \rho |S| \varepsilon - C_2 \rho \frac{\varepsilon^2}{k + (\nu\varepsilon)^{0.5}} + S_\varepsilon \quad (3.39)$$

Additionally, the turbulence viscosity is evaluated by Equation (3.40),

$$\nu = C_\mu \frac{k^2}{\varepsilon} \quad (3.40)$$

where the coefficient  $C_\mu$  is computed by Equation (3.41).

$$C_\mu = \frac{1}{A_0 + A_s U^* \frac{k}{\varepsilon}} \quad (3.41)$$

The  $U^*$  term Equation (3.41) is determined by,

$$U^* = \sqrt{S_{ij}S_{ij} + \tilde{\Omega}_{ij}\tilde{\Omega}_{ij}} \quad (3.42)$$

$$\tilde{\Omega}_{ij} = \Omega_{ij} - 2\varepsilon_{ij}\omega_k \quad (3.43)$$

$$\Omega_{ij} = \bar{\Omega}_{ij} - \varepsilon_{ij}\omega_k \quad (3.44)$$

$\bar{\Omega}_{ij}$  term in the previous equation is the mean rotation rate of the reference frame turning with the angular velocity  $\omega_k$ . Moreover, the term  $A_s$  is found by the following equations.

$$A_s = \sqrt{6} \cos \phi \quad (3.45)$$

$$\phi = \frac{1}{3} \arccos(\sqrt{6}\omega) \quad (3.46)$$

$$\omega = \frac{S_{ij}S_{jk}S_{ki}}{\tilde{S}^3} \quad (3.47)$$

$$\tilde{S} = \sqrt{S_{ij}S_{ij}} \quad (3.48)$$

### 3.4. Spray Angle Calculation

Spray angle is an imaginary angle, that is found based on the spray boundaries. As most of the studies was done experimentally, measuring the spray angle was completed via image processing in the previous works. The advantage of numerical studies is that the particles are distributed on a coordinate system. Hence, it is easy to detect the particles, which compose the boundaries of the spray. This makes everything easier and prevents the mistakes such as missing particles while calculating the angle via image processing.

After spray simulation data is obtained from OpenFOAM, it is post-processed via an inhouse code that has been developed for the calculations of spray angle at each time



step. Initially the locations of the particles in the spray for each time step are determined and the spray is investigated in 2D conditions. The most important variable for spray angle calculations is the penetration length of the spray. The penetration length of 95% mass fraction is known for each time step due to the simulation data, so 60% of penetration length is calculated based on the penetration length of 95% mass fraction. That percentage of mass fraction helps to get rid of the oscillations in the data<sup>[68]</sup>. In addition to this, the reason of computing 60% penetration length is that the spray plume is mushroom shaped after this penetration length and a shape like a triangle, which can be gained at 60% of penetration length, is needed for finding the spray angle<sup>[69]</sup>. Hence, the particles up to that penetration are detected and the mass value of each particle is evaluated by using Equation (3.49).

$$m = \rho \cdot n_{particles} \cdot V \quad (3.49)$$

$$V = \frac{4}{3}\pi r^3 \quad (3.50)$$

In Equation (3.49),  $V$  is the volume of particle,  $\rho$  stands for the density of the particle, and  $n_{particles}$  represents the number of particles. The volume of the particle is calculated via Equation (3.50) because the particles are assumed to have a spherical shape.

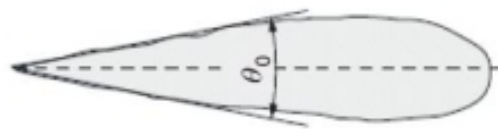


Figure 3.3.: Spray angle for a single-hole GDI injector (Source: Jafarmadar et al.<sup>[70]</sup>)

The total mass is calculated by adding up the particle mass values later on; however, this total mass covers 100% mass fraction. Therefore, the boundaries of the spray should be drawn and they should be increased or decreased based on the mass fraction of spray inside them. When the location values are reviewed, the precision number of them is quite high, so they are rounded to have a shape where particles are sorted side

by side. For creating the boundaries, maximum and minimum values in the horizontal axis are found out at 60% penetration length and the angle is computed basically with the division of endpoints in the horizontal axis to penetration length because the lengths in both vertical and horizontal axes are known. Thereafter the boundary values in the horizontal axes for different penetrations, which are smaller than 60% percent penetration, are calculated by using these penetrations and angle found in the last step. Next step covers the particles outside the boundaries as their mass is going to be subtracted from the total mass to figure out the particle mass fraction inside of the boundaries. If it is smaller than 95% mass fraction, the horizontal boundary values will be bigger than the initial ones and if it is bigger than that mass fraction, the boundaries will change vice-versa. When the mass fraction reaches 95%, the last angles of boundaries are summed up and spray angle is finally calculated.

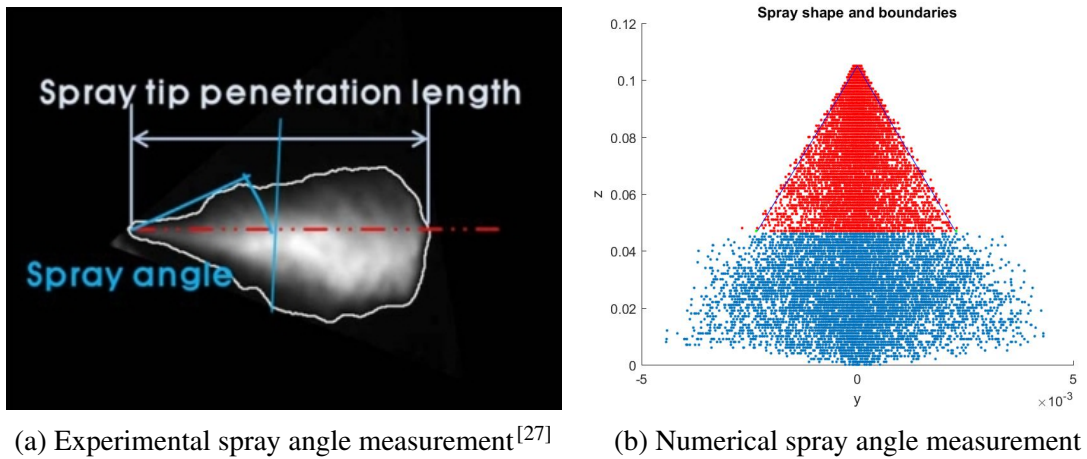


Figure 3.4.: Experimental and numerical spray angle measurement

### 3.5. Numerical Setup

As a first step, a cylindrical domain with 60 mm diameter and 105 mm length was designed and three different grid resolutions namely coarse, medium, and fine were composed based on the work of Gulec et. al<sup>[49]</sup>. The coarse mesh had 58800 cells that were changing between 1 mm and 1.75 mm. The medium mesh contained 160000 cells and cell sizes were at the range of 0.75 mm-1.3 mm in medium mesh resolution. Additionally, there were 437500 cells that varied from 0.6 mm to 0.75 mm in fine mesh configuration.

Besides, a better mesh configuration was also tested but it was seen that the results did not alter. Except for the chamber, the geometrical features of the injector are a single hole diameter with 0.2mm and a hole length-to-diameter ratio  $L/D = 3$ <sup>[23]</sup>.

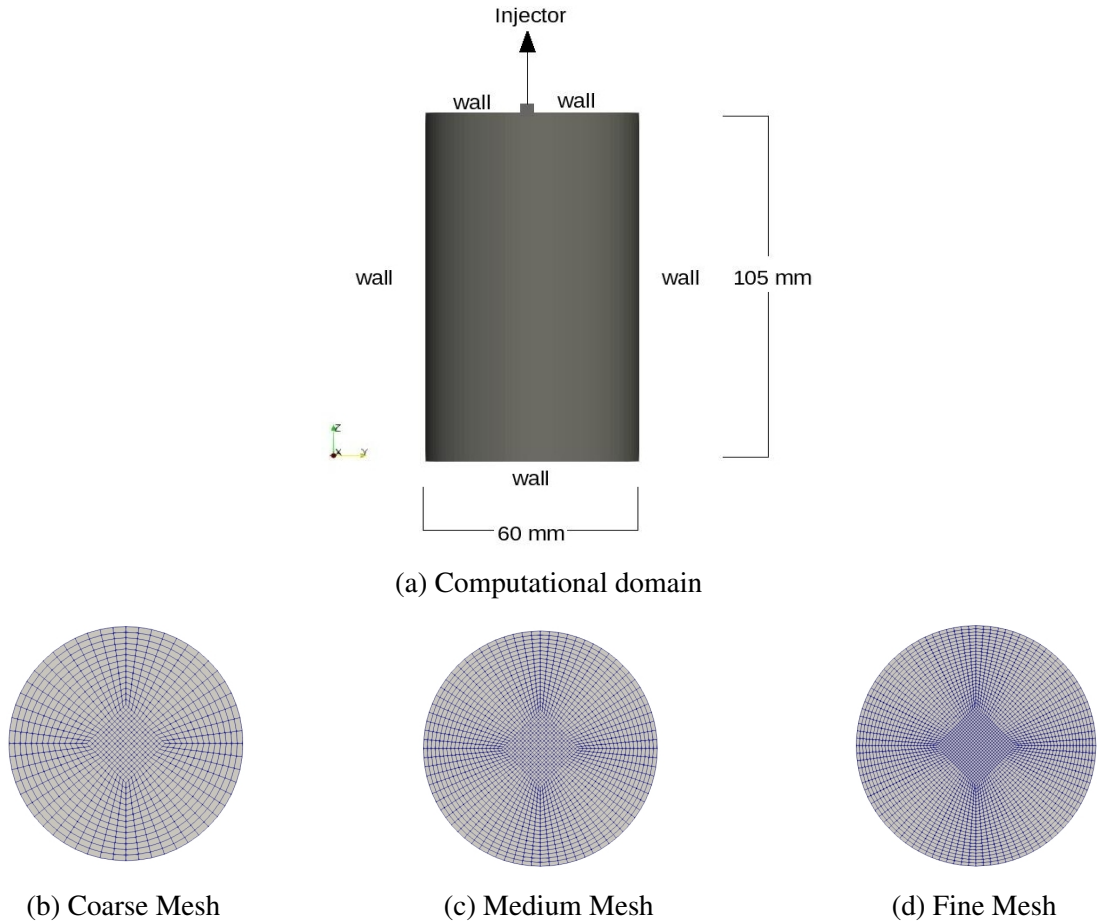


Figure 3.5.: Computational domain and mesh configuration

Table 3.2.: Mesh configuration

Resolution	Number of cells	Mesh size(mm)
Coarse	58800	1-1.75
Medium	160000	0.75-1.3
Fine	437500	0.6-0.75

The simulations were completed with  $2.5\mu s$  time step; however, the results of simulations were divided into two parts in terms of the time step for a better understanding of spray angle measurements just after the start of injection (SOI). In the first part, the time

step was arranged as  $5\mu s$ <sup>[38]</sup> and the results of each  $5\mu s$  were investigated for determining the spray angle. For the second part of the simulation results,  $50\mu s$  time step, which is the default one in OpenFOAM, was used and the spray angle measurements were done for them. Moreover,  $1\mu s$  time step was also tested but the results remained the same with  $2.5\mu s$  time step.

The experimental measurements of the single-hole GDI injector that was numerically simulated in this work were completed for different injection pressures by Postrioti et. al<sup>[23]</sup> and the injection profile of fuel injected with 100 bar pressure was shown in Figure (3.6).

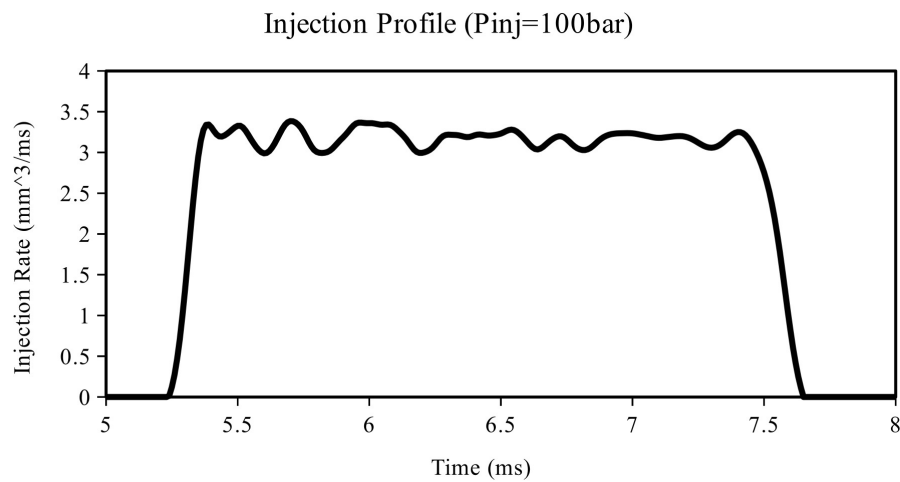
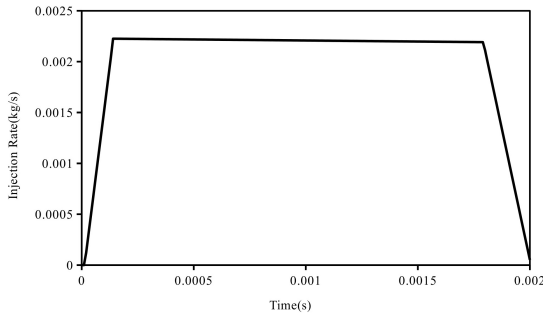
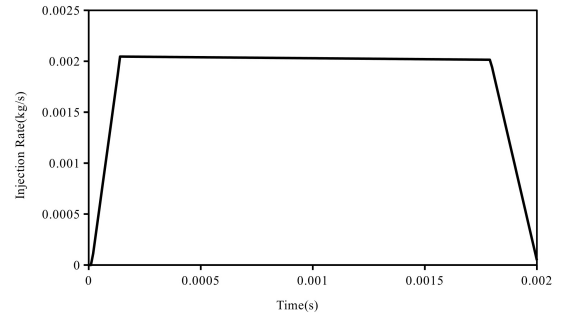


Figure 3.6.: Experimental measurement of the injection profile after SOI<sup>[23]</sup>

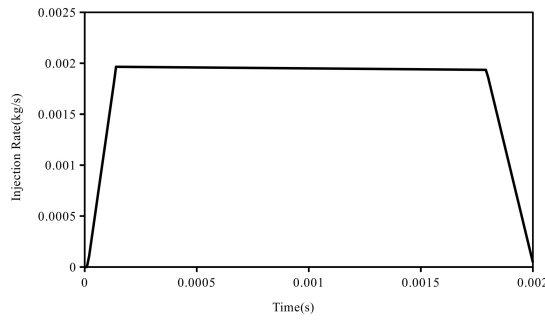
This injection profile was modified based on the fuel temperature and injection pressure, since the density of the fuel alters with respect to the fuel temperature. N-heptane, which is the default fuel type in OpenFOAM, was used and the properties of it were found on the official web-page of NIST laboratories for dissimilar temperatures and 100 bar injection pressure<sup>[71]</sup>. The experimental measurement of the injection profile had a volumetric value. Therefore, it was multiplied by the density of fuel at three different temperatures to acquire total mass and injected mass profile needed for the simulation cases. Eventually, the total mass injected into the chamber varied from 3.5 mg to 4 mg.



(a) Injection Profile at  $T_{fuel}=293K$



(b) Injection Profile at  $T_{fuel}=363K$



(c) Injection Profile at  $T_{fuel}=393K$

Figure 3.7.: Modified injection profiles for different  $T_{fuel}$

Table 3.3.: Density of n-heptane<sup>[71]</sup>

<b><math>P_{inj}=100 \text{ bar}</math></b>	
<b><math>T_{fuel} \text{ (K)}</math></b>	<b><math>\rho_{fuel} \text{ (kg/m}^3\text{)}</math></b>
293	692.82
363	636.90
393	611.77

In addition to the injection profile, the discharge coefficient, which describes the performance of the nozzle, was theoretically calculated for the simulations under different conditions shown in Table (3.4).

$$C_d = \frac{\dot{m}_{inj}}{\rho_{fuel} \cdot u_{Bernoulli} \cdot A_{nozzle}} \quad (3.51)$$

$$u_{Bernoulli} = \sqrt{\frac{2 \cdot (P_{fuel} - P_{air})}{\rho_{fuel}}} \quad (3.52)$$

In Equation (3.51),  $u_{Bernoulli}$  is the maximum initial velocity that is calculated via Equation (3.52),  $\dot{m}_{inj}$  represents the mass flow rate calculated based on the modified injection rate data for different temperatures,  $A_{nozzle}$  symbolizes the surface area of the injector, and  $\rho_{fuel}$  stands for the density of the fuel<sup>[3]</sup>.

Table 3.4.: Simulation cases

Case	T <sub>fuel</sub> (K)	P <sub>vessel</sub> (bar)
1	293	0.4
2	363	
3	393	
4	293	1
5	363	
6	393	
7	293	3
8	363	
9	393	

Another characteristic parameter that is called spray initial angle (SIA) affects not only the spray angle, but also the size of the droplets directly. Spray penetration is also influenced by the initial angle as spray penetrates into a shorter distance when the initial angle is high. In order to calculate the spray initial angle, Heywood's method, which is mostly used for the initial angle calculation for diesel injection sprays, was implemented<sup>[72]</sup>.

$$\tan\left(\frac{\phi}{2}\right) = \left(\frac{4\pi}{A}\right) \cdot \left(\frac{\rho_g}{\rho_l}\right) \cdot f(v) \quad (3.53)$$

$$f(v) = \frac{\sqrt{3}}{6} \cdot (1 - e^{-10v}) \quad (3.54)$$

$$v = \left(\frac{Re_l}{We_l}\right)^2 \cdot \left(\frac{\rho_l}{\rho_g}\right) \quad (3.55)$$

$$Re_l = \frac{u_{inj} D_h}{\nu} \quad (3.56)$$

$$We_l = \frac{u_{inj}^2 D \rho_l}{\sigma} \quad (3.57)$$

To compute the spray initial angle, firstly Reynold number and Weber number for the fluid under different conditions must be known, therefore initial injection velocity should be found by using the regulated injection rate data. Equation (3.58) is the basic explanation of obtaining that value. Surface tension  $\sigma$  and kinematic viscosity  $\nu$  of the fuel are other characteristics of the fuel for calculating the Reynold and Weber number. Furthermore, hydraulic diameter  $D_h$  for the calculation of Reynold number is equal to the length  $L$  of the nozzle.

$$\dot{m}_{inj} = \rho_{fuel} \cdot u_{inj} \cdot A_{nozzle} \quad (3.58)$$

After the theoretical calculations were completed, the discharge coefficient and spray initial angle were found for dissimilar conditions. The results are shown in Table (3.5).

Table 3.5.: Theoretically calculated discharge coefficient and spray initial angle values

<b>T<sub>fuel</sub></b>	<b>293 K</b>			<b>363 K</b>			<b>393 K</b>		
<b>P<sub>vessel</sub></b>	<b>0.4 bar</b>	<b>1 bar</b>	<b>3 bar</b>	<b>0.4 bar</b>	<b>1 bar</b>	<b>3 bar</b>	<b>0.4 bar</b>	<b>1 bar</b>	<b>3 bar</b>
<b>C<sub>d</sub></b>	0.538	0.539	0.545	0.515	0.517	0.522	0.505	0.507	0.512
<b>SIA</b>	1.42	2.24	3.87	1.48	2.34	4.04	1.51	2.39	4.13

Table 3.6.: AtSPR values under different conditions<sup>[23]</sup>

<b>Ambient to Saturation Pressure Ratio (AtSPR)</b>			
<b>Temperature (K)</b>	<b>Pressure (kPa)</b>		
	<b>40</b>	<b>100</b>	<b>300</b>
<b>293</b>	8.47	21.38	64.16
<b>363</b>	0.51	1.28	3.85
<b>393</b>	0.22	0.55	1.65

Based on the simulation cases and AtSPR ranges illustrated in Table (3.6), the sprays in flashing, transient, and non-flashing regions were firstly defined. Since flashing sprays have shorter penetration lengths and higher spray angles than non-flashing sprays, the calculated spray initial angle values for the sprays in the flash-boiling and transient regions were quite low for the simulations. Therefore, spray initial angle values for flash-boiling sprays were assumed bigger than the evaluated ones based on the study of Jafarmadar et. al<sup>[70]</sup>. The effect of spray cone angle on the breakup of a GDI spray was

numerically investigated in that work and the results showed that an increase in the spray cone angle reduces the penetration length and enhances the fuel-air mixing or vice versa. Eventually, the spray initial angle was adjusted as 10 degrees for flashing sprays and 7.5 degrees for the sprays in the transient region based on the estimations from the experimental measurements. Nevertheless, the computed initial angle values were implemented for non-flashing sprays.

In the end, the modifications in sub-models were completed and the parameters of each were determined with respect to both experimental and numerical works done before. Rosin-Rammler model<sup>[52]</sup> was applied for estimation of droplet distribution. As a secondary breakup model, TAB<sup>[59]</sup>, Reitz-Diwakar<sup>[54]</sup>, Pilch-Erdman<sup>[57]</sup> and Hybrid<sup>[49]</sup> models were compared. Additionally, k- $\epsilon$  and realizable k- $\epsilon$  models were utilized as a turbulence model. In order to rise the accuracy of the spray simulations, stochastic dispersion model, in which the velocity is distracted in an unspecific direction with a Gaussian random number distribution, was also implemented. The parameters of those and other sub-models explained in the previous sections are summarized in Table (3.7).

Table 3.7.: Summary of sub-models

<b>Model Name</b>	<b>Parameters</b>
Rosin-Rammler	$d_{\max}=1.5e-4$ , $d_{\min}=1e-6$ , $\delta=1.5e-4$ $n=3$
Reitz Diwakar	$C_{\text{bag}}=0.6$ , $C_b=0.785$ , $C_{\text{strip}}=0.5$ , $C_s=10$
Pilch-Erdman	$B_1=0.375$ , $B_2=0.2274$
Hybrid	$B_1=0.375$ , $B_2=0.2274$
TAB	$y_0=0$ , $\dot{y}_0=0$ , $C_\mu=10$ $C_\omega=8$ , $We_{\text{crit}}=12$
Trajectory	$C_{\text{Space}}=1$ , $C_{\text{Time}}=0.3$
k- $\epsilon$	$C_\mu=0$ , $C_1=1.44$ , $C_2=1.92$ , $C_{3,\text{RDT}}=-0.33$ , $C_k=1$ $C_\epsilon=1.3$
Realizable k- $\epsilon$	$A_0=4$ , $C_2=1.9$ , $C_k=1$ , $C_\epsilon=1.2$



### 3.6. Model Validation

The validation of the numerical model against the experimental data was done for the GDI sprays at 293 K. The reason of choosing this temperature was that the tendency of flashing is the lowest when the fuel is at that temperature. The validations were completed by a modified sprayFoam solver. As sprayFoam was normally designed for diesel spray simulations, discharge coefficient, spray initial angle and injection profile was changed based on the calculations explained previously.

The spray penetration length results of TAB, Reitz-Diwakar, Pilch-Erdman and Hybrid secondary breakup models were firstly compared with the experimental results at 293K fuel temperature and 1 bar vessel pressure. In Figure (3.8), it can be clearly seen that Hybrid and Pilch-Erdman secondary breakup models have almost the same results that are much better than the results of other breakup models. Additionally, there is a very tiny gap between the data of Hybrid and Pilch-Erdman models. Therefore, the estimations of Hybrid model is better than the results of Pilch-Erdman with a very small difference. Those predictions also demonstrate that Hybrid and Pilch-Erdman models are more extensive than other models so they were utilized in the spray simulations.

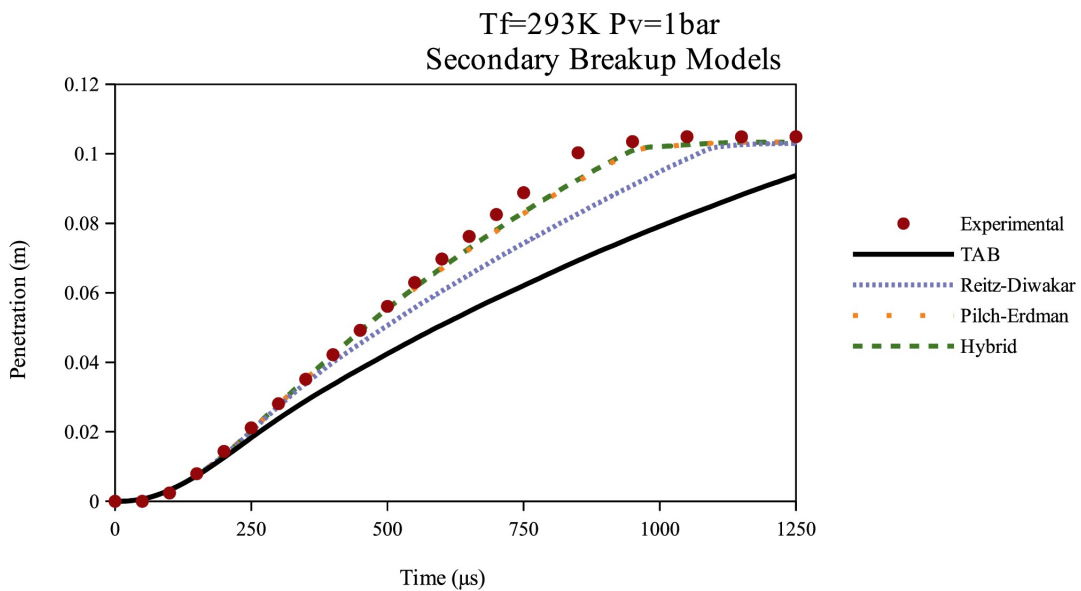


Figure 3.8.: Comparison of secondary breakup models at  $T_{fuel}=293K$ ,  $P_v=1bar$

Besides secondary breakup models, two different turbulence models namely  $k-\varepsilon$  and Realizable  $k-\varepsilon$  were also compared under the same conditions. Figure (3.9) shows that the results are close to each other but Realizable  $k-\varepsilon$  gives better results than standard  $k-\varepsilon$  turbulence model. As a conclusion, it was understood that realizable  $k-\varepsilon$  model works better than standard  $k-\varepsilon$  for the turbulence computations near wall regions. Apart from those, medium mesh configuration was utilized for secondary breakup model and turbulence model tests by considering the time spent for the simulations.

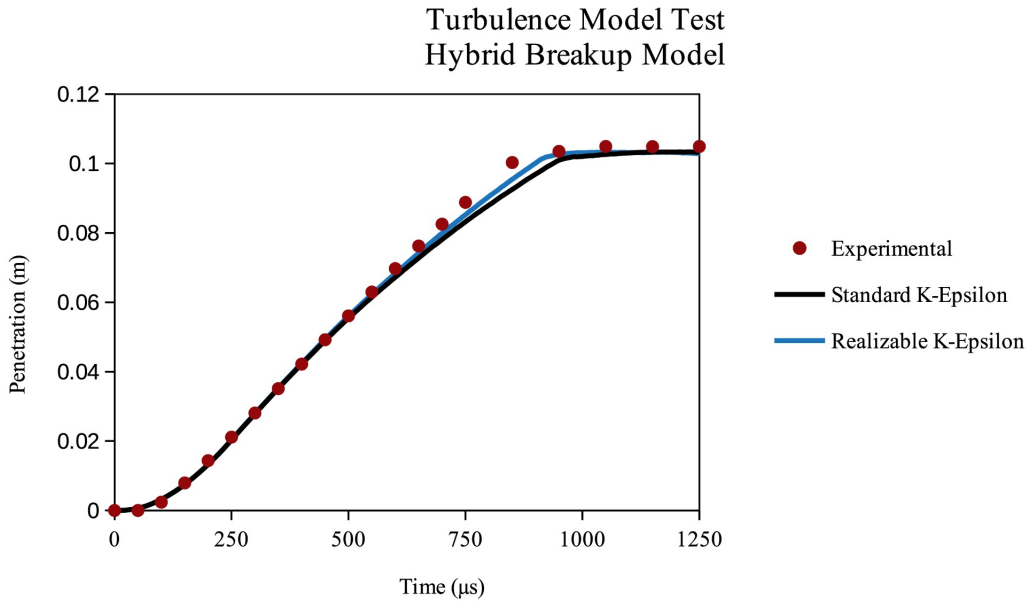


Figure 3.9.: Comparison of turbulence models at  $T_{fuel}=293K$ ,  $P_v=1bar$

After the turbulence model tests were completed, mesh dependency was tested for the configurations mentioned in Section (3.5). An additional mesh size that is bigger than the size of fine mesh configuration was applied and the same results with the fine mesh orientation were obtained. The closest numerical result to the experimental one was acquired by fine mesh configuration, yet there was a small difference between numerical and experimental results from  $600 \mu s$  to  $850 \mu s$ . Figure (3.10) indicates the mesh dependency test data at  $293K$  fuel temperature and  $1 bar$  vessel pressure. Furthermore, a time convergence test was also done with medium mesh configuration for the hybrid model under the same circumstances. Figure (3.11) illustrates the results which are the same for different time steps  $\Delta t = 1e - 6\mu s$  and  $\Delta t = 2.5e - 6\mu s$ .

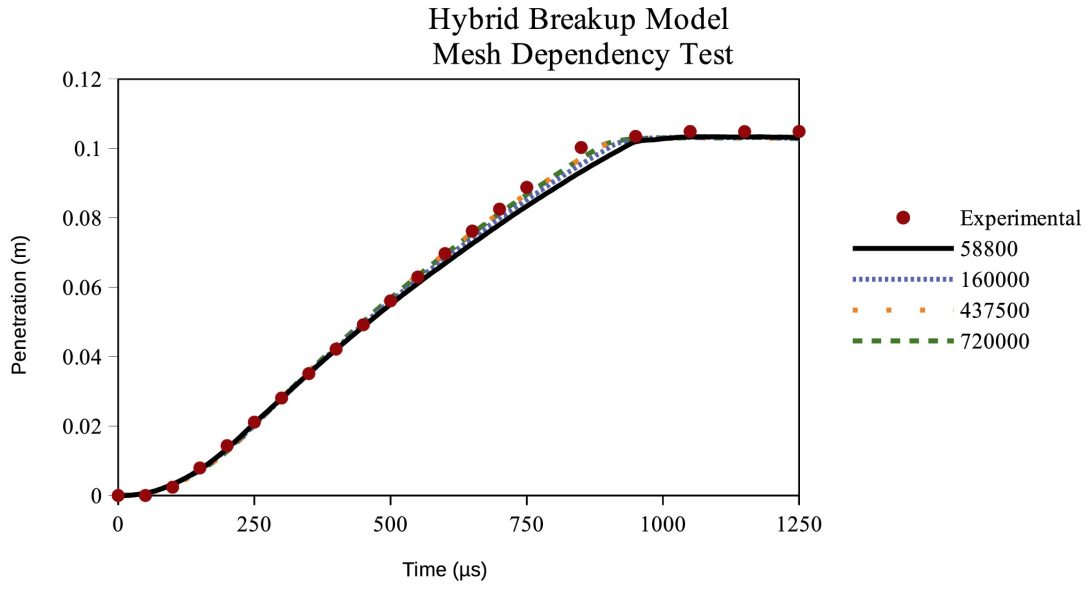


Figure 3.10.: Mesh dependency test at  $T_{\text{fuel}}=293\text{K}$ ,  $P_v=1\text{bar}$

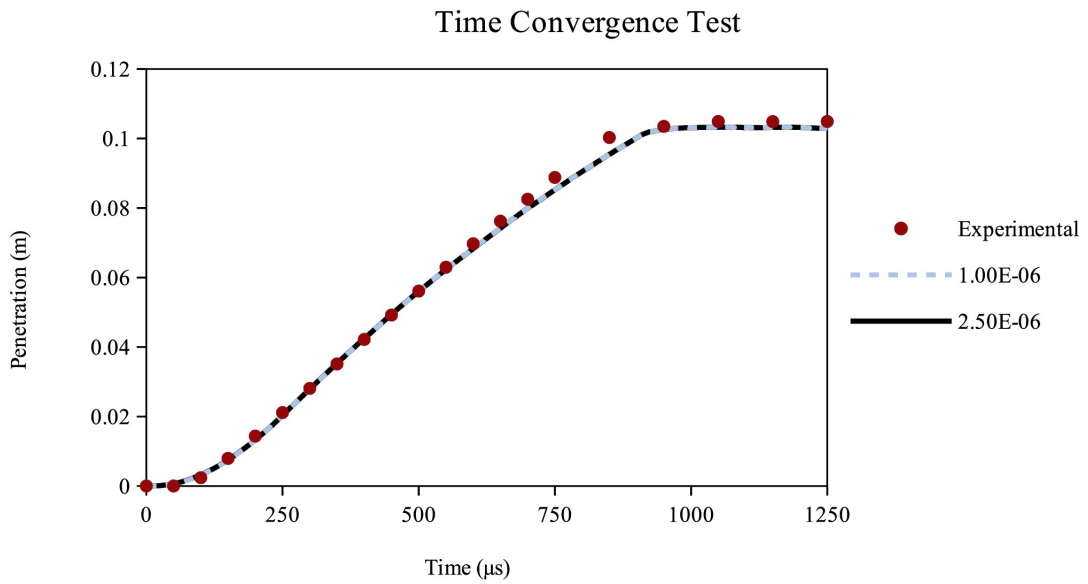


Figure 3.11.: Time convergence test at  $T_{\text{fuel}}=293\text{K}$ ,  $P_v=1\text{bar}$

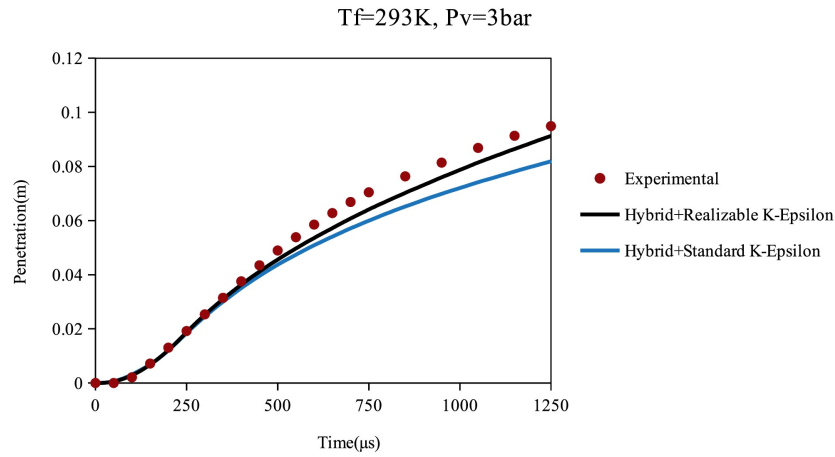
## CHAPTER 4

### RESULTS AND DISCUSSIONS

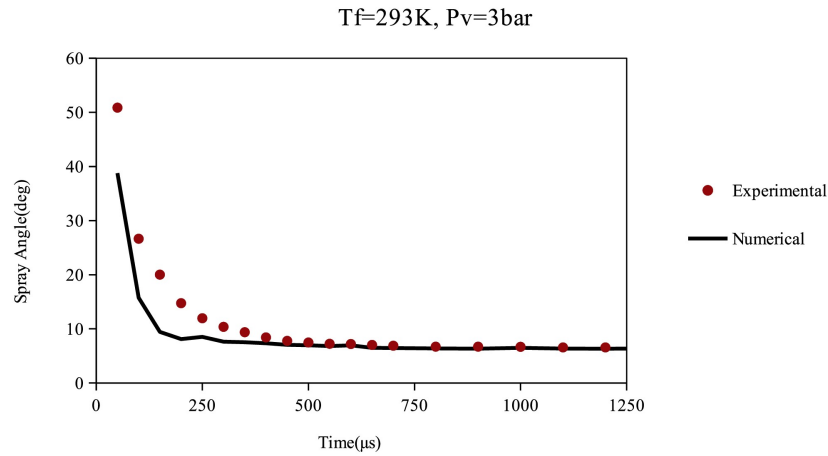
The main goal of this study is to build a numerical model for the estimation of non-flashing and flashing spray structures in terms of spray penetration length and spray angle. The operating conditions were mentioned in Table (3.4) and the results are given between Figure (4.1)- Figure(4.9) in this section.

Experimental measurements of spray structures under these circumstances were completed by a high-speed camera synchronized with the injector actuation. Thereafter, single frames were extracted from high-speed videos and they were processed in order to calculate spray penetration length and spray angle<sup>[23]</sup>. Numerical measurements of spray penetration length were provided by OpenFOAM after the simulations were over, yet the spray angle data was found by an inhouse code developed for the calculation of spray angle. Since those parameters are directly influenced by the mass fraction of the spray, the mass fraction of the spray was assumed as 95% to lessen the fluctuation in data<sup>[68]</sup>.

In Section (3.6) the numerical spray penetration values for realizable  $k-\varepsilon$  turbulence model and the standard  $k-\varepsilon$  turbulence model were compared at  $T_{fuel}=293$  K and  $P_v= 1$  bar. Figure (4.1a) indicates the results for sprays modeled with those turbulence models and it can be clearly seen that the one modeled with realizable  $k-\varepsilon$  has a better estimation for the non-flashing spray at  $T_{fuel}=293$  K and  $P_v= 3$  bar. Since non-flash-boiling sprays have longer penetration lengths, they hit the walls of geometry. Therefore, realizable  $k-\varepsilon$  turbulence model gives closer results to the experimental ones for those sprays and the comparison between numerical and experimental data for non-flashing sprays is completed considering that. Additionally, the numerical spray tip penetration length is roughly 0.007 m lower than the experimental one after 500  $\mu s$ . Both experimental and numerical penetration lines have values less than the end point of the geometry because of the back pressure. Besides spray penetration length analysis, numerical spray cone angle values are also compared with the experimental ones. Figure (4.1b) shows that there is a good match after 350  $\mu s$  but the numerical results are almost 10 degrees smaller than the experimental values before that point. Difficulties of numerical and experimental spray angle measurements just after the SOI may cause that difference between them.



(a) Spray Penetration Length at  $T_{\text{fuel}}=293\text{K}$   $P_v=3\text{bar}$

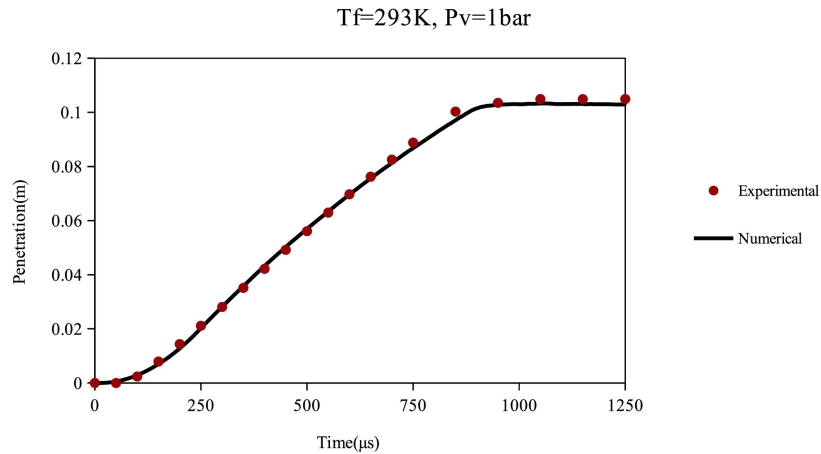


(b) Spray cone angle at  $T_{\text{fuel}}=293\text{K}$   $P_v=3\text{bar}$

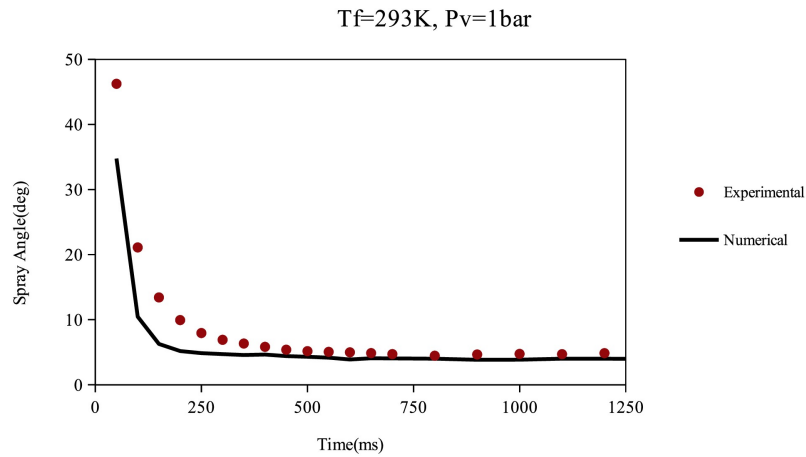
Figure 4.1.: Spray penetration and cone angle at  $T_{\text{fuel}}=293\text{K}$   $P_v=3\text{bar}$

The same analyses for the non-flashing spray at  $T_{\text{fuel}}=293\text{K}$  and  $P_v=1\text{bar}$  are illustrated in Figure (4.2). Under those circumstances, the numerical spray penetration shows a very good match with the experimental penetration line. However, there are small gaps between these values in the range of  $750\ \mu\text{s}$ - $900\ \mu\text{s}$  and  $900\ \mu\text{s}$ - $1250\ \mu\text{s}$ . The differences range from  $0.002\ \text{m}$  to  $0.005\ \text{m}$  between the mentioned time steps. The reason for having shorter penetration length in the numerical spray after  $900\ \mu\text{s}$  might be the particles that are pushed back after the spray hits the wall of the geometry. In addition to the penetration length, the trend of the numerical spray angle looks fine but the values are smaller than the experimental results. Moreover, spray angle value decreases sharply at the beginning

and then, it starts to become nearly a constant line two time steps after the sudden drop.



(a) Spray Penetration Length at  $T_{fuel}=293K$   $P_v=1bar$

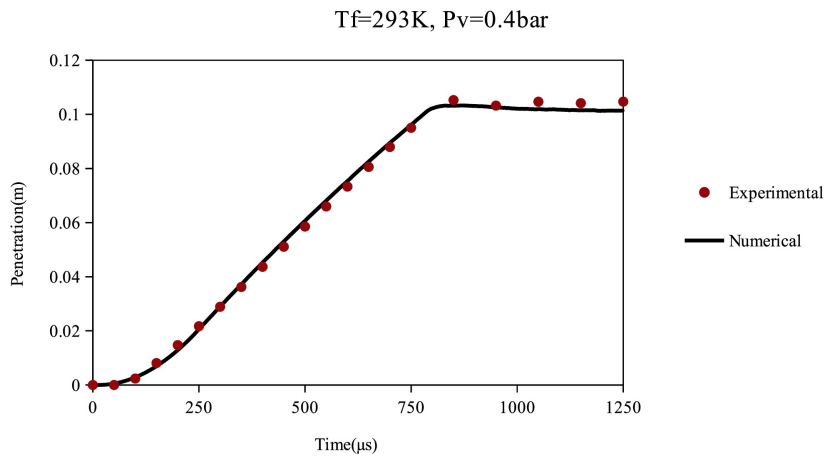


(b) Spray cone angle at  $T_{fuel}=293K$   $P_v=1bar$

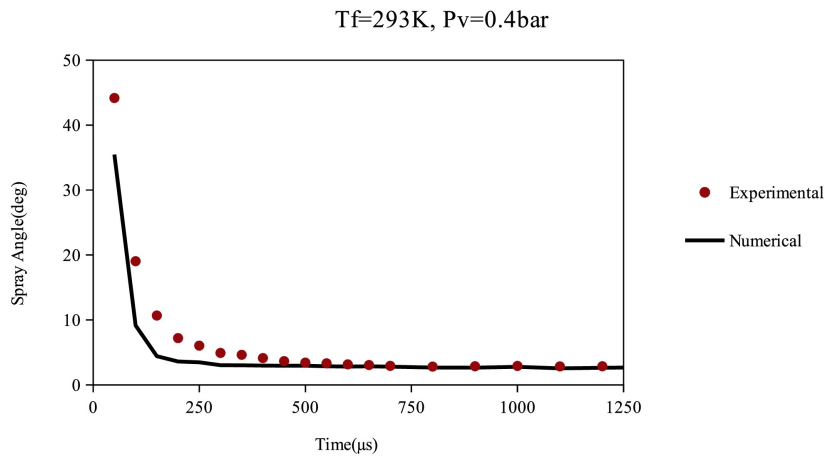
Figure 4.2.: Spray penetration and cone angle at  $T_{fuel}=293K$   $P_v=1bar$

Figure (4.3) indicates the comparison of experimental and numerical values at  $T_{fuel}=293K$  and  $P_v=0.4bar$ . The results of spray penetration length seem almost the same. However, the numerical data is slightly above the experimental values until  $1000\mu s$ . After this time step, the numerical values are a little lower than the experimental one like the numerical spray penetration length at  $T_{fuel}=293K$  and  $P_v=1bar$ . Furthermore, the numerical spray cone angle has a good trend and it matches with the experimental values after  $500\mu s$ . On the other hand, the experimental spray angle data is almost 10 degrees bigger than the numerical results until  $250\mu s$  and both experimental and numerical values decrease

harshly between first and second time steps.



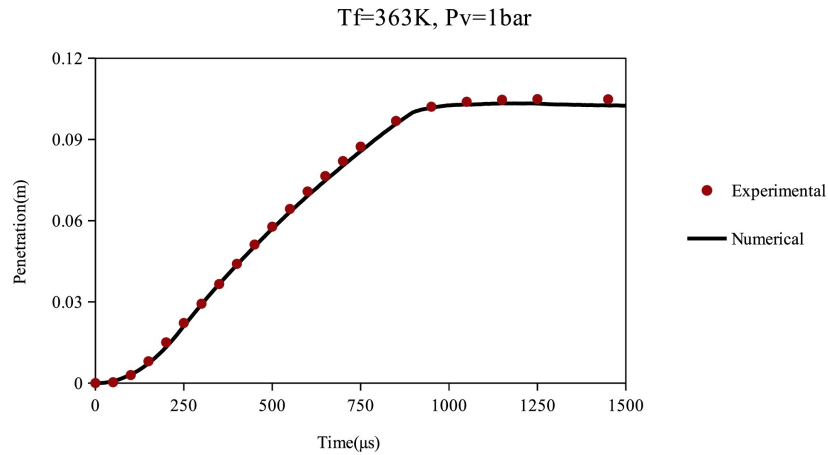
(a) Spray Penetration Length at  $T_{\text{fuel}}=293\text{K}$   $P_v=0.4\text{bar}$



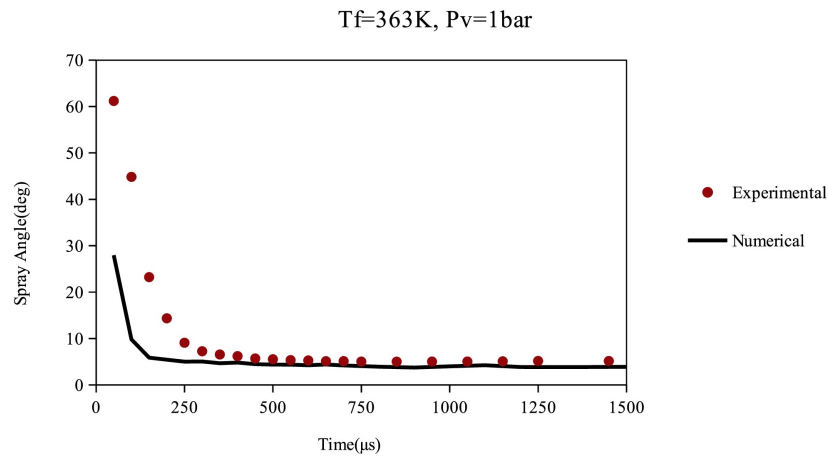
(b) Spray cone angle at  $T_{\text{fuel}}=293\text{K}$   $P_v=0.4\text{bar}$

Figure 4.3.: Spray penetration and cone angle at  $T_{\text{fuel}}=293\text{K}$   $P_v=0.4\text{bar}$

In Figure (4.4), the same comparisons are described for  $T_{\text{fuel}}=363\text{K}$  and  $P_v=1\text{bar}$ . The spray tip penetration has a perfect match under those conditions. On the contrary, there is a large difference between numerical and experimental spray angle values in the range of  $50\ \mu\text{s}$  and  $200\ \mu\text{s}$ . Especially, it is almost 30 degrees for the first and second time steps. However, the values are close to each other after  $200\ \mu\text{s}$ .



(a) Spray Penetration Length at  $T_{fuel}=363K$   $P_v=1bar$



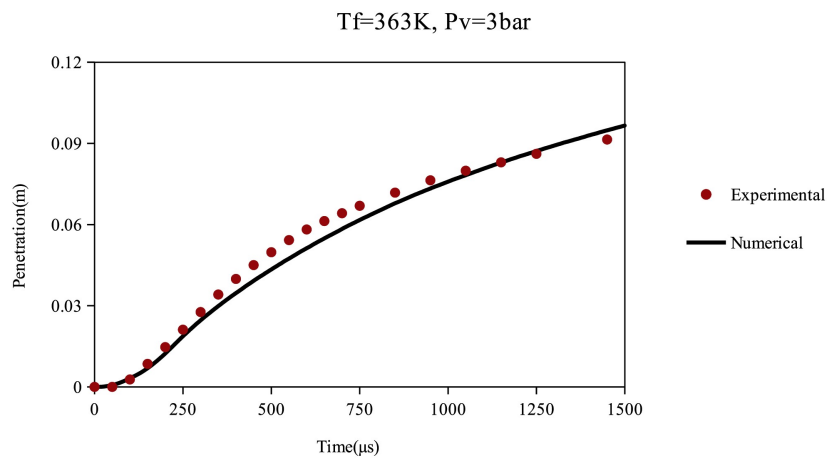
(b) Spray cone angle at  $T_{fuel}=363K$   $P_v=1bar$

Figure 4.4.: Spray penetration and cone angle at  $T_{fuel}=363K$   $P_v=1bar$

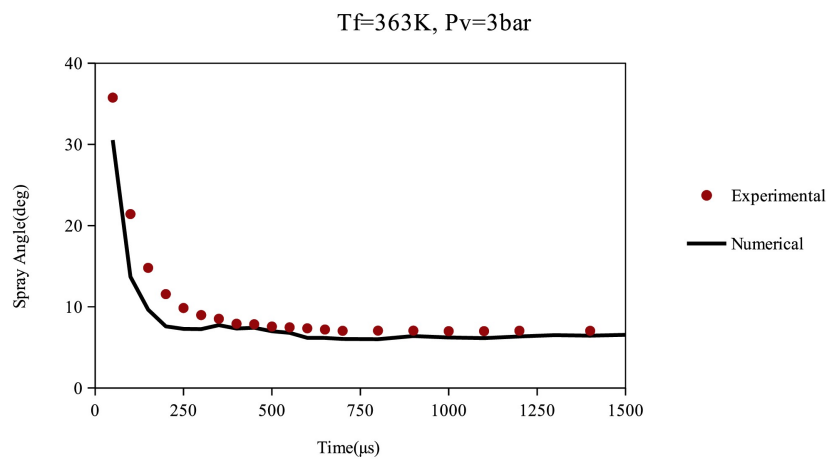
Figure (4.5) depicts the spray angle and spray penetration length at  $T_{fuel}=363K$  and  $P_v=3bar$ . The numerical penetration line does not have the same slope with the experimental one but the values of them are close to each other. The highest difference between them is nearly 0.01 m. The numerical penetration line intersects the experimental line at 1200  $\mu s$  and after that point, the numerical values become slimly bigger than the experimental results. Additionally, experimental and numerical results at the last time step are lower than the end point of the geometry because of the back pressure and higher fuel temperature. On the other hand, the spray cone angle shows a good trend. Even if the results look close to each other, the experimental results are 1 degree greater than the nu-



merical ones after 300  $\mu s$ . Before that point, there is almost 5 degrees difference between the two lines.



(a) Spray Penetration Length at  $T_{fuel}=363K$   $P_v=3bar$

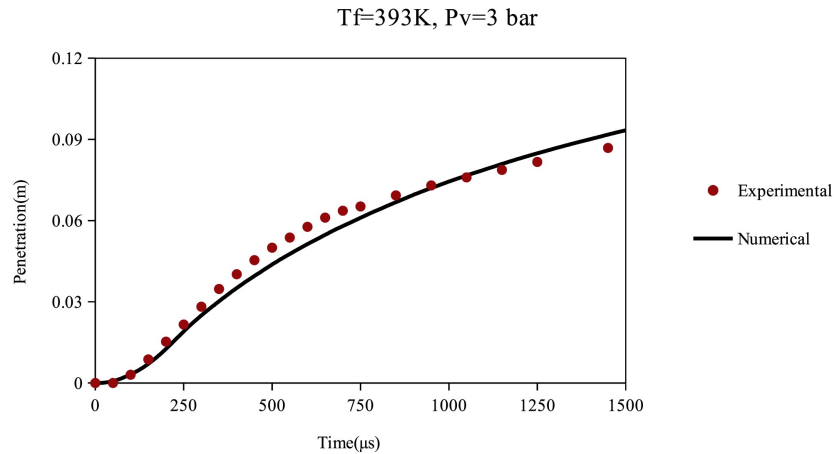


(b) Spray cone angle at  $T_{fuel}=363K$   $P_v=3bar$

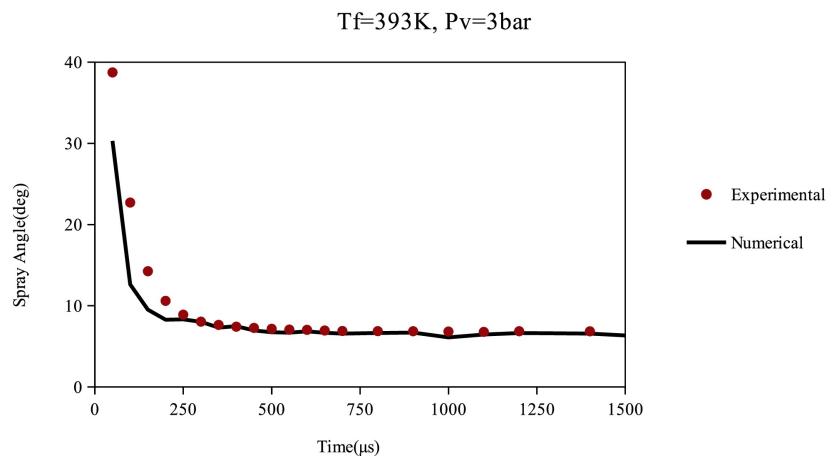
Figure 4.5.: Spray penetration and cone angle at  $T_{fuel}=363K$   $P_v=3bar$

The last analyses of non-flash-boiling sprays are illustrated in Figure (4.6) for the sprays at  $T_{fuel}=393K$  and  $P_v=3bar$ . The spray penetration line has a dissimilar trend like the numerical spray penetration line at  $T_{fuel}=363K$  and  $P_v=3bar$ . Both numerical and experimental penetration lines have the end points that are less than the length of the geometry. The experimental results are higher than the numerical values in the range of 250  $\mu s$  and 1000  $\mu s$ . 1000  $\mu s$  is the intersection point of those lines and the numerical results are a little bigger than the experimental merits after that point. Besides spray

tip penetration, spray angle values are also close to each other and they show a perfect match after 200  $\mu\text{s}$ . Before this time step, there is roughly 8 degrees difference between numerical and experimental points. Among whole spray angle analysis, this one looks the best because many numerical results match with the experimental measurements.



(a) Spray Penetration Length at  $T_{\text{fuel}}=393\text{K}$   $P_v=3\text{bar}$

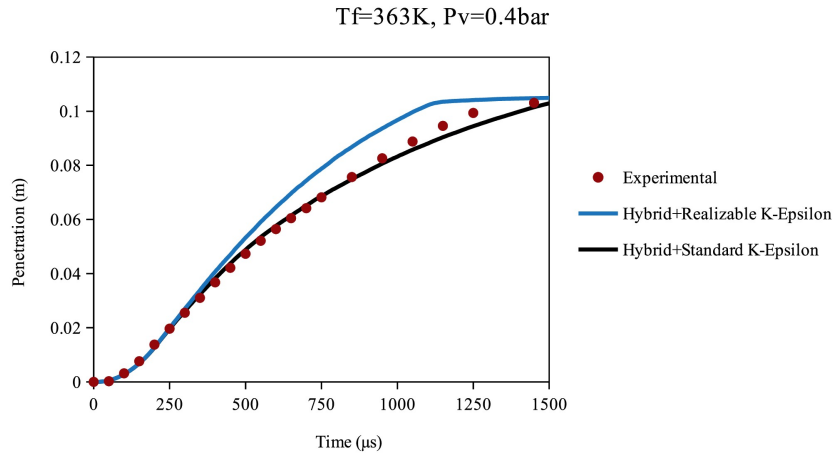


(b) Spray cone angle at  $T_{\text{fuel}}=393\text{K}$   $P_v=3\text{bar}$

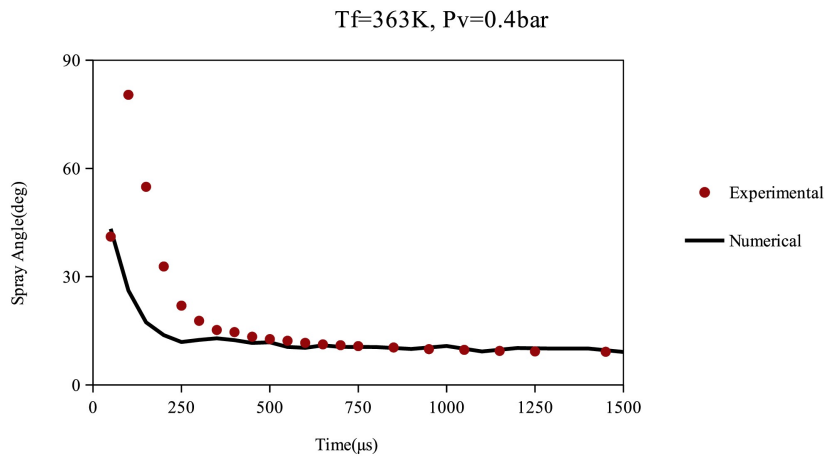
Figure 4.6.: Spray penetration and cone angle at  $T_{\text{fuel}}=393\text{K}$   $P_v=3\text{bar}$

Except for non-flashing sprays, the sprays under flash-boiling conditions were also simulated with the same models. However, the results demonstrate that realizable  $k-\varepsilon$  turbulence model is not the appropriate model to predict flashing sprays since the flashing spray reaches the maximum point of the geometry when realizable  $k-\varepsilon$  turbulence model is applied. On the contrary, the flashing sprays normally have wider angles and shorter

penetration lengths in theory. Therefore, the standard  $k-\varepsilon$  turbulence model was chosen for the numerical investigations of the flash-boiling sprays. Figure (4.7) is the illustration of the numerical and experimental comparisons of sprays at  $T_{\text{fuel}}=363\text{K}$  and  $P_v=0.4\text{bar}$ .



(a) Spray Penetration Length at  $T_{\text{fuel}}=363\text{K}$   $P_v=0.4\text{bar}$



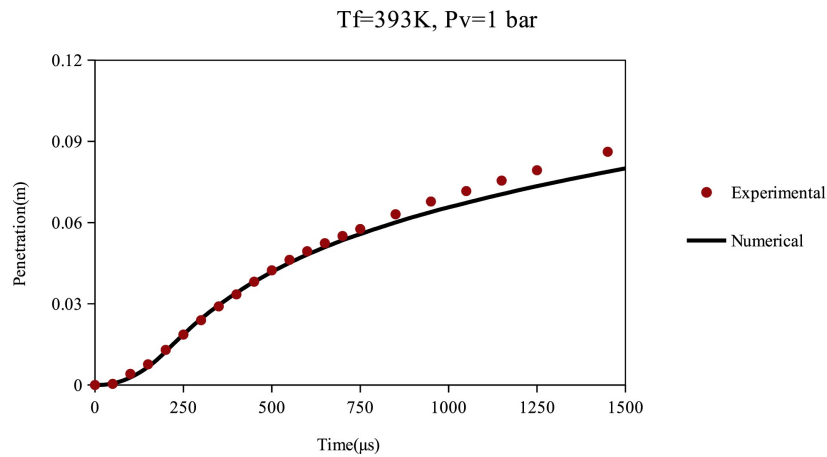
(b) Spray cone angle at  $T_{\text{fuel}}=363\text{K}$   $P_v=0.4\text{bar}$

Figure 4.7.: Spray penetration and cone angle at  $T_{\text{fuel}}=363\text{K}$   $P_v=0.4\text{bar}$

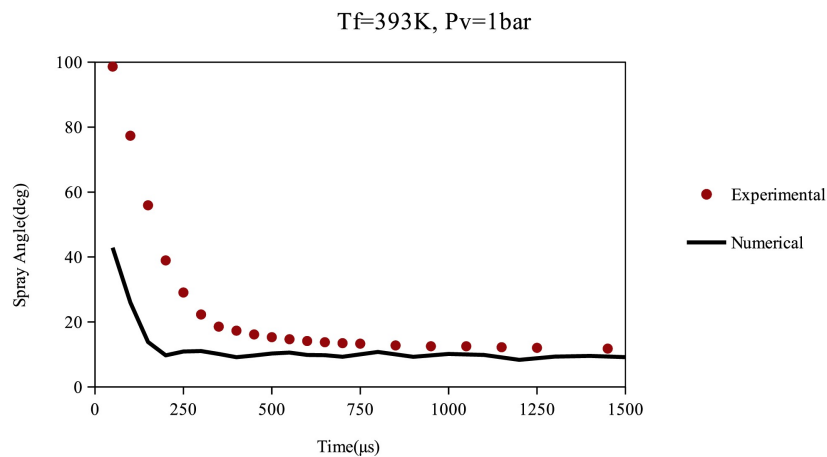
The penetration length estimated by the numerical model with realizable  $k-\varepsilon$  turbulence submodel seems like a non-flashing spray. Nevertheless, the estimation of the model with standard  $k-\varepsilon$  turbulence submodel looks very good. For this model, there is a small gap between the experimental and the numerical lines after  $1000 \mu\text{s}$  and the maximum difference is almost 5 mm. Both curves meet again at the end. The predictions of the spray cone angle are also fine for the first time step and the time steps after  $300 \mu\text{s}$ .

However, there is an enormous difference at the second time step due to the surprising rise of experimental spray angle. Normally, the spray angle is the highest at the first time step because of its shape just after the SOI. Then, the spray angle starts decreasing after the spray has a triangular structure. Additionally, the experimental penetration length is not influenced by this sudden increase and it continues to go up at the second time step.

The investigations of another flashing spray at  $T_{\text{fuel}}=393\text{K}$  and  $P_v=1\text{bar}$  are indicated in Figure (4.8).



(a) Spray Penetration Length at  $T_{\text{fuel}}=393\text{K}$   $P_v=1\text{bar}$



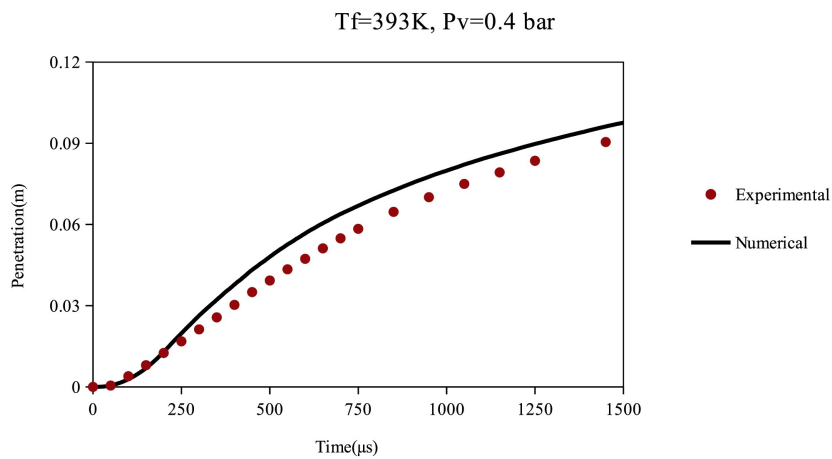
(b) Spray cone angle at  $T_{\text{fuel}}=393\text{K}$   $P_v=1\text{bar}$

Figure 4.8.: Spray penetration and cone angle at  $T_{\text{fuel}}=393\text{K}$   $P_v=1\text{bar}$

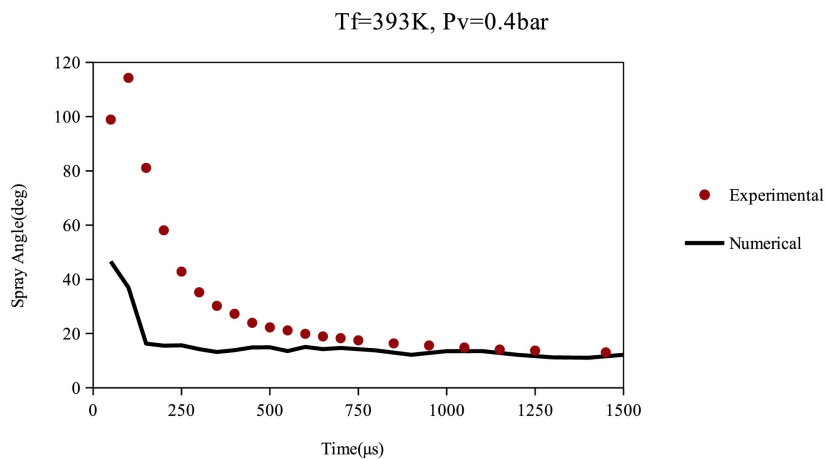
The numerical spray penetration curve has a good trend and it matches with the experi-

mental curve until  $750 \mu\text{s}$ . After that point, numerical results are lower than the experimental data and the difference between them is almost  $0.01 \text{ m}$  at the end. On the contrary, the numerical spray cone angle data does not have a good match with the experimental results. Especially, the experimental angle is much greater than the numerical one at the first time step. This gap is continuous until  $750 \mu\text{s}$  but the lines get closer to each other after that point and there are approximately 4 degrees between those lines.

Figure (4.9) shows the results for the last flash-boiling analysis for the sprays at  $T_{\text{fuel}}=393\text{K}$  and  $P_v=0.4\text{bar}$ .



(a) Spray Penetration Length at  $T_{\text{fuel}}=393\text{K}$   $P_v=0.4\text{bar}$



(b) Spray cone angle at  $T_{\text{fuel}}=393\text{K}$   $P_v=0.4\text{bar}$

Figure 4.9.: Spray penetration and cone angle at  $T_{\text{fuel}}=393\text{K}$   $P_v=0.4\text{bar}$

Both penetration curves have almost the same slope, yet the experimental values are nearly 0.01 mm lower than the numerical ones after 250  $\mu\text{s}$ . The spray angle investigations seem good after the first half of the simulations. In the first half of the comparisons, the experimental results are much higher than the numerical merits until 600  $\mu\text{s}$ . Unlike other spray angle curves, the experimental curve of fully flashing spray decreases gradually. However, it rises in the second time step and this does not affect the spray penetration length.

In addition to those investigations, the results are also compared with the study of Gulec et al.<sup>[49]</sup> in terms of spray penetration length. The discharge coefficient value was kept constant in their study. Different from that, modified spray injection profiles for dissimilar fuel temperatures, theoretically computed discharge coefficient  $C_d$  and spray initial angle (SIA) for different conditions, and realizable  $k-\varepsilon$  turbulence model are implemented in this study. Figure (4.10) illustrates that the model working with realizable  $k-\varepsilon$  turbulency and theoretically evaluated parameters predicts the non-flashing sprays better.

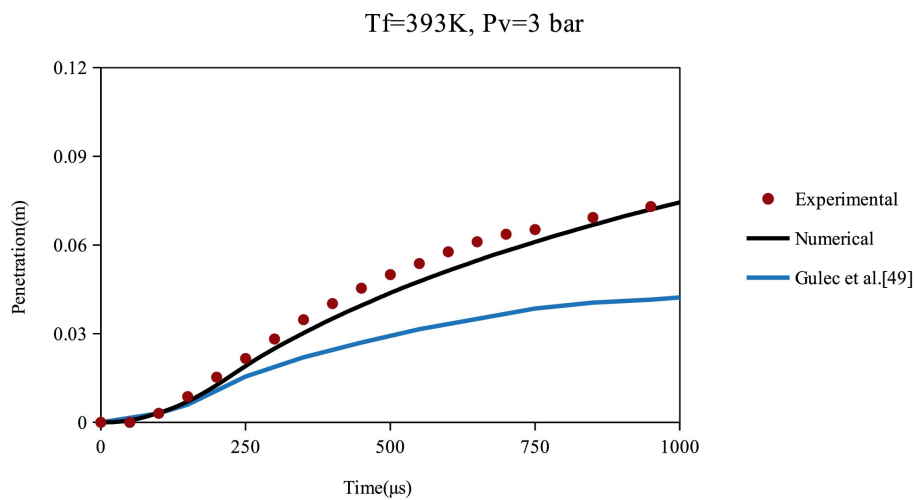


Figure 4.10.: Comparison of two numerical models at  $T_{\text{fuel}}=393\text{K}$ ,  $P_v=3\text{bar}$

Besides non-flashing ones, the comparisons for flash-boiling sprays are shown between Figure (4.11)-Figure (4.13). The main difference between the models of flash-boiling sprays is theoretically evaluated parameters. Therefore, the effects of those calculations are compared. Figure (4.11) indicates the results for sprays at  $T_{\text{fuel}}=363\text{K}$  and

$P_v=0.4\text{bar}$ .  $C_d$  value used in this thesis looks suitable for the simulations under those circumstances. Normally, lower discharge coefficients affect the spray penetration length reversely. Hence, the numerical model of Gulec et al.<sup>[49]</sup> has slightly bigger results than experimental ones between  $250\ \mu\text{s}$  and  $1000\ \mu\text{s}$ .

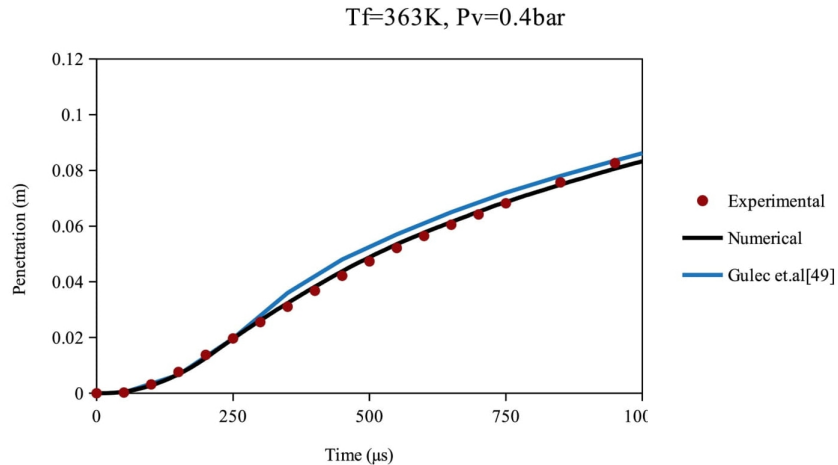


Figure 4.11.: Comparison of two numerical models at  $T_{\text{fuel}}=363\text{K}$ ,  $P_v=0.4\text{bar}$

Another comparison is depicted in Figure (4.12) for the flashing sprays at  $T_{\text{fuel}}=393\text{K}$  and  $P_v=1\text{bar}$ . The results of both models look fine until  $600\ \mu\text{s}$  but the model of Gulec et al.<sup>[49]</sup> becomes constant after  $600\ \mu\text{s}$  while experimental values are going up. At the last time step, there is almost 15 mm difference between them. On the other hand, the model used in this study estimated the sprays good enough. In this comparison, the effect of the discharge coefficient is different from the previous investigation for the sprays at  $T_{\text{fuel}}=363\text{K}$  and  $P_v=0.4\text{bar}$ . Additionally, the spray initial angle of the model of Gulec et al.<sup>[49]</sup> is not known either and that might have a significant influence on the results.

The last comparison is done for fully flashing sprays at  $T_{\text{fuel}}=393\text{K}$  and  $P_v=0.4\text{bar}$ . The curves of both models follow the same path until  $600\ \mu\text{s}$  and they are almost 8 mm above the experimental curve. However, the numerical line of Gulec et al.<sup>[49]</sup> bends at  $750\ \mu\text{s}$  and matches with the experimental data while the other numerical line has the same trend. They are both less than the length of geometry, so they fulfill the requirements of flash-boiling phenomena but the model of Gulec et al.<sup>[49]</sup> has better results than the numerical model of this study for full flash-boiling sprays.

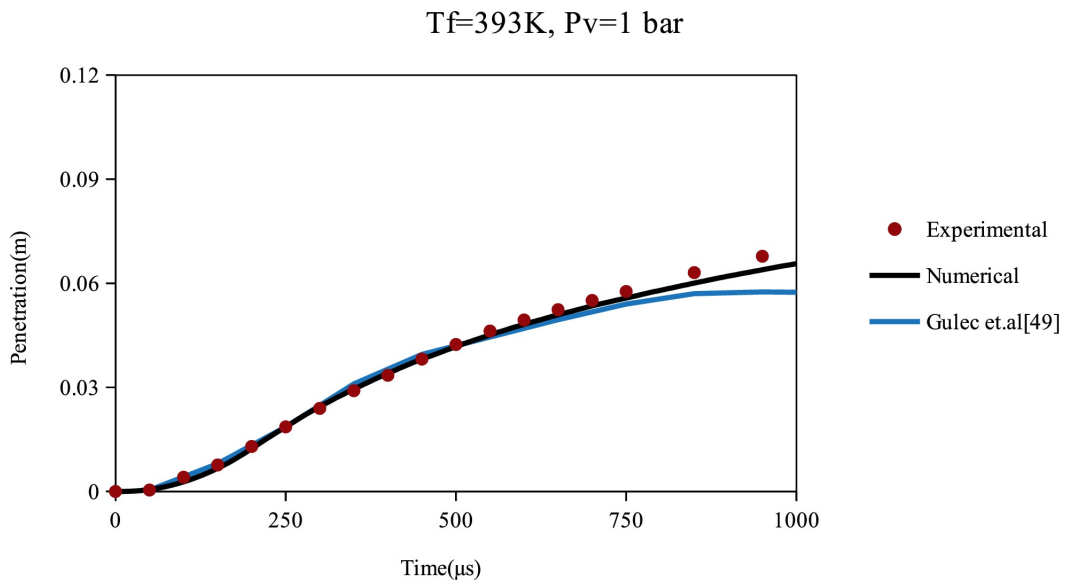


Figure 4.12.: Comparison of two numerical models at  $T_{\text{fuel}}=393\text{K}$ ,  $P_v=1\text{bar}$

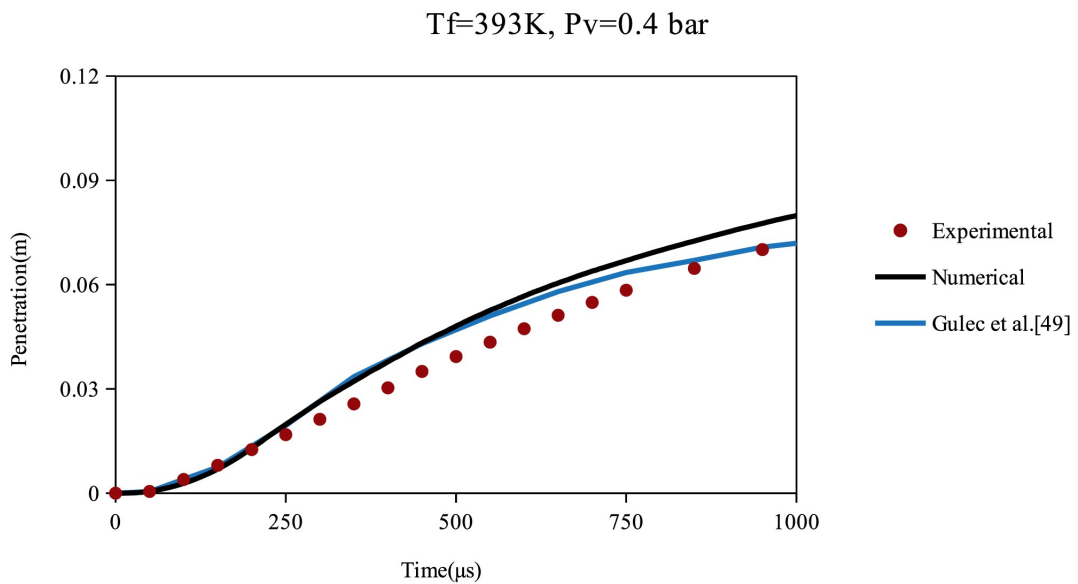


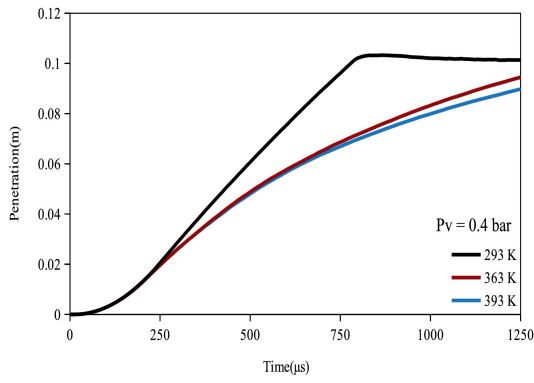
Figure 4.13.: Comparison of two numerical models at  $T_{\text{fuel}}=393\text{K}$ ,  $P_v=0.4\text{bar}$



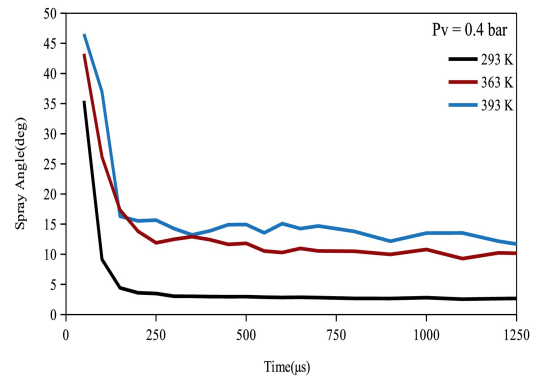
Besides the previous comparisons, the numerical spray penetration length and spray cone angle results are also compared for constant vessel pressure and variable fuel temperature values as well as dissimilar vessel pressures and constant fuel temperature. While the diagrams in Figure (4.14) represents the numerical results in terms of spray penetration length and spray cone angle for constant chamber pressure and various fuel temperature values, Figure (4.15) indicates the numerical results for constant fuel temperature and variable vessel pressures.

In Figure (4.14), the graphs of spray penetration length illustrate that the evaporation is promoted when the fuel temperature rises. Therefore, the penetration length is the shortest for the sprays at 393K. The penetration lengths are close to each other under back pressure condition. On the other hand, the sprays at 293K and 363K show approximately the same trend under atmospheric pressure while the sprays at 363K and 393K follow similar curves under vacuum pressure. In addition to the spray penetration length diagrams, the spray cone angle ones indicate that the sprays in transient and flashing regions have much wider angles than the sprays in non-flash-boiling region. Besides that, sprays under back pressure condition have almost the same spray cone angle values whilst the spray cone angles at 293K and 363K have very close results to each other under atmospheric pressure. Furthermore, the fully flashing spray has the widest angle among all.

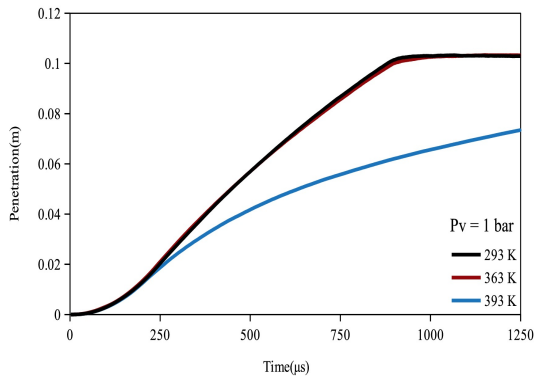
The comparison of numerical spray penetration length and cone angle results under constant fuel temperature and variable vessel pressure values are demonstrated in Figure (4.15). The sprays at room temperature prove the common relation between spray penetration length and spray cone angle since the spray having the shortest penetration length has the highest spray cone angle values. In addition to that, the spray cone angle values for the sprays at 363K have the expected results as the spray at  $T_f=363\text{K}$  and  $P_v=0.4\text{bar}$  is in the transient region. Therefore, it has the greatest spray cone angle. On the other hand, the penetration length for the spray at  $T_f=363\text{K}$  and  $P_v=0.4\text{bar}$  is unexpectedly longer than the length under back pressure. Moreover, the spray at the same temperature and atmospheric pressure has the penetration length looking like the penetration length of the spray at  $T_f=293\text{K}$  and  $P_v=1\text{bar}$ . Lastly, the fully flashing spray has the highest spray angle when it is compared with the other sprays at 393K fuel temperature. However, the spray penetration length at this fuel temperature is unexpectedly the longest one. Normally, it is expected to be the shortest one due to the relation between spray cone angle and penetration length. Additionally, the penetration length in the transient region is lower than the one in the non-flashing region because of the flash evaporation.



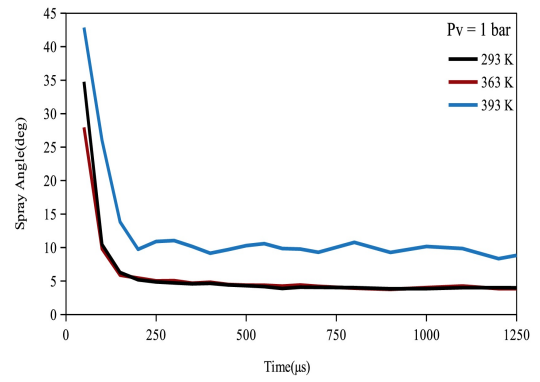
(a)



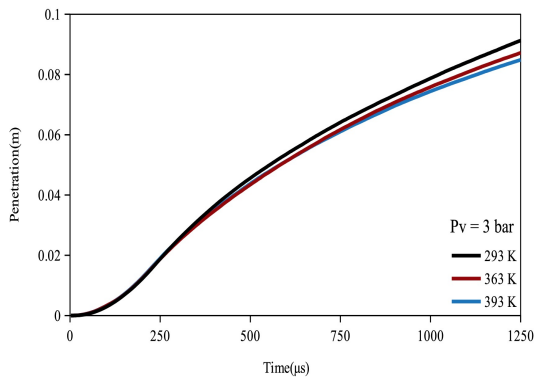
(b)



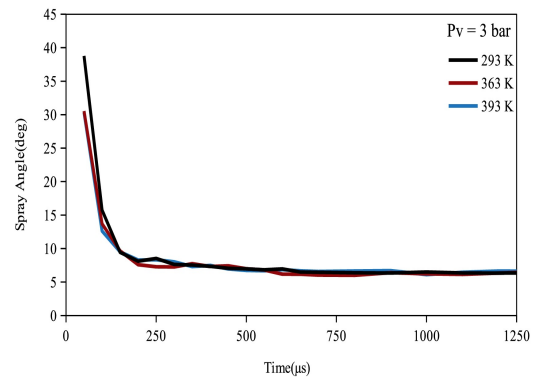
(c)



(d)

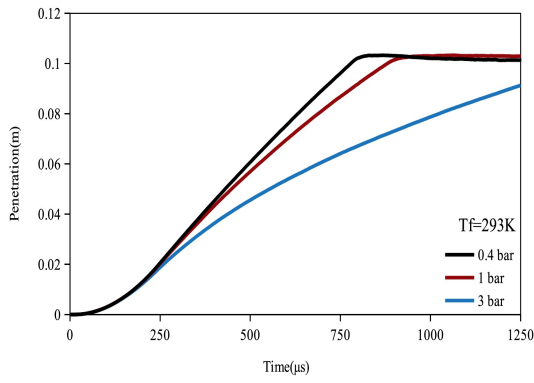


(e)

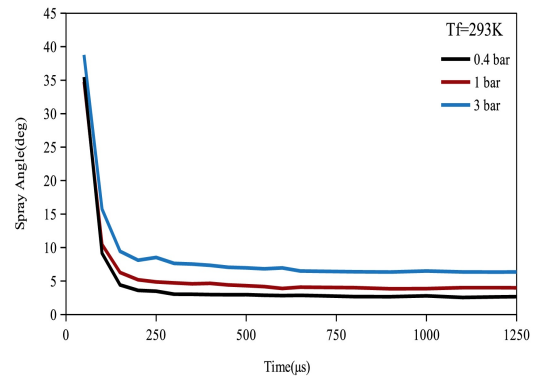


(f)

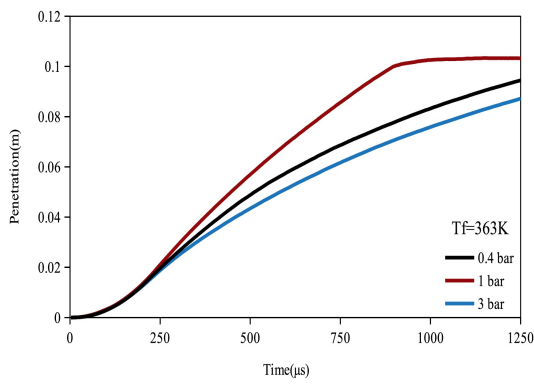
Figure 4.14.: Comparison of numerical data for constant  $P_v$  and variable  $T_f$



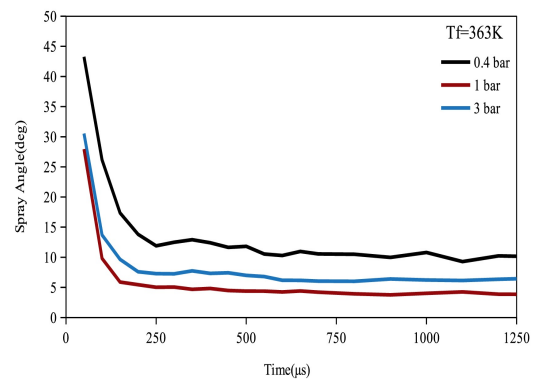
(a)



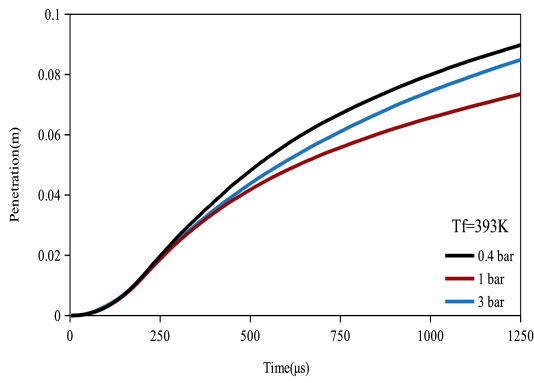
(b)



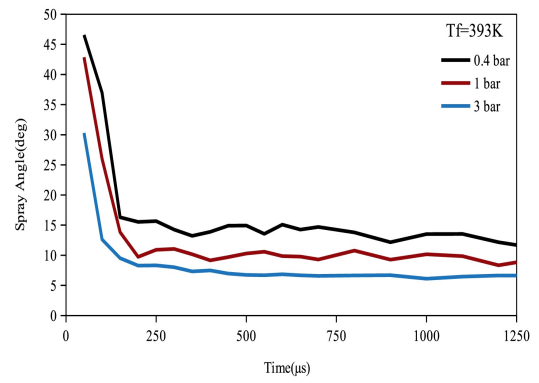
(c)



(d)



(e)



(f)

Figure 4.15.: Comparison of numerical data for constant  $T_f$  and variable  $P_v$

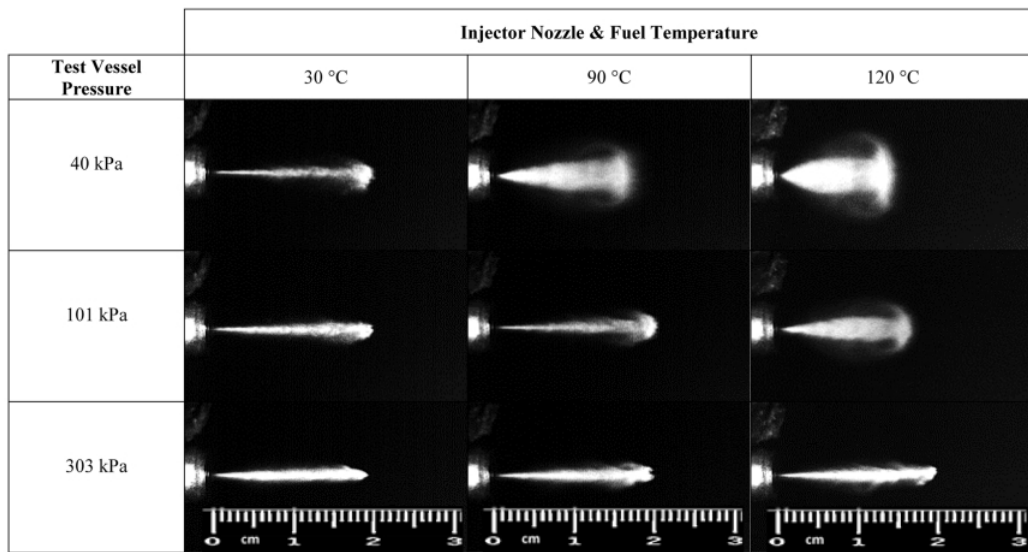


Figure 4.16.: Experimental particle distribution (Source: Postrioti et al. [23])

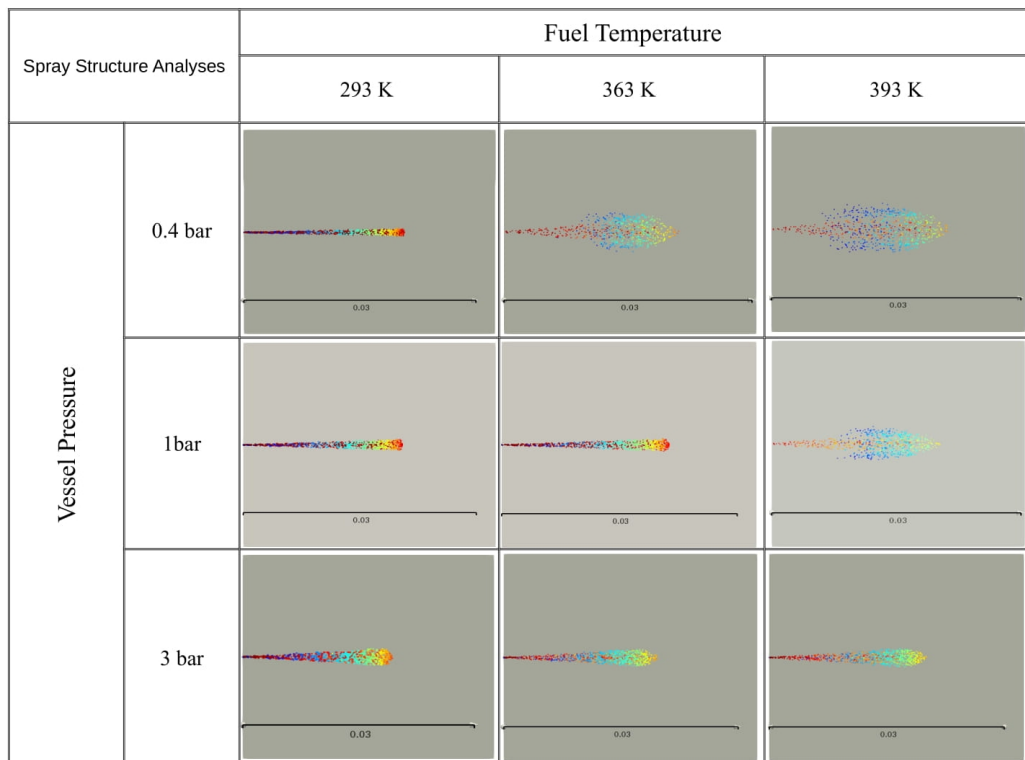


Figure 4.17.: Numerical particle distribution

In addition to spray penetration length and spray cone angle analyses, spray structures are also investigated for the sprays under different conditions. Figure (4.16) and Figure (4.17) shows the experimental and numerical results of them. In this study, non-flashing sprays for 20 °C is examined instead of the non-flashing sprays at 30 °C. The images indicate that the dissimilarity between those is not that much. All non-flashing sprays seem like the experimental ones and the numerical flashing sprays has also wide spray cone angle values like experimental sprays but they do not look as wide as the experimental ones after the liquid fuel leaves the nozzle tip. This might result in the divergence between numerical and experimental spray cone angle values.

Furthermore, the spray angle curves are also investigated statistically and the average standard deviation values shown in Table (4.1) are computed for understanding the average difference between numerical and experimental cone angle curves. Based on the results, the cone angle data of non-flashing sprays mostly matches with the experimental results. However, the cone angle values for the sprays in transient and full flash-boiling regions differ from the experimental results. Big differences of spray angle values after the SOI lead to the high standard deviation number for those sprays.

Table 4.1.: Average standard deviation of spray angle analyses

<b>Average Standard Deviation for Spray Cone Angle</b>			
<b>Temperature (K)</b>	<b>Pressure (kPa)</b>		
	<b>40</b>	<b>100</b>	<b>300</b>
<b>293</b>	1.39	1.84	1.90
<b>363</b>	4.62	3.84	1.23
<b>393</b>	8.83	11.91	0.99

# CHAPTER 5

## CONCLUSIONS

The numerical investigations of non-flash-boiling and flash-boiling sprays generated by a single-hole GDI research injector IHP-293 were completed in this thesis. An open source CFD software namely OpenFOAM was used for performing the simulations and MATLAB was utilized as the post-processing tool for spray angle analyses. The numerical results were validated against the experimental data in terms of spray penetration length and spray cone angle. All results proved that spray penetration length and spray cone angle are inversely proportional.

A typical cylindrical geometry that has been used in different studies was composed and dissimilar mesh sizes were tested for obtaining the best results. The sub-models were detected based on the literature survey and some modifications were done in the source code. Besides those changes, the significant parameters discharge coefficient  $C_d$  and spray initial angle were theoretically calculated for each case. However, theoretical spray initial angle values were too low for flashing sprays, so they were determined with respect to the experimental measurements. In addition to these parameters, the secondary breakup and turbulence models made a difference as well. Hybrid and Pilch-Erdman secondary breakup models had almost the same results but the Hybrid model predicted the sprays better than Pilch-Erdman with a very tiny difference. As a turbulence model, the standard and realizable  $k-\varepsilon$  models were compared. The simulations completed with realizable  $k-\varepsilon$  model had preferable results for non-flashing sprays since those sprays were either very close to the wall of the geometry or hit that wall. On the other hand, it did not work well for flashing sprays due to shorter penetration lengths of them. Hence, the standard  $k-\varepsilon$  model was applied for the simulations of flashing sprays and it provided good results in terms of penetration length.

Moreover, the spray cone angles were estimated adequately for non-flashing sprays but the predictions for flashing sprays were in acceptable range. The numerical spray structures of flashing sprays were not as wide as the experimental ones. This results in a standard deviation of 5 to 12% between spray cone angle values for the sprays in the transient and flashing regions. After the start of injection, the spray cone angle value

could not be computed well for non-flashing cases either. The miscalculations were done mostly in the first four time steps and the results were either very close to the experimental ones or matched with them after those time steps. Since both numerical and experimental measurements of spray angle are difficult just after the start of injection, that variance might have emerged.

The spray penetration lengths were also compared with the study of Gulec et al.<sup>[49]</sup>, which was completed with the Hybrid secondary breakup model. The results indicated that the numerical model was improved because the changes done helped to have better estimations for both non-flashing and flashing sprays. However, the numerical data of the previous model for fully flashing spray was one step closer to the experimental merits.

Also, the comparisons of numerical results showed that a rise in the fuel temperature enhanced the evaporation rate. Besides that, the sprays in transient and fully flashing regions had the widest spray cone angles. The spray penetration length was also affected by the back pressure. Additionally, the relation between spray penetration length and cone angle was proved once and it was seen that the penetration length decreased when the cone angle increased.

In order to improve the predictions of both non-flashing and flashing fuel sprays, the suggestions that can be studied as future works are listed as follows:

- As it is hard to detect the behavior of flashing sprays at the primary breakup stage, a new flash atomization model can be developed for better estimations of flashing sprays after the start of injection.
- To compensate for the errors after SOI and have better estimations, LES or DNS simulations, which are more effective than RANS, can be applied. Particularly, they can give preferable results for the primary breakup of the sprays. However, they need much computing power, which should be taken into account.
- Based on the current spray angle algorithm, a new spray angle code can be developed with some modifications for better results in the beginning and it can be added into OpenFOAM source code. Also, the current spray angle code can be calibrated to obtain better predictions at the time steps when miscalculations occurred.

## REFERENCES

- [1] Postriotti, L.; Bosi, M.; Gioia, R. D.; Bonandrini, G. GDI spray evolution and sizing characteristics in Flash-Boiling conditions. **2015**, 10.
- [2] Cengel, Y. A.; Boles, M. A. *Thermodynamics: an engineering approach*, eighth edition ed.; McGraw-Hill Education: New York, 2015; OCLC: ocn869741544.
- [3] Baumgarten, C. *Mixture formation in internal combustion engines*; Heat and mass transfer; Springer: Berlin ; New York, 2006.
- [4] Huang, C. *Numerical modelling of fuel injection and stratified turbulent combustion in a direct-injection spark-ignition engine using an open source code*; Doktorsavhandlingar vid Chalmers Tekniska Hogskola N.S., 3775; Chalmers Univ. of Technology: Goteborg, 2014; OCLC: 931794918.
- [5] Celik, M. B.; Ozdalyan, B. In *Fuel Injection*; Siano, D., Ed.; ISBN:-307-116-9, InTech, Available from: injection/gasoline-direct-injection, 2010; pp 978–953.
- [6] What's The Difference Between Turbochargers and Superchargers?  
<https://www.boldmethod.com/learn-to-fly/systems/whats-the-difference-turbocharger-vs-supercharger>, (Accessed Nov 29, 2018).
- [7] Chincholkar, S.; Suryawanshi, J. Gasoline Direct Injection: An Efficient Technology. *Energy Procedia* **2016**, 90, 666–672.
- [8] Hiroyasu, H.; Arai, M. Structures of Fuel Sprays in Diesel Engines. SAE Technical Paper. 1990.
- [9] Chehroudi, B.; Chen, S.-H.; Bracco, F. V.; Onuma, Y. On the Intact Core of Full-Cone Sprays. SAE Technical Paper. 1985.
- [10] Ohnesorge, W. Die Bildung von Tropfen an Dusen und die Auflosung flussiger



- Strahlen. *Zeitschrift für angewandte Mathematik und Mechanik*, Bd. **1931**, 16, 355–358.
- [11] Wierzba, A. Deformation and Breakup of Liquid Drops in a Gas Stream at Nearly Critical Weber Numbers. *Experiments in Fluids* **1993**, 9, 59–64.
- [12] Ashgriz, N., Ed. *Handbook of atomization and sprays: theory and applications*; Springer: New York, NY, 2011; OCLC: 731927924.
- [13] Xi, X.; Liu, H.; Jia, M.; Xie, M.; Yin, H. A new flash boiling model for single droplet. *International Journal of Heat and Mass Transfer* **2017**, 107, 1129 – 1137.
- [14] Schmitz, I.; Ipp, W.; Leipertz, A. Flash Boiling Effects on the Development of Gasoline Direct-Injection Engine Sprays. SAE Technical Paper. 2002.
- [15] Senda, J. Modeling on atomization and vaporization process in flash boiling spray. *JSAE Review* **1994**, 15, 291–296.
- [16] Roesle, M. L.; Kulacki, F. A. Boiling of small droplets. *International Journal of Heat and Mass Transfer* **2010**, 53, 5587–5595.
- [17] Forster, H. K.; Zuber, N. Growth of a Vapor Bubble in a Superheated Liquid. *Journal of Applied Physics* **1954**, 25, 474–478.
- [18] Mohammadein, S. A.; Gouda, S. A. Temperature distribution in a mixture surrounding a growing vapour bubble. *Heat and Mass Transfer* **2006**, 42, 359–363.
- [19] Hanafizadeh, P.; Eshraghi, J.; Kosari, E.; Ahmed, W. H. The Effect of Gas Properties on Bubble Formation, Growth, and Detachment. *Particulate Science and Technology* **2015**, 33, 645–651.
- [20] Suma, S.; Koizumi, M. Internal Boiling Atomization by Rapid Pressure Reduction of Liquids. *Transactions of the Japan Society of Mechanical Engineers* **1977**, 43, 4608–4621.

- [21] Kawano, D.; Goto, Y.; Odaka, M.; Senda, J. Modeling Atomization and Vaporization Processes of Flash-Boiling Spray. SAE Technical Paper. 2004.
- [22] Xu, M.; Zhang, Y.; Zeng, W.; Zhang, G.; Zhang, M. Flash Boiling: Easy and Better Way to Generate Ideal Sprays than the High Injection Pressure. *SAE International Journal of Fuels and Lubricants* **2013**, *6*, 137–148.
- [23] Postrioti, L.; Bosi, M.; Cavicchi, A.; AbuZahra, F.; Gioia, R. D.; Bonandrini, G. Momentum Flux Measurement on Single-Hole GDI Injector under Flash-Boiling Condition. SAE Technical Paper. 2015.
- [24] Kusters, A.; Karlsson, A. A Comprehensive Numerical Study of Diesel Fuel Spray Formation with OpenFOAM. SAE Technical Paper. 2011.
- [25] Siebers, D. L. Liquid-Phase Fuel Penetration in Diesel Sprays. SAE Technical Paper. 1998.
- [26] Naber, J. D.; Siebers, D. L. Effects of Gas Density and Vaporization on Penetration and Dispersion of Diesel Sprays. SAE Technical Paper. 1996.
- [27] Kim, D.; Kim, K. Comparison of Spray Structures of Diesel and Gasoline Using Modified Evaporation Model in Openfoam CFD Package. SAE Technical Paper. 2014.
- [28] Abdelghaffar, W. A.; Karimi, K.; Heikal, M. R. Fuel Spray Penetration in High Pressure Diesel Engines. SAE Technical Paper. 2007.
- [29] Bianchi, G.; Pelloni, P. Modeling the Diesel Fuel Spray Breakup by Using a Hybrid Model. SAE Technical Paper. 1999.
- [30] Huh, K. Y.; Gosman, A. D. A Phenomenological Model of Diesel Spray Atomization. Proceedings of International Conference on Multiphase Flows. Japan, September, 1991; pp 24–27.
- [31] Allocca, L.; Belardini, P.; Bertoli, C.; Corcione, F.; De Angelis, F. Experimental

- and Numerical Analysis of a Diesel Spray, SAE Paper 920576. 1992.
- [32] A Chaudhry, I.; Mirza, M.; Rashid, M. Simulation of Non Evaporating Diesel Sprays and Comparison with Empirical Correlation. *Pakistan Journal of Engineering and Applied Sciences* **2010**, 7, 1–11.
- [33] Mirza, M. R. Studies of Diesel sprays interacting with cross flows and solid boundaries. Ph.D. thesis, UMIST UK, 1991.
- [34] Kaario, O.; Larimi, M.; X Tanner, F. Non-evaporating liquid spray simulations with the ETAB and WAVE droplet breakup models. **2002**,
- [35] Larimi, M.; Tiainen, J. Diesel Spray Simulation and KH-RT Wave Model. SAE Technical Paper. 2003.
- [36] Larimi, M. a. Simulation of Non-Evaporating Diesel Sprays and Verification with Experimental data. *SAE Paper 946*, 2002–01.
- [37] Postrioti, L.; Mariani, F.; Battistoni, M.; Mariani, A. Experimental and Numerical Evaluation of Diesel Spray Momentum Flux. *SAE International Journal of Engines* **2009**, 2, 287–299.
- [38] Postrioti, L.; Battistoni, M. Evaluation of Diesel Spray Momentum Flux in Transient Flow Conditions. SAE Technical Paper. 2010.
- [39] Postrioti, L.; Battistoni, M.; Ungaro, C.; Mariani, A. Analysis of Diesel Spray Momentum Flux Spatial Distribution. *SAE International Journal of Engines* **2011**, 4, 720–736.
- [40] Vita, A. D.; Allocca, L. Experimental Analysis and CFD Simulation of GDI Sprays. SAE Technical Paper. 2003.
- [41] Rotondi, R.; Bella, G. Gasoline direct injection spray simulation. *International Journal of Thermal Sciences* **2006**, 45, 168–179.

- [42] Banerjee, R.; Kumar, S. Numerical investigation of stratified air/fuel preparation in a GDI engine. *Applied Thermal Engineering* **2016**, *104*, 414–428.
- [43] Suh, E. S.; Rutland, C. J. Numerical Study of Fuel/Air Mixture Preparation in a GDI Engine. *SAE Transactions* **1999**, *108*, 2185–2201.
- [44] Cavicchi, A.; Postrioti, L.; Giovannoni, N.; Fontanesi, S.; Bonandrini, G.; Di Gioia, R. Numerical and experimental analysis of the spray momentum flux measuring on a GDI injector. *Fuel* **2017**, *206*, 614–627.
- [45] Price, C.; Hamzehloo, A.; Aleiferis, P.; Richardson, D. Aspects of Numerical Modelling of Flash-Boiling Fuel Sprays. SAE Technical Paper. 2015.
- [46] Khan, M. M.; Helie, J.; Gorokhovski, M.; Sheikh, N. A. Experimental and numerical study of flash boiling in gasoline direct injection sprays. *Applied Thermal Engineering* **2017**, *123*, 377–389.
- [47] Khan, M. M.; Sheikh, N. A. Experimental characterization of high pressure gasoline direct injection sprays. *Journal of Mechanical Science and Technology* **2017**, *31*, 2015–2022.
- [48] Kawano, D.; Ishii, H.; Suzuki, H.; Goto, Y.; Odaka, M.; Senda, J. Numerical study on flash-boiling spray of multicomponent fuel. *Heat Transfer, Asian Research* **2006**, *35*, 369–385.
- [49] Gulec, Y.; Contino, F.; Diez, A. Numerical Modeling of Flashing Sprays Using a Hybrid Breakup Model. *International Journal of Automotive Science and Technology* **2018**, *2*, 1 – 9.
- [50] Price, C.; Hamzehloo, A.; Aleiferis, P.; Richardson, D. Numerical modelling of fuel spray formation and collapse from multi-hole injectors under flash-boiling conditions. *Fuel* **2018**, *221*, 518–541.
- [51] Bianchi, G. M.; Forte, C.; Negro, S.; Pelloni, P. A 1d Model for the Prediction of Flash Atomization in Gdi Multi-Hole Injectors: Preliminary Results. *SAE*

- International Journal of Engines* **2008**, *1*, 1278–1293.
- [52] Vesilind, P. The Rosin-Rammler particle size distribution. *Resource Recovery and Conservation* **1980**, *5*, 275–277.
- [53] Alderliesten, M. Mean Particle Diameters. Part VII. The Rosin-Rammler Size Distribution: Physical and Mathematical Properties and Relationships to Moment-Ratio Defined Mean Particle Diameters. *Particle & Particle Systems Characterization* **2013**, *30*, 244–257.
- [54] Reitz, R. D.; Diwakar, R. Structure of High-Pressure Fuel Sprays. SAE Technical Paper. 1987.
- [55] 6.5.2 Secondary Breakup Models. [https://www.sharcnet.ca/Software/Ansys/16.2.3/en-us/help/cfx\\_thry/spray\\_secondary\\_breakup.html](https://www.sharcnet.ca/Software/Ansys/16.2.3/en-us/help/cfx_thry/spray_secondary_breakup.html), (Accessed Feb 28, 2019).
- [56] Stiesch, G. *Modeling engine spray and combustion processes*; Heat and mass transfer; Springer: Berlin Heidelberg, 2010; OCLC: 746236436.
- [57] Pilch, M.; Erdman, C. Use of breakup time data and velocity history data to predict the maximum size of stable fragments for acceleration-induced breakup of a liquid drop. *International journal of multiphase flow* **1987**, *13*, 741–757.
- [58] Ghadimi, P.; Yousefifard, M.; Nowruzi, H. Applying Different Strategies within OpenFOAM to Investigate the Effects of Breakup and Collision Model on the Spray and in-Cylinder Gas Mixture Attribute. *9*, 11.
- [59] O'Rourke, P. J.; Amsden, A. A. The Tab Method for Numerical Calculation of Spray Droplet Breakup. SAE Technical Paper. 1987.
- [60] Rotondi, R.; Helie, J.; Leger, C.; Mojtabi, M.; Wigley, G. Multihole gasoline direct injection spray plumes. 2010.
- [61] O'Rourke, P. J. Collective drop effects on vaporizing liquid sprays. 1981.

- [62] Droplet Collisions in Diesel Spray and Implementations of Collisions in SolidParticle. [http://www.tfd.chalmers.se/~hani/kurser/OS\\_CFD\\_2010/josefRunsten/josefRunstenReport.pdf](http://www.tfd.chalmers.se/~hani/kurser/OS_CFD_2010/josefRunsten/josefRunstenReport.pdf), (Accessed Mar 6, 2019).
- [63] Zuo, B.; Gomes, A. M.; Rutland, C. J. Modelling superheated fuel sprays and vaporization. **2000**, *1*, 16.
- [64] Ranz, W. E.; Marshall, W. R. E. f. D. Chemical Engineering Progress. **1952**, *48*, 173–180.
- [65] OpenFOAM: User Guide: k-epsilon. <https://www.openfoam.com/documentation/cpp-guide/html/guide-turbulence-ras-k-epsilon.html>, (Accessed Mar 6, 2018).
- [66] Shih, T. H.; Liou, W. W.; Shabbir, A.; Yang, Z.; Zhu, J. A new k-epsilon eddy viscosity model for high Reynolds number turbulent flows. *Computers and Fluids* **1995**, *24*, 227–238.
- [67] OpenFOAM: User Guide: Realizable k-epsilon. <https://www.openfoam.com/documentation/guides/latest/doc/guide-turbulence-ras-realizable-k-epsilon.html#sec-turbulence-ras-realizable-k-epsilon-properties>, (Accessed May 12, 2019).
- [68] Karrholm, F. P. *Numerical Modelling of Diesel Spray Injection, Turbulence Interaction and Combustion*; Doktorsavhandlingar vid Chalmers Tekniska Hogskola; Chalmers Univ. of Technology: Goteborg, 2008.
- [69] Ruiz-Rodriguez, I.; Pos, R.; Megaritis, T.; Ganippa, L. Investigation of Spray Angle Measurement Techniques. *IEEE Access* **2019**, 1–1.
- [70] Jafarmadar, S.; Heidarpour, V. Numerical studies of spray breakup in a gasoline direct injection (GDI) engine. *Thermal Science* **2011**, *15*, 1111–1122.
- [71] Heptane. <https://webbook.nist.gov/cgi/cbook.cgi?ID=142-82-5>, (Accessed May 2, 2018).
- [72] Heywood, J. B. *Internal Combustion Engine Fundamentals*; McGraw-Hill series

in mechanical engineering; McGraw-Hill: New York. 1988.